E.O. Paton Electric Welding Institute of the National Academy of Science of Ukraine
International Association “Welding”

The Paton Welding Journal

03
2025

International Scientific-Technical and Production Journal ◆ Founded in January 2000 (12 Issues Per Year)

Address of Editorial Office:
E.O. Paton Electric Welding Institute, 11 Kazymyr Malevych Str., 03150, Kyiv, Ukraine
E-mail: office@paton.kiev.ua; https://paton.org.ua/en/

Address of Publisher:
International Association “Welding”, 11 Kazymyr Malevych Str., 03150, Kyiv, Ukraine
Tel.: (38044) 205 23 90, E-mail: patonpublishinghouse@gmail.com; journal@paton.kiev.ua
https://patonpublishinghouse.com/eng/journals/tpwj

The Journal was registered by the National Council of Ukraine on Television and Radio Broadcasting on 09.05.2024, carrier identifier R30-04569
ISSN 0957-798X (Print), ISSN 3041-2293 (Online)
DOI: https://doi.org/10.37434/tpwj, from #01, 2020 to now; DOI: https: //doi.org/10.15407/tpwj from #01, 2014 to #12, 2019.

Subscriptions, 12 issues per year:
348 Euro — annual subscription for the printed (hard copy) version, air postage and packaging included;
288 Euro — annual subscription for the electronic version (sending issues in pdf format or providing access to IP addresses).

Representative Offices of “The Paton Welding Journal”:

BRAZIL, Arc Dynamics
Address: Nova Iguacu, Rio de Janeiro, Brazil
Daniel Adolpho, Tel.: +55 21 9 6419 5703,
E-mail: dadolpho@arcdynamics.com.br

CHINA, China-Ukraine Institute of Welding, Guangdong Academy of Sciences
Address: Room 210, No. 363 Changxing Road, Tianhe, Guangzhou, 510650, China
Zhang Yupeng, Tel.: +86-20-61086791,
E-mail: patonjournal@gwi.gd.cn

BULGARIA, Bulgarian Welding Society
Address: Blvd. Asen Yordanov No.10, Sofia 1592, Bulgaria
Pavel Popgeorgiev, Tel.: +359 899 96 22 20,
E-mail: office@bws-bg.org

POLAND, PATON EUROPE Sp. z o. o.
Address: ul. Kapitałowa 4, 35-213, Rzeszów, Poland
Anton Stepakhno, Tel.: +38067 509 95 67,
E-mail: Anton.Stepakhno@paton.ua

The content of the Journal includes articles received from authors from around the world in the field of welding, cutting, cladding, soldering, brazing, coating, 3D additive technologies, electrometallurgy, material science, NDT and selectively includes translations into English of articles from the following journals, published in Ukrainian:

- «Avtomatychne Zvaryuvannya» (Automatic Welding), https://patonpublishinghouse.com/eng/journals/as;
- «Suchasna Elektrometalurhiya» (Electrometallurgy Today), https://patonpublishinghouse.com/eng/journals/sem;
- «Tekhnichna Diahnostyka ta Neruinivnyi Kontrol» (Technical Diagnostics & Nondestructive Testing), https://patonpublishinghouse.com/eng/journals/tdnk.

CONTENTS

ORIGINAL ARTICLES

INFORMATION

---

*Translated Article(s) from “Avtomatychne Zvaryuvannya” (Automatic Welding), No. 1, 2025.

**Translated Article(s) from “Suchasna Elektrometalurhiya” (Electrometallurgy Today), No. 1, 2025.

***Translated Article(s) from “Tekhnichna Diahnostyka ta Neruinivnyi Kontrol” (Technical Diagnostics & Nondestructive Testing), No. 4, 2024.

Indexing: The electronic edition of the Journal is stored in the V.I. Vernadsky National Library of Ukraine (eVerLib), included in the OPEN UKRAINIAN CITATION INDEX database and international databases: CROSSREF, EBSCO, Google Scholar, INDEX COPERNICUS, ULRICHSWEB.

DOI: https://doi.org/10.37434/tpwj2025.03.01

DETERMINATION OF THE QUANTITATIVE PHASE COMPOSITION OF THE METAL OF WELDED JOINTS OF HIGH-ALLOY STEELS, INCLUDING DUPLEX STEELS

G.V. Fadeeva[1], **S.Yu. Maksymov**[1], **Chuanbao Jia**[2], **D.V. Vasiliev**[1], **A.A. Radzievska**[1]

[1]E.O. Paton Electric Welding Institute of the NASU
11 Kazymyr Malevych Str., 03150, Kyiv, Ukraine
[2]MOE Key Lab for Liquid-Solid Structure Evolution and Materials Processing, Institute of Materials Joining, Shandong University, Jinan 250061

ABSTRACT

The article considers the main techniques and methods available today for quantitative determination of the phase composition of metal in welded joints of high-alloy and duplex stainless steels (DSS). The feasibility of using particular method in different cases is analysed. The article presents the results of the analysis of the influence of cooling rate on the structure and phase composition of weld metal and HAZ during welding of high-alloy chromium-nickel steels and duplex stainless steels. It is shown that due to the influence of high cooling rates, such as during welding in aqueous medium, the amount of ferritic component in the weld metal and deposited metal of high-alloy steels decreases, whereas in the weld metal and HAZ of duplex steels, on the contrary, the amount of austenitic component decreases. This depends on the type of metal solidification. The presented data explain the differences in determining the phase composition of the weld metal and deposited metal at the same alloying during welding in different environments. The main advantages and disadvantages of various techniques and methods for quantitative determination of the phase composition of welded joints of high-alloy and duplex steels are shown.

KEYWORDS: high-alloy chromium-nickel steels, duplex steels, phase composition, austenite, ferrite, cooling rate, methods for quantitative determination of phase composition

INTRODUCTION

The main task in welding high-alloy austenitic steels and duplex stainless steels (DSS) is to ensure conditions that should help mitigating the negative impact of the thermal welding cycle (TWC) on the microstructure and phase composition of weld metal and HAZ of welded joints.

Depending on welding conditions, primarily on the cooling rate, in the temperature range of phase transformations, which is almost the same for both high-alloy austenitic steels and duplex stainless steels and corresponds to the temperature range T = 1450–800 °C for high-alloy austenitic steels and a slightly lower temperature range for duplex stainless steels T = 1300–800 °C, depending on the chemical composition of the metal, a corresponding structure is formed with a certain composition of austenite and ferrite phase components. The microstructure and its phase composition are the most important factors that determine the basic technological and other characteristics, such as mechanical properties and corrosion resistance, as well as resistance to hot crack formation as, for instance, in welding austenitic steels.

The most efficient method to increase the resistance of austenitic welds against the formation of hot cracks is to provide the weld metal with a ferritic component. Producing welds having an austenitic-ferritic structure with the amount of ferrite from 2 to 7–8 % significantly improves the resistance of the weld metal against the formation of hot solidification cracks [1]. The upper limit of ferrite content is limited to the specified amount in the case of operation of products at a temperature above 300 °C [2]. In some cases, to ensure the required corrosion resistance in highly aggressive non-oxidizing environments, the presence of ferritic phase in the weld metal or in the base metal is not allowed [3]. For operation at cryogenic temperatures, stable austenitic chromium-nickel and chromium-nickel-molybdenum steels containing 17–25 % chromium, 8–25 % nickel, and 3–6 % molybdenum are usually used. In these steels, the martensitic transformation is suppressed and the austenitic structure is preserved down to the lowest temperatures (–196 °C). These steels are stable austenitic and, therefore, the content of ferritic component in such welds and in the welded metal is also unacceptable. The welds should have a greater margin of austeniticity compared to the base metal, i.e. the Cr_{eq}/Ni_{eq} ratio should be lower than the Cr_{eq}/Ni_{eq} ratio of the base metal [4].

In duplex stainless steels, the optimum combination of high strength characteristics and corrosion resistance against pitting corrosion and stress corrosion cracking is achieved when the ratio of ferritic and austenitic phases in the metal structure is 1:1, i.e., when the content of each component is 50 %.

Table 1. Ferrite content in welded joint according to standards

Standard description	Ferrite content		
	BM	HAZ	WM
API RP 582 (API A 938 C) [6]	30–65	30–65	30–65
NORSOK M630 D45 [7]	35–55	30–70	
Specification for the oil and gas industry	35–55	< 60–65	< 60

Under the effect of the welding thermal cycle due to the high heating and cooling rates inherent in various types of welding, the original austenite-ferrite phase balance is violated. To maintain this balance, guidelines and standards provide recommendations to ensure the content of austenitic and ferritic components in different parts of a welded joint in the required amounts. The ferrite content in the weld metal and heat-affected zone should be within 25–70 % to ensure the optimum mechanical properties and corrosion resistance [5].

Different fields of operation of high-alloy steel welded joints and industries are governed by regulatory documents and standards, as well as welding process instructions that specify the phase composition of the weld metal and HAZ to ensure the required characteristics and corrosion resistance of a weldment.

Table 1 shows the requirements for ferrite content in a welded joint of duplex stainless steels used in the oil and gas industry.

Many studies have been devoted to the influence of microstructure and austenite/ferrite ratio in duplex stainless steels on the mechanical properties and corrosion resistance of welded joints [8–10].

The corrosion resistance and mechanical properties of welded joints of austenitic, austenitic-ferritic and duplex steels under different operating conditions have their own characteristics and depend on many factors, such as chemical composition, structural heterogeneity, phase composition, etc. Determination of the quantitative phase composition of structural components in the metal of welded joints is of great importance for ensuring the main technological properties of welded structures.

All of the stated above indicates the importance of determining the phase composition of weld metal and HAZ in welding high-alloy steels of austenitic, austenitic-ferritic grades, as well as duplex stainless steels of ferritic-austenitic grade.

Taking into account the relevance of the above material, it is necessary to analyse the basic techniques and methods available today for determining the phase composition of metal in welded joints of high-alloy steels and duplex stainless steels.

THE AIM

of this study is to find out the feasibility of using a particular technique and method for determining the quantitative phase composition, as well as to show, based on experimental data, the effect of cooling rate on the microstructure and phase composition of the welded joint metal during welding in different environments; to show the basic advantages or disadvantages of different techniques and methods for quantitative determination of the phase composition in welding high-alloy steels.

ANALYSIS OF AVAILABLE METHODS FOR QUANTITATIVE DETERMINATION OF THE PHASE COMPOSITION OF WELDED JOINTS

There are several basic methods for determining the phase composition of high-alloy steels of various structural classes, such as Scheffler, Delong, WRC-1992 (FN) and Espy diagram, measurements using ferritometers and feritscopes, manual point counting according to ASTM E562, X-ray diffraction analysis, and image analysis software.

Let us consider each of these methods in more details.

CONSTITUTION DIAGRAMS

To determine the structure of high-alloy welds by their chemical composition, constitution diagrams are commonly used, constructed depending on the content of elements that stabilize austenite and ferrite. To take into account the influence of alloying elements on the structure and phase composition of welds in relation to nickel and chromium, the concepts of nickel equivalent (Ni_{eq}) and chromium equivalent (Cr_{eq}) were introduced, which take into account the influence of other alloying elements in relation to nickel and chromium. The calculated values of Ni_{eq} and Cr_{eq} are used to determine the phase composition of metal on the constitution diagrams.

The type of solidification of the weld metal can also be determined by the pseudo-binary diagram (Fe–Cr–Ni), constructed using the equivalent Cr_{eq}/Ni_{eq} ratio. This ratio in the pseudo-binary diagram (Fe–Cr–Ni) provides important information about the mode of primary solidification and phase transformations during cooling.

Figure 1 shows a pseudo-binary diagram constructed using the equivalent Cr_{eq}/Ni_{eq} ratio [11].

According to the Scheffler [12], Delong [13], WRC-92 (FN) [14] and Espy diagram [15], the phase composition of the weld metal can be determined. The following equations are used to determine Ni_{eq} and Cr_{eq} for the Scheffler, Delong, WRC-92 (FN) and Espy diagram:

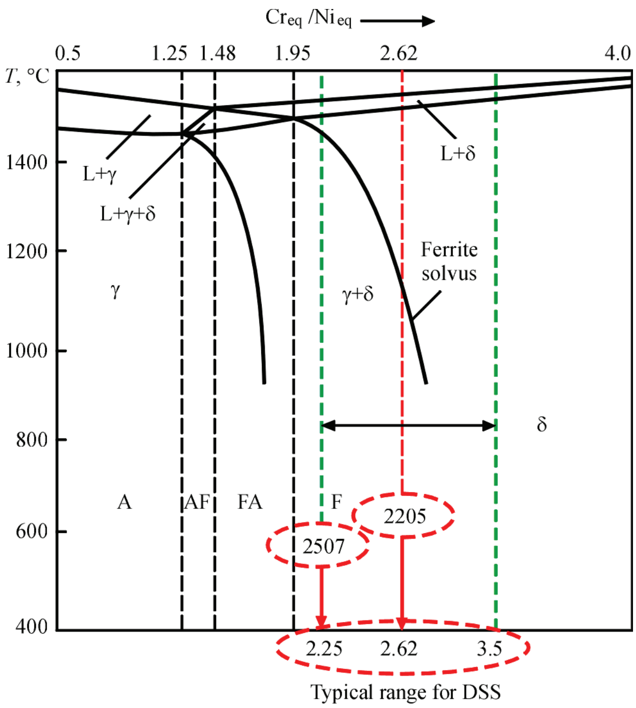

Figure 1. Pseudo-binary (Fe–Cr–Ni) diagram constructed using the equivalent Cr_{eq}/Ni_{eq} ratio [11]

Scheffler diagram (1949)

$$Cr_{eq} = Cr + Mo + 1.5Si + 0/5Nb; \quad (1)$$

$$Ni_{eq} = Ni + 30C + 0.5Mn; \quad (2)$$

Delong diagram (1973)

$$Cr_{eq} = Cr + Mo + 1.5Si + 0.5Nb; \quad (3)$$

$$Ni_{eq} = Ni + 30C + 30N + 0.5Mn; \quad (4)$$

WRC-92 diagram (FN)

$$Cr_{eq} = Cr + Mo + 0.7Nb; \quad (5)$$

$$Ni_{eq} = Ni + 35C + 20N + 0.25Cu; \quad (6)$$

Espy diagram (2005)

$$Cr_{eq} = Cr + Mo + 1.5Si + 0.5Nb + 5V + 3Al; \quad (7)$$

$$Ni_{eq} = Ni + 30C + 0.87Mn + 0.33Cu + 30(N - 0.045). \quad (8)$$

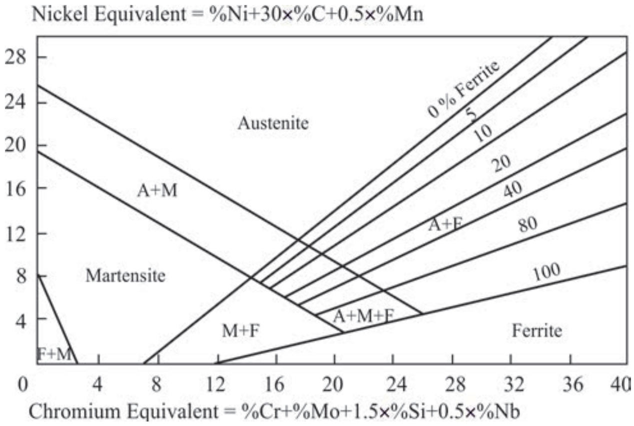

Figure 2. Scheffler constitution diagram [12]

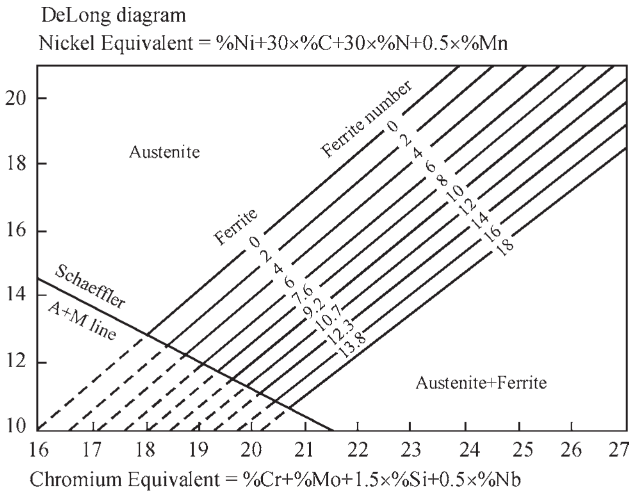

Figure 3. Delong constitution diagram [13]

In addition to equations (1–8), there are other equations for calculating Cr_{eq} and Ni_{eq}, namely (9, 10) [16–18].

$$Ni_{eq} = Ni + Co + 0.1Mn – 0.01Mn^2 + 18N + 30C; \quad (9)$$

$$Cr_{eq} = Cr + 1.5Mo + 1.5W + 0.48Si + 2.3V + 1.75Nb + 2.5Al. \quad (10)$$

Figures 2–4 show the above constitution diagrams.

The cooling rate also affects the type of metal solidification. With its increase, the austenitic region expands during the solidification of austenitic stainless steels at ultra-high cooling rates (Figure 5).

Initially, on the basis of experimental studies, a Scheffler diagram was created to predict the phase composition of weld metal of high-alloy steels of various structural grades for the cooling rate typical of the welding process [12].

With the emergence of nitrogen-containing steels, Delong took into account the presence of nitrogen in the steel and in the weld metal through its contribution to the nickel equivalent [13]. The effect of nitrogen on the austenitic phase is similar to that of carbon. Both alloying elements have the same effect

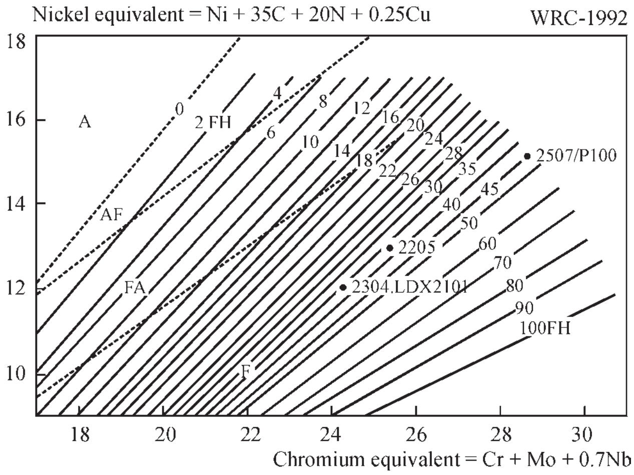

Figure 4. WRC-92 (FN) constitution diagram [14]

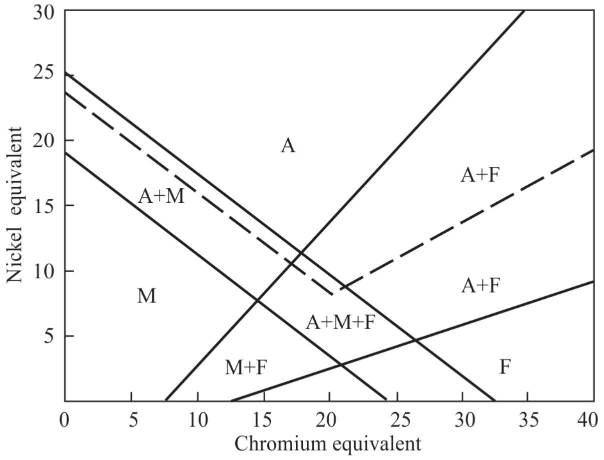

Figure 5. Modified Scheffler diagram for cooling rate of approximately 10^6 K/s [19, 20]

on increasing the stability of austenite, which is determined by the coefficient 30. This formula allows for a more accurate evaluation of the phase composition and microstructure of steels containing nitrogen in higher amounts.

Recently, the Espy diagram has been introduced. This diagram is a modification of the Scheffler diagram and, similar to the Delong diagram, takes into account the influence of nitrogen and other alloying elements. In this case, Cr_{eq} and Ni_{eq} are calculated according to equations (7) and (8) [15].

Analyzing the equations that are used to determine Cr_{eq} and Ni_{eq}, it can be found that for today, there is no unanimous opinion on the equivalent impact of different austenite- and ferrite-forming elements. Some publications provide different coefficients. Thus, the coefficient of ferrite-forming action of molybdenum is in the range from 1 to 2 [1]. There are also different coefficients of impact of the austenite-forming effect of nitrogen, which range from 18 to 30. This indicates that up to this day, the degree of impact of various elements on the structure and phase composition of weld metal is being improved and clarified. This explains that prediction of the phase composition of weld metal using constitution diagrams and determination of Cr_{eq} and Ni_{eq} cannot provide high accuracy when using this method.

The most accurate version for predicting weld metal in welding duplex steels (DSS), recommended by the Welding Research Council (WRC), is the WRC-1992 (FN) diagram [14]. Its use can predict the structure with an accuracy of approximately ±4 ferrite number (FN) when calculating its levels up to 18 FN. The diagram can be used for values of up to 100 FN, which is important for duplex stainless steels.

On the Delong and WRC-92 (FN) constitution diagrams, the amount of ferritic component can be defined as a percentage of ferrite content or as a ferrite number FN. The ferrite number was originally supposed to be a reasonable approximation of the “ferrite percentage” in the metal of a 19-9 or 308 type weld, but later studies show that FN is significantly higher than the “ferrite percentage” in the weld metal. The adoption of an arbitrary “ferrite number” scale is related to the use of measuring instruments and their calibration, which are widely used in foreign measuring instruments — feritscopes. This issue will be discussed in more detail in the next section.

Methods for determining the microstructure and phase composition of weld metal of high-alloy steels of various structural classes using Scheffler, Delong, WRC-92 (FN) and Espy constitution diagrams, as well as according to the pseudo-binary diagram (Fe–Cr–Ni) by calculating Cr_{eq} and Ni_{eq} and their ratio can be successfully used by researchers and developers of welding consumables for prediction when choosing a weld metal alloying system, as well as to determine a welding technology. For a more accurate determination of the phase composition, it is necessary to additionally use other methods.

MEASUREMENTS USING FERRITOMETERS AND FERITSCOPES

Measurement using ferritometers and feritscopes belongs to non-destructive types of testing and quantitative determination of the phase composition of welded joints. The operation of these devices is based on the concept that the ferrite phase (α-phase) and strain martensite (α′-phase) are ferromagnetic, while the austenite phase is paramagnetic.

When using the volumetric method, standard size specimens that are cut out of the test area are magnetized to the state of technical saturation. This is a destructive method. At local magnetic testing, the material is magnetized only at a small area of a product. Most existing modifications of ferritometers that are still in use are based on the local principle of measuring the ferritic component. The local method of magnetic ferritometry is widely used in the non-destructive method of determining the quantitative phase composition due to its efficiency and the ability to determine the content of the ferritic phase directly in a finished product.

The operation of feritscopes used abroad is based on measuring the breakaway force of a permanent magnet from the surface of a specimen. This measurement uses the term “ferrite number” or FN.

The disadvantage of quantitative phase composition measurements using ferritometers and feritscopes is that the measurement is only possible in the weld metal or base metal. It is impossible to measure the phase composition in the HAZ of a welded joint using these methods due to its small size.

Today, a modern portable Feritscope FMP 30 is available designed for measuring the ferrite content of high-alloy steels of the austenitic-ferritic grade, as well as duplex steels, in which the measurement of the magnetic component can be both in percentage as well as on a scale (FN) [21].

Advantages:

- two measuring ranges;
- switching option for measuring ferrite on the FN scale and as a percentage of ferrite;
- measuring range from 0.15 to 80 % of ferrite, or from 0.15 to 110 FN;
- measurements according to ISO 17655 or Basler Standard;
- calibration specimens are produced based on the international TWI secondary standards that meet the requirements of ISO 8249 and AWS A 4. 2M;
- compliance with the measurement accuracy specified in ANSI/AWS A4. 2M/A 4.2 1997.

MANUAL POINT COUNTING METHOD ACCORDING TO ASTM E 562

This test method describes a systematic manual point counting procedure for statistical evaluation of the volume fraction of an identified phase on metallographic images using a point grid [22]. Although the method of manual point counting is standardized and widely used to determine the quantitative phase composition, it should be recognised that its main disadvantage is the slowness and high labour intensity, operator subjectivity, which depends on his skills, the dependence of the relative measurement accuracy on a number of fields and points, which can lead to imperfect results. Determination of the measured phase by different operators on the same metallographic image can lead to completely different values of the volume fraction of the phase component. This method is very imperfect and its application requires verification and comparison with other methods.

X-RAY DIFFRACTION METHOD OF ANALYSIS

Determination of the phase composition of high-alloy and duplex stainless steels by X-ray diffraction (XRD) analysis is the most contemporary and advanced method.

Advantages of X-ray diffraction (XRD) analysis:

- high accuracy in determining crystal phases;
- phase composition is determined in volume;
- can determine the quantitative ratio of phases in a specimen;
- reveals the exact crystal structure and defects in the crystal lattice;
- ability to analyse small specimens.

Disadvantages:

- XRD requires more expensive specialized and more complex equipment and specimen preparation.

METHOD USING IMAGE ANALYSIS SOFTWARE

There are several powerful types of software for analysing steel microstructures. The most popular and effective of them are:

1. ImageI/Fiji is a free, open source image analysis software. It is widely used in materials science for microstructure analysis, including grain size measurement, phase analysis, and statistical processing.
2. MIPAR™ is a software package specifically designed for the analysis of material microstructures. It offers advanced features for image segmentation, quantitative phase analysis and microstructure characterisation.
3. Clemex Vision PE is a comprehensive solution for image analysis in materials science. It offers automated tools for analysing grains, particle shape, phase distribution and other microstructure parameters.
4. OLYMPUS Stream, Carl Zeiss Axio Vision, Thermo Scientific™ Phenom Particle X are image analysis software specially developed by microscope manufacturers and used with the respective OLYMPUS, Carl Zeiss, Phenom microscopes for automated analysis of various microstructure parameters.

The following advantages of image analysis software can be noted:

- easier in use and cheaper equipment compared to XRD;
- possibility of visualization and evaluation of microstructure;
- helps in studying morphology and phase distribution.

The disadvantages include:

- accuracy depends on the quality of images obtained (e.g. SEM or optical microscopy);
- less accurate quantitative analysis compared to XRD;
- may be less accurate compared to XRD, especially when detecting small phases or microstructural components;
- probable subjective interpretation of results.

Each of these software has its own advantages and the choice depends on the specific needs of the study, steel grade and microstructure to be analysed, and the availability of the particular software. Comparing these two analysis methods, XRD and software, it can be determined that XRD is suitable for material

Table 2. Impact of nitrogen on the structure of chromium-nickel steels [23]

No.	Chemical composition, wt.%			Standard solubility of nitrogen $S_{N, 1873}$, %	Structural composition	
	Cr	Ni	N		Metallographic evaluation	According to Scheffler without nitrogen
1	21.0	6.0	0.47	0.31	A + 21 % F	A + 13 % F
2	21.0	6.0	0.56		A + traces F	A + 8 % F
3	21.0	6.0	0.61		A	–
4	23.5	6.5	0.42	0.32	A + 10 % F	A + 18 % F
5	23.5	6.5	0.45		A + traces F	A + 17 % F
6	23.5	6.5	0.51		A	A + 14 % F
Notes: A — austenite; F — ferrite.						

Table 3. Chemical composition of steels, wt.%

No	Chemical composition of steels					
	C	Mn	Si	Ni	Cr	N
1	0.08	1.2	0.8	6.0	21.0	0.47
2	0.08	1.2	0.8	6.0	21.0	0.56
3	0.08	1.2	0.8	6.0	21.0	0.61
4	0.08	1.2	0.8	6.5	23.5	0.42
5	0.08	1.2	0.8	6.5	23.5	0.45
6	0.08	1.2	0.8	6.5	23.5	0.51

volume analysis and crystal structure determination, whereas software is useful for surface analysis and phase morphology.

Both methods complement each other and can be used together for a complete analysis of the phase composition and microstructure of high-alloy and duplex stainless steels.

To determine the feasibility of using particular method for determining the quantitative phase composition of the metal of welded joints of high-alloy steels and to compare them with each other, examples from the literature are given.

In [23], the structural phase composition of steels containing nitrogen was evaluated by two methods: metallographic and using Scheffler diagram. In this case, the use of the Scheffler diagram is not quite accurate, since it does not take into account the impact of nitrogen. The kind of metallographic method was not specified. Table 2 shows data on the impact of nitrogen on the phase composition of steel.

Using the data from [23], we made an attempt to find out which of the constitution diagrams, Delong, WRC-92 (FN) or Espy, can most accurately predict the phase composition of nitrogen-containing steels. To calculate Cr_{eq} and Ni_{eq}, it was assumed that the metal contains C = 0.08 wt.%, Si = 0.8 wt.% and Mn = 1.2 wt.%. Table 3 shows the chemical composition of the steels selected for calculation of Cr_{eq} and Ni_{eq} to determine the phase composition.

To determine the phase composition according to the Delong constitution diagram, Cr_{eq} and Ni_{eq} were calculated according to equations (3) and (4), for the WRC-92 (FN) diagram — according to equations (5) and (6), and for the Espy diagram — according to equations (7) and (8). The phase composition of steels is shown in Table 4.

Table 4. Phase composition of steels

No	Composition of steels									
	Metallographic evaluation [24]	Delong			WRC-92 (FN)			Espy		
		Cr_{eq}	Ni_{eq}	Phase composition F, %	Cr_{eq}	Ni_{eq}	Phase composition F, %	Cr_{eq}	Ni_{eq}	Phase composition F, %
1	A+21 % F	22.2	23.1	A	21.0	18.2	A	21.0	22.15	A
2	A + traces F	22.2	25.8	A	21.0	20.0	A	21.0	24.85	A
3	A	22.2	27.3	A	21.0	21.0	A	21.0	26.35	A
4	A+10 % F	25.0	22.1	A + 2 % F	25.0	17.3	A + 10 % FN	25.0	21.15	A
5	A + traces F	25.0	23.0	A	25.0	17.9	A + 8 % FN	25.0	22.05	A
6	A	25.0	24.8	A	25.0	19.1	A + 6 % FN	25.0	23.79	A

Analysing the data presented in Tables 3 and 4, it can be found that the prediction of the phase composition of steels according to the Delong and Espy diagrams shows almost the same result. These diagrams are modified from the Scheffler diagram, however they consider the impact of nitrogen on the expansion of the austenitic region. The phase composition of steels calculated according to the WRC-92 (FN) diagram differs slightly from the composition based on the metallographic evaluation. The largest difference in the phase composition of steels compared to the metallographic evaluation corresponds to the Scheffler diagram, if the impact of nitrogen on the phase composition is not taken into account. The differences in the determination of the phase composition in the metal by the metallographic evaluation and constitution diagrams are associated with the fact that [23] considers steels with nitrogen content in the greater amount than its solubility in the metal. Only the nitrogen and carbon content being in the solid solution should be taken into account in the constitution diagrams. It should be noted that all constitution diagrams are designed to predict the weld metal of welded joints, i.e. according to the cooling rates inherent in welding. For example, the Scheffler diagram was created on the basis of experimental data during coated electrode welding, i.e. according to manual arc welding technology. Other diagrams were also developed on the basis of experimental data obtained during outdoor welding. In other words, all constitution diagrams were created for weld metal. It can be said that it is not entirely reasonable to expect the results of predicting the phase composition of steels according to constitution diagrams to be identical to the metallographic evaluation.

In [24], the prediction of ferrite content in the weld at welding dissimilar joints of duplex steel DSS 2205 and stainless steel ASS 316 L was studied using Espy and WRC-92 (FN) constitution diagrams. The ferrite content was also measured experimentally using a Fischer FMP30 feritscope. It has been proven that the use of the WRC-92 constitution diagram (FN) to predict the ferrite content in the weld metal in the amount of FN can lead to a deviation of FN of approximately ±8.69 at welding with an input energy of 0.60 kJ/mm and ±3.86 FN with an input energy of 45 kJ/mm. Whereas, the Espy diagram has a deviation of ±2 % from the experimentally measured value using a feritscope. Prediction by the Espy diagram is less dependent on the cooling rate and is more accurate.

This example shows that the use of constitution diagrams to predict the phase composition of weld metal in welding dissimilar steels can be quite successful.

The Scheffler constitution diagram is also used to predict the phase composition of the weld metal in welding dissimilar steels —low-alloyed with austenitic steels [25].

The prediction of weld metal microstructure carried out based on constitution diagrams and calculation of Cr_{eq} and Ni_{eq} does not take into account the effect of cooling rate and, therefore, has rather limited practical application, especially in welding technologies where the cooling rate differs from the usual one, for example, during welding in aqueous medium, electron beam welding or welding in a pulsed mode, etc. Therefore, to check the predicted phase composition of the weld metal, it is appropriate to compare it with the experimental evaluation of the phase composition using ferritometers or feritscopes.

In [10], the ferrite content in the HAZ of duplex stainless steel 2205 was studied using the manual point counting method in accordance with ASTM E 562 standard [22]. It was noted that the measurement of ferrite in the base metal and in the weld metal using ASTM E 1245 standard [26] usually gives equivalent results compared to the manual point counting method. Determination of the maximum ferrite content in HAZ by this method is complicated. ASTM E 562 is a reference for measuring phases (austenite and ferrite), but does not specify the exact magnification for metallographic examination. Depending on the magnification level, the ferrite content in HAZ shows different results: at a magnification of ×400, the ferrite content is 48 %, at a magnification of ×1000, the ferrite content is determined to be 76 %, i.e., it differs by 1.5 times. Therefore, a magnification of ×400 is not fully representative, whereas a magnification of ×1000 is more suitable for evaluation of the ferrite content in HAZ. In other words, the interpretation of the ferrite content is highly dependent on the operator's skills. The manual point counting method using the grid methodology determines the ferrite content from 50 to 75–80 % for one and the same microstructure.

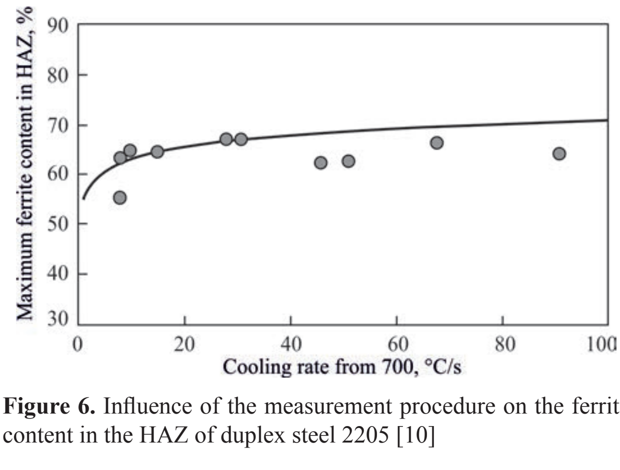

Figure 6. Influence of the measurement procedure on the ferrite content in the HAZ of duplex steel 2205 [10]

Table 5. Ferrite content in weld metal [27]

No	Welding methods	Feritscope (EFN)	Metallographic evaluation, %
1	Electric arc welding with W-electrode	104	78
2	Electric arc welding with W-electrode with additional Ni filler	74	58
3	Electron beam welding	114	86
4	Electron beam welding with additional Ni filler	80	61

Table 6. Phase composition of HAZ modelled at different cooling rates in the temperature range $T = 1300–800$ °C

HAZ cooling rate, °C/s	Phase fraction, %		
	δ-ferrite	γ-austenite	Excess phase (fine)
Base metal	52.000	48.000	–
8.21	57.499	38.674	3.236
81.70	64.644	30.268	3.746
165.85	67.696	20.965	8.606
320.51	68.848	17.733	13.437

Table 7. Quantitative phase composition and crystal lattice parameters of phase components in the welded joint

Examination area	Method for determining the phase composition	Phase component, %			
		δ-Fe		γ-Fe	
		Content	Lattice period, nm	Content	Lattice period, nm
Weld metal	X-ray diffraction phase analysis	19.4	0.2889	80.6	0.3607
	MIPAR	19.0	–	81.0	–
Base metal	X-ray diffraction phase analysis	52.8	0.2886	47.2	0.3614
	MIPAR	52.0	–	48.0	–

Figure 6 shows the effect of the measurement procedure on the ferrite content in the HAZ of duplex steel 2205. The measurements were carried out according to ASTM E 562.

I.e., this method is very imperfect according to ASTM E 562.

In [8], different welding technologies are compared: electron beam welding, which is characterized by high cooling rates, and electric arc welding with a W-electrode in shielding gas. The ferrite content in the weld metal was measured using a Fisher Feritscope (based on the expanded ferrite number EFN) and the metallographic method of manual point counting. Table 5 shows the measurement results.

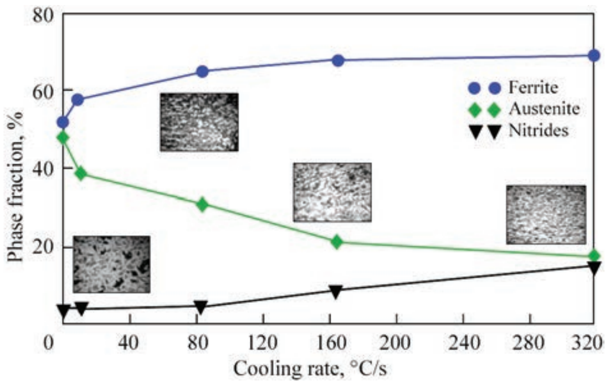

Figure 7. Phase composition of HAZ in the duplex steel depending on the cooling rate in the temperature range of 1200 (1300)–800 °C

It has been proven that the ferrite content in electron beam welding is higher than in electric arc welding with a W-electrode, both with and without an additional nickel filler. This is explained by faster cooling rate in electron beam welding.

The type of primary solidification can be determined by the Cr_{eq}/Ni_{eq} ratio and in accordance with the pseudo-binary Fe–Cr–Ni diagram (Figure 1) [11].

Taking into account the cooling rate ranges used in welding, if $Cr_{eq}/Ni_{eq} \leq 1.5$, the solidification can be austenitic (A) or austenitic-ferritic (A/F). If the ratio is $1.5 \leq Cr_{eq}/Ni_{eq} \leq 2.0$, the solidification will be ferritic-austenitic (F/A). And finally, if $Cr_{eq}/ Ni_{eq} \geq 2.0$, the solidification will be ferritic (F) [27].

EFFECT OF COOLING RATE ON PHASE COMPOSITION DURING WET UNDERWATER WELDING OF DUPLEX STEELS (DSS) 2205 (EXPERIMENTAL DATA)

The results of preliminary studies were borrowed from [28]. Table 6 shows numerical values of the phase composition of HAZ, and Figure 7 shows a graphical representation of the phase composition of HAZ depending on the cooling rate.

Figure 7 shows the changes in the volume fractions of the phase components of ferrite, austenite, and excess phase (probably the precipitation of chromium Cr_2N nitrides) depending on the cooling rate in the modelled HAZ of the duplex steel in the temperature range T = 1300–800 °C, determined using the MIPAR image analysis software.

A study of the quantitative determination of the phase composition of the welded joint was carried out by two methods: X-ray diffraction analysis and using MIPAR software. The determination of the phase composition was carried out using a Rigaku Ultima IV X-ray diffractometer. Table 7 shows the quantitative phase composition and crystal lattice parameters of the phase components in the weld metal.

The difference in the values of determining the quantitative phase composition can be explained by the fact that the X-ray diffraction analysis method determines the phase composition in volume percents and MIPAR — in wt.%.

CONCLUSIONS

1. The basic methods for determining the quantitative phase composition of the metal of welded joints of high-alloy steels are considered and analysed, and the advantages and disadvantages of a particular method are given.

2. The choice of research method depends on the task according to which it is necessary to determine the phase composition.

3. Prediction of the phase composition of weld metal using constitution diagrams is appropriate for those welding technologies that are characterized by slow cooling of weldments in air.

4. Constitution diagrams do not take into account the cooling rate during welding and, in the cases of high performance welding methods or conditions different from free cooling of weldments in air, introduce a significant error in the determined phase composition.

5. The phase composition of the HAZ in the welded joint can be determined by XRD or by using software.

6. The most imperfect and at the same time very subjective method is manual point counting according to ASTM E562.

REFERENCES

1. Kakhovsky, N.I. (1975) *Welding of high-alloy steels.* Kyiv, Tekhnika [in Russian].
2. Kopersak, N.I. (1963) Influence of alloying elements on 475° brittleness of austenitic-ferritic deposited metal. *Avtomaticheskaya Svarka*, **7**, 15–20 [in Russian].
3. Belinsky, A.L. et al. (1970) *About corrosion resistance of pure austenitic steel grade OKh17N16M3T.* In Coll.: Protection of Metals, Vol. 6, Issue 1. Moscow, Nauka [in Russian].
4. https://uas.su/books/newmaterial/722/razdel722.php
5. Labanowski, J. (1997) Duplex steels — New material for chemical processing industry. *Eng. and Chemical Equipment*, **2**, 3–10.
6. API 582–09: *Welding quidelines for the chemical, oil, and gas industries*.
7. Norsok M-630, Edition 6. October 2013. *Material data sheets and element data sheets for piping*.
8. Muthupandi, V., Srinivasan, P.B., Seshadri, S.K., Sundaresan, S. (2003) Effect of weld metal chemistry and heat input on the structure and properties of duplex stainless steel welds. *Mater. Sci. and Eng.*: A, 358(**1–2**), 9–16. DOI: https://doi.org/10.1016/S0921-5093(03)00077-7
9. Liou, H.-Y., Hsieh, R.-I., Tsai, W.-T. (2002) Microstructure and pitting corrosion in simulated heat-affected zones of duplex stainless steels. *Materials Chemistry and Physics*, **74**, 33–42. DOI: https://doi.org/10.1016/S0254-0584(01)00409-6
10. Higelin, A., Manchet, S.L., Passot, G. et al. (2022) Heat-affected zone ferrite content control of a duplex stainless steel grade to enhance weldability. *Welding in the World*, **66**, 1503–1519. DOI: https://doi.org/10.1007/s40194-022-01326-0
11. Verma, I., Taiwade, R.V (2017) Effect of welding processes and conditions on the microstructure, mechanical properties and corrosion resistance of duplex stainless steel weldments — A review. *J. of Manufacturing Processes*, **25**, 134–152. DOI: https://doi.org/10.1016/J.JMAPRO.2016.11.003
12. Schäffler, A.L. (1949) Constitution diagram for stainless steel weld metal. *Metal Progress*, **56**, 680–680.
13. Delong, F.A. (1973) Ferrite determination in stainless steel weld metal. *Welding J.*, 52(**5**), 210-s–214-s.
14. Kotecki, D.I., Siewert, P.A. (1992) WRC-1992 constitution diagram for stainless steel weld metals: A modification of the WRC-1988 diagram. *Welding J.*, 71(**5**), 171–178.
15. Lippold, J.C., Kotecki, D.J. (2005) *Welding Metallurgy and Weldability of Stainless Steel.* Wiley, Hoboken, New Jersey.
16. Kolpingon, E.Yu., Ivanova, M.V., Shitov, E.V. (2007) Nitrogen-containing steels of equivalent composition. *Chyornye Metally,* February, 10–12 [in Russian].
17. Pomarin, Yu.M., Bialik, O.M., Hryhorenko, H.M. (2007) *The influence of gases on the structure and properties of metals and alloys.* Kyiv, NTUU KPI [in Ukrainian].
18. Cobelli, P. (2003) *Development of ultrahigh strength austenitic stainless steels alloyed with nitrogen*: Syn. of Thesis for Dr. of *Techn. Sci. Degree.* Swiss Federal Institute of Technology in Zurich.
19. Vicente, A., Silva, P.A.D., Souza, R.L.D. et al. (2020) *The use of duplex stainless steel filler metals to avoid hot cracking in GTAW welding of austenitic stainless steel AISI 316L.* DOI: https://doi.org/10.11606/T.3.2017.tde-05092017-103140
20. Jonson, E., Grabaek, L. et al. (1988) Microstructure of rapidly solidified stainless steel. *Mater. Sci. and Eng.*, **98**, 301–303. DOI: https://doi.org/10.1016/0025-5416(88)90174-7
21. http://www Sales@otec.com.ua
22. (2020) ASTM E 562: *Standard test method for determining volume fraction by systematic manual point count*. West Conshohocken, ASTM.
23. Sheiko, I.V., Grigorenko, G.M., Shapovalov, V.A. (2016) Alloying of steels and alloys with nitrogen from the arc plasma. Theory and practice (Review. Pt.1). *Sovremennaya Elektrometallurgiya*, 122(**1**), 32–37 [in Russian]. DOI: https://doi.org/10.15407/sem2016.01.05
24. Verma, J., Taiwade, R.V., Khatirkar, R.K. et al. (2016) Microstructure, mechanical and intergranular corrosion behavior

of dissimilar DSS 2205 and ASS 316 L shielded metal arc welds. *Transact. Indian Inst. Met.*, **70**, 225–237. DOI: https://doi.org/10.1007/s 2666-016-0878-8

25. Zemzin, V.N. (1966) *Welded joints of dissimilar steels*. Moscow, Mashinostroenie [in Russian].
26. (2023) ASTM E 1245-03: *Standard practice for determining the inclusion or second-phase constituent content of metals by automatic image analysis*. https://cdn.standards.iteh.ai.
27. Vicente, A., Silva, P.A.D, Sadanandan, S. et al. (2020) Study on the effect of nitrogen content and cooling rate on the ferrite number of austenitic stainless steels. *Int. J. of Advanced Eng. Research and Sci.,* 7(**11**), 270–277. DOI: https://doi.org/10.22161/ijaers.711.34
28. Maksymov, S.Yu., Fadeyeva, G.V., Jia Chuanbao, et al. (2024) Influence of cooling rate on the microstructure and phase composition of the HAZ of duplex stainless steel (DSS) 2205 during wet underwater welding. *The Paton Welding J.*, **1**, 3–12. DOI: https://doi.org/10.37434/tpwj2024.01.01

ORCID

G.V. Fadeeva: 0009-0003-8142-0110,
S.Yu. Maksymov: 0000-0002-5788-0753,
Jia Chuanbao: 0000-0002-6028-6528,
D.V. Vasiliev: 0000-0002-4629-162X,
A.A. Radzievska: 0009-0002-7718-9668

CONFLICT OF INTEREST

The Authors declare no conflict of interest

CORRESPONDING AUTHOR

S.Yu. Maksymov
E.O. Paton Electric Welding Institute of the NASU
11 Kazymyr Malevych Str., 03150, Kyiv, Ukraine.
E-mail: maksimov@paton.kiev.ua

SUGGESTED CITATION

G.V. Fadeeva, S.Yu. Maksymov, Chuanbao Jia, D.V. Vasiliev, A.A. Radzievska (2025) Determination of the quantitative phase composition of the metal of welded joints of high-alloy steels, including duplex steels. *The Paton Welding J.*, **3**, 3–12.
DOI: https://doi.org/10.37434/tpwj2025.03.01

JOURNAL HOME PAGE

https://patonpublishinghouse.com/eng/journals/tpwj

Received: 25.09.2025
Received in revised form: 29.10.2025
Accepted: 22.04.2025

DOI: https://doi.org/10.37434/tpwj2025.03.02

EMPLOYING ARTIFICIAL NEURAL NETWORKS TO ESTIMATE WELD BEAD GEOMETRY IN A-TIG WELDS

Samarendra Acharya[1], **Soumyadip Patra**[2], **Santanu Das**[3]

[1]Department of Mechanical Engineering, Global Institute of Management and Technology,
Krishnanagar-741101, West Bengal, India
[1,2,3]Department of Mechanical Engineering, Kalyani Government Engineering College, Kalyani,
741235, West Bengal, India

ABSTRACT

The present research explores the effect of ternary oxide flux on Activated-flux Tungsten Inert Gas welding of austenitic stainless steel 304. Butt joint welding was performed using three different fluxes (SiO_2, TiO_2 and Cr_2O_3) combined in various ratios. Tungsten Inert Gas welding was used to weld 8 mm thick plate of grade 304 stainless steel. Welding parameters such as penetration depth, weld bead width and reinforcement were observed. The experimental results showed that using fluxes SiO_2, TiO_2 and Cr_2O_3 resulted in improved weld penetration. Based on the current findings, centripetal Marangoni convection and constricted arc are proposed as mechanisms for enhancing the penetration of activated flux TIG welding. The microstructure of the weldment was investigated using an optical microscope and a Scanning Electron Microscope. The hardness of the weld bead was determined using the Rockwell Hardness Tester. Maximum value of the hardness was found as 66 *HRC*. The purpose of this work is to investigate the effect of oxide fluxes on weld morphology and welding parameter. Estimation of output parameters using Artificial Neural Network tool in MATLAB17 was done. The dataset was extracted from the experimental work. Heat input, flux ratio and gas flow rate have been investigated as input factors for predicting weld bead width and depth of penetration. In this research, it was found that using ten nodes in a single hidden layer produced the best outcomes. The estimated values of weld bead width and depth of penetration were found to be pretty similar to the experimental observations.

KEYWORDS: welding, activated-flux, A-TIG welding, weld bead geometry, microstructure, hardness, ANOVA (analysis of variance), artificial neural network

INTRODUCTION

Stainless steel, aluminiuum, titanium and magnesium alloys are fabricated primarily with high weld quality and a smooth, scatter-free surface obtained through the use of the tungsten inert gas (TIG) welding. Hot weldment is shielded from ambient contamination by inert shielding gas, which is primarily pure argon but is occasionally combined with hydrogen or helium. Weld spatter can be reduced using TIG welding, and excellent weld beads are typically produced. Besides these advantages, its flexibility in combining numerous types of metals opened the door for their extensive use in the industrial and civil sectors. In addition to the benefits that the TIG welding method has introduced, shallow penetration has been viewed as a disadvantage, particularly when combining thick parts [1–4]. Many techniques were developed to address the issue of poor (low) penetration; one of the most significant of these is activated flux TIG welding method, which involves covering faying surface with a paste-like mixture of an activating flux. This flux layer may be of oxide, fluoride, chloride, etc. Flux coating gets melted and evaporated with the start of welding. Penetration depth increases and welding width bead decreases as a result of arc constriction and reversal of Marangoni convection [5–7].

Babbar et al. [8] investigated on AISI 316 stainless steel under sea water environment as it is much resistant to corrosion compared to other grades of steel without molybdenum. They carried out autogenous bead-on-plate welding utilizing SiO_2 and TiO_2 in three ratios and compared it without using a flux. A maximum depth of penetration (DOP) of 5 mm was achieved.

A-TIG process can be used to weld dissimilar metals because it stabilizes DOP based on the reversal of Marangoni convection, in addition to being used to fabricate various materials such as titanium, aluminum, manganese and stainless steel. Filler metal is needed to fill the gap between the welding portions in TIG welding process with flat thickness greater than 3 mm. For 8 mm thick work piece, A-TIG welding with filler metal could be done without even edge preparation [9–10]. Venkatesan et al. demonstrated [11] how A-TIG welding could enhance penetration while welding AISI 409 ferritic stainless steel. SiO_2 flux had the highest penetration and aspect ratio (ASR) across all current levels, while TiO_2 flux had a rapid fall in ASR at higher current. A cost-effective SiO_2 and TiO_2 flux combination had up to 5 mm penetration. On the other hand, Ganesh et al. [12] explored possibility of A-TIG welding of 10 mm thick SS316LN. An unspecified multi-component oxide flux was used to accomplish autogenous welding to have 10 mm DOP in one pass; however, in TIG welding, 13 passes were needed.

Numerous research works were conducted where various facets of the A-TIG process had been considered. Pamnani et al. [13] optimised the TIG process by employing response surface approach to get the maximum welding penetration. A-TIG and TIG process performance was examined by Kumar et al. [14]. The only procedure where full DOP has been attained is A-TIG. Therefore, by concurrently boosting DOP and lowering weld bead width (WBW), the A-TIG process may enhance the performance of the TIG process. Zuber et al. [15] studied how oxide flux affects welding distortion, ferrite number, hardness value, and DOP in austenitic stainless steel 304L plates with a thickness of 8 mm. SiO_2 powder was combined with acetone and applied to a bead plate without joint preparation or the use of filler wire.

Kulkarni et al. [16] examined the microstructure and mechanical characteristics of AISI 316L and SS-Alloy 800 after connecting them. A multi-component flux was used, including 25 % MoO_3, 25 % TiO_2, 25 % V_2O_5, 15 % SiO_2 and 10 % Co_3O_4. No filler material was used in the A-TIG welding process. The AISI 316L and SS-Alloy 800 joint successfully penetrated 8 mm thick plates with no fractures or defects. The weldment zone had high impact toughness and an austenitic microstructure. Alloy 800 HAZ exhibited grain coarsening. Touileb et al. [17] evaluated the effects of activating fluxes on the 430 Ferritic Stainless Steel alloy in A-TIG welding. Three fluxes were identified: MoO_3, TiO_2 and SiO_2. Minitab 17 software was used to perform experimental runs as per design of experiment (DOE). Each run had a varied percentage of all three fluxes. The maximum DOP of 7.24 mm was attained with a combination of 55 % TiO_2 and 45 % MoO_3. It costs more than twice as much as traditional TIG welding. When A-TIG welding was employed, mechanical parameters such as tensile strength, hardness, and breaking absorbed energy were almost unchanged. Using A-TIG welding, flux resulted in a positive corrosion potential for the weld metal.

Table 1. The present experimental details

TIG welding machine	K2 by Kemppi TIG 200AC DC
	Current range 10–200 A
	Duty cycle — 25 %/200 AC
Travelling vehicle	Make — Mehta Sanghvi and Co. India
	Speed — 0.85-to 5mm/s
Belt grinder/polisher	Make — Usha Instruments, India
	Motor — power 1/4 HP

Some others [18–27] used a variety of fluxes, including ones based on chloride, oxide and fluoride, in dissimilar joining (low alloy and stainless steel). The results of this research indicate that oxide-based fluxes have produced the greatest penetration depth. Additionally, DOP was little affected by other fluxes. A-TIG welding had been the subject of several investigations, according to the literature review on the technique.

According to the literature review and preliminary experimental tests conducted using the DOE (screening) approach, the following process input variables have been considered and their corresponding intervals and levels determined: current (I), welding speed (v), and percentage of activating fluxes combination ratio (FR). It has been discovered that the most appropriate design matrix Box–Behnken Design is the best method for conducting experiments and obtaining the necessary data for modelling and optimisation purposes based on the number of process parameters and their preset values.

Then, a neural network using a back-propagation algorithm was employed to find the relationships between the process input and output parameters (I, v and FR, as well as DOP, WBW and ASR). Next, using the particle swarm optimization (PSO) method, the optimal BPNN architecture has been identified. PSO algorithm has finally been used for multi-response optimisation [28–33].

In this research work, the combination of the three activating fluxes (TiO_2, SiO_2 and Cr_2O_3) in different ratios have been taken into consideration as the process input variable It has been optimised so that DOP increases, WBW decreases. This is because different activating fluxes have different effects on the weld bead geometry, mechanical, and metallurgical properties of weldments.

MATERIALS AND METHOD

The present research employs an analytical approach to improve weld bead shape after completing tests. The Box–Behnken response surface design approach is used to conduct an A-TIG welding experiment on an austenitic stainless steel 304 work piece. To estimate what has been found, an artificial neural network (ANN) model is developed. The specifics of the proposed approach, as well as the theoretical requirements, are described in the following subsections. The experimental work was carried out using a TIG welding machine, whose specifications and other parameters are listed in Table 1. Table 2 displays the chemical composition of base metal 304 stainless steel (percentage by weight).

Table 2. The percentage of chemical composition in 304 stainless steel (wt.%)

C	Si	Mn	S	P	Cr	Ni	Fe
0.034	0.445	1.529	0.003	0.030	18.124	8.478	Rest

Table 3. Process parameters and their levels

Parameters	Symbol	Unit	Factor level		
			Max	Intermediate	Min
Heat input	HI	kJ/mm	0.734	0.634	0.534
Flux ratio	FR (SiO_2:TiO_2:Cr_2O_3)	–	72:18:10	65:25:10	45:45:10
Gas flow rate	GFR	l/min	16	14	12

Table 4. Trial experiment

No	HI, kJ/mm	*v*, mm/s	Root gap, mm	Flux	GFR, l/min	WBW, mm	Reinforcement, mm	DOP, mm
1	0.734	2.5	1	NF	16	9.05	–0.43	2.84
2	0.634	2.5	1	NF	16	6.09	–0.77	2.24
3	0.534	2.5	1	NF	16	9.01	–0.17	2

EXPERIMENTAL DETAILS

SS304, a base metal measuring 65×25×8 mm, was employed in the experiment. 304 stainless steel is highly resistant to oxidation and corrosion at high temperature, and is used for making complicated shapes because to its high elongation, low yield strength and excellent formability. Fluxes employed were SiO_2, TiO_2 and Cr_2O_3. Welding was done using an autogenous process. Current was varied from 120 to 160 A. First, butt welding with a root gap of 1 mm was performed as a trial experiment, followed by A-TIG welding with a flux containing a mixture of SiO_2, TiO_2 and Cr_2O_3 in various ratios, such as 72:18:10 (high value), 65:25:10 (mid value) and 45:45:10 (low value). The measured heat input (HI) values were 0.534 kJ/mm (low value), 0.634 kJ/mm (mid value) and 0.734 kJ/mm (high value). Root gap was kept fixed at 1 mm. GFR was varied from 12–16 l/min. Welded plates were cut using an abrasive cutter, and then ground and polished to a mirror finish on a belt grinder, on a disc grinder/polisher using emery paper grades of 400, 600, 800, 1000 and 1200, and using a velvet cloth soaked in alumina suspension. Kalling's No. 2 reagent was used to etch it. This solution was employed for around two minutes to etch the mirror-finish plates. The geometry of the weld beads was then determined using an optical microscope. Figure 1, *a*, *b* show the experimental setup for the present research.

The present investigation includes three key process items that have been identified as input process parameters: HI, FR and GFR. Furthermore, the outcome factors for the current research include WBW and DOP. Table 3 provides the parameters of the model as well as the different stages of the experiment.

According to Box–Behnken of Response Surface Methodology (RSM), in order to identify the most effective process parameters resulting in the highest penetration depth, for the 15 experimental runs shown in Table 5, a design with three factors and three levels was chosen. Table 4 shows the trial experimental findings for various input parameter combinations, as well as the associated experimental output data (WBW, DOP, and reinforcement). HI values are calculated by using equation mentioned below:

$$HI = \eta UI/(1000v).$$

Here, HI, HI values are expressed in kJ/mm; welding speed, v in mm/s; weld voltage, U and weld current, I are in Volt and Ampere respectively; η is process efficiency (for TIG welding, it is taken as 0.8).

Input parameters used are GFR, FR and HI. The design of experiment is made using three levels and three variables, as per Box–Behnken Design approach of RSM. Fifteen experimental runs are performed. Output parameters chosen are DOP, reinforcement and WBW. Shielding gas utilized is 99.9 % pure argon

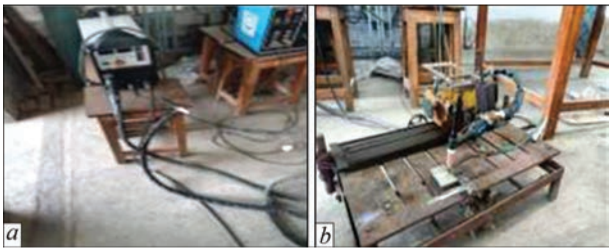

Figure 1. Welding machine (*a*), travelling vehicle (*b*)

Table 5. The experimental data

No	I, A	v, mm/s	U, V	HI, kJ/mm	FR	GFR, l/min	WBW, mm	Reinforcement, mm	DOP, mm
1	122	2.5	14.6	0.53436	2.5	12	6.31	–0.21	2.58
2	139	2.5	15.2	0.63447	2.5	14	9.25	–0.18	3.42
3	122	2.5	14.6	0.53436	4	14	7.57	–1.14	3.61
4	159	2.5	15.4	0.73458	2.5	12	6.54	–0.3	3.32
5	139	2.5	15.2	0.63447	4	12	7.63	–0.52	4.597
6	139	2.5	15.2	0.63447	1	12	6.79	–0.26	2.4
7	159	2.5	15.4	0.73458	2.5	16	6.73	0.17	3.45
8	159	2.5	15.4	0.73458	4	14	8.34	0.2	4.255
9	159	2.5	15.4	0.73458	1	14	7.82	–1.23	4.15
10	139	2.5	15.2	0.63447	2.5	14	8.45	–0.2	2.7
11	122	2.5	14.6	0.53436	2.5	16	7.37	0	3.08
12	139	2.5	15.2	0.63447	2.5	14	9.25	–0.2	2.91
13	122	2.5	14.6	0.53436	1	14	8.94	–0.28	4.14
14	139	2.5	15.2	0.63447	1	16	9.06	–0.5	5.7
15	139	2.5	15.2	0.63447	4	16	6.3	–0.23	2.44

gas, and gun angle is kept constant at 75° throughout. Weld bead microstructure is examined using both an optical microscope and a scanning electron microscope (SEM). Rockwell hardness tester is used to measure hardness. The optimal settings for the A-TIG welding process contain a HI of 0.634 kJ/mm, a FR (SiO_2:TiO_2:Fe_2O_3) of 45:45:10 and GFR of 16 l/min.

Figure 3, *a* shows weld beads created by autogenous A-TIG welding. Figure 3, *b* depicts deep penetration of 5.7 mm with a FR of 45:45:10, current of 150 A and GFR of 16 l/min and Figure 3, *a* shows a shallow DOP 2.58 mm with a weld current of 140 A, FR of 65:25:10 and GFR of 12 l/min has little effect on DOP.

RESULTS AND DISCUSSION OF EXPERIMENTAL OBSERVATION

The observed data in table 1 was inputted into the Minitab 17 program, and analysis of variance (ANOVA) tables, contour plots, and surface plots were generated using the software.

Figure 2. A-TIG welded specimens corresponding to respective experimental runs: *a* — weld joint in experiment 3; *b* — weld joint in experiment 9; *c* — weld joint in experiment 10; *d* — weld joint in experiment 12

ANOVA TABLE OF DOP WITH VARYING HI, FR, GFR

Table 6 contains the ANOVA table for DOP, while Figure 4, *a–f* shows the surface and contour plots with GFR as hold values.

The lowest HI and FR yield the maximum DOP. It changes slightly as the amount of HI increases. DOP displays a declining trend at the starting level with an increasing FR, and DOP practically remains constant after that.

DOP first decreases as HI increases, but then begins to expand. As FR increases, DOP first decreases before rising. The lowest DOP is seen at mid-range HI and FR. Maximum DOP is observed with high HI and FR.

At lower FR, DOP changes only somewhat with an increase in HI. However, at greater FR, DOP increases in response to an increase in DOP, on the other hand, increases dramatically when the FR increases for any HI amount. The regression relationship is relatively satisfactory since the R^2 (correlation coefficient) value

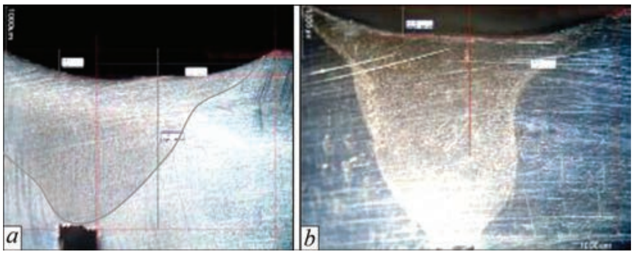

Figure 3. Photographs of weld beads: *a* — macrostructure at a set current 140 A; *b* — macrostructure at a set current 150 A

Table 6. ANOVA table for DOP

Source	Degrees of freedom	Adjusted sum of squares	Adjusted mean squares	Fisher value or F-statistics	PV
Model	9	11.4553	1.27282	16.58	0.003
Linear	3	1.0591	0.35304	4.6	0.067
HI, kJ/mm	1	0.3894	0.3894	5.07	0.074
FR	1	0.2768	0.27677	3.67	0.116
GFR	1	0.3929	0.37294	5.12	0.073
Square	3	2.8165	0.93883	12.23	0.01
HI, kJ/mm × HI, kJ/mm	1	0.1144	0.11437	1.49	0.277
FR × FR	1	2.685	2.68498	34.97	0.002
GFR × GFR	1	0.0228	0.02275	0.3	0.61
2-Way Interaction	3	7.5797	2.52658	32.91	0.001
HI, kJ/mm × FR	1	0.1008	0.10081	1.31	0.304
HI, kJ/mm × GFR	1	0.0342	0.03423	0.45	0.534
FR × GFR	1	7.4447	7.44471	96.97	0
Error	5	0.3839	0.07677	–	–
Lack-of-fit	3	0.1097	0.03655	0.27	0.847
Pure error	2	0.2742	0.1371	–	–
Total	14	11.8392	–	–	–

for DOP is 96.76 %, the static values of the model are close to zero, and the lack of fit is not significant, as shown in ANOVA Table 3. The surface and contour plots show that the largest DOP occurs when the HI is 0.70 kJ/mm or higher, and the FR is lower or larger. This graphic does not show a distinct trend. More experiments are needed to clarify this. Equation (1) is the DOP regression equation.

$$\begin{gathered}\mathrm{DOP} = 12.4 - 16.3\,\mathrm{HI} + 3.677\,\mathrm{FR} + 2.09\,\mathrm{GFR} + \\ + 17.6\,\mathrm{HI} \times \mathrm{HI} + 0.3790\,\mathrm{FR} \times \mathrm{FR} - 0.0196\,\mathrm{GFR} \times \\ \times \mathrm{GFR} + 1.057\,\mathrm{HI} \times \mathrm{FR} - 0.462\,\mathrm{HI} \times \\ \times \mathrm{GFR} - 0.4547\,\mathrm{FR} \times \mathrm{GFR}.\end{gathered} \tag{1}$$

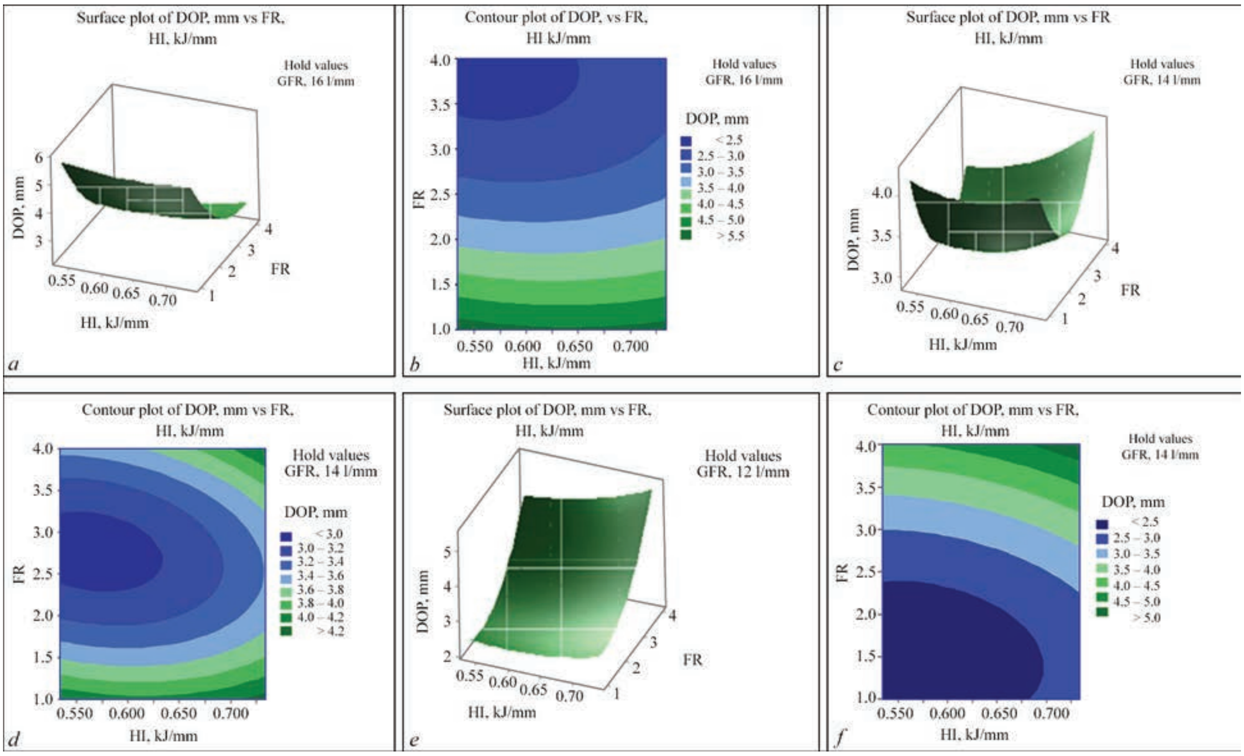

Figure 4. *a* — surface; *b* — contour plot of DOP (mm) for FR against HI with GFR held at 16 l/min; *c* — surface; *d* — contour plot of DOP (mm) for FR against HI with GFR held at 14 l/min; *e* — surface; *f* — contour plot of DOP (mm) for FR against HI with GFR held at 12 l/min

Table 7. ANOVA table of bead width

Source	Degrees of freedom	Adjusted sum of squares	Adjusted mean squares	Fisher value or F-statistics	PV
Model	9	15.6857	1.74285	14.97	0.004
Linear	3	1.6308	0.54361	4.67	0.065
HI, kJ/mm	1	0.0722	0.07220	0.62	0.467
FR	1	0.9591	0.95911	8.24	0.035
GFR	1	0.5995	0.59951	5.15	0.073
Square	3	9.7326	3.24421	27.86	0.002
HI, kJ/mm × HI, kJ/mm	1	2.1420	2.14204	18.39	0.008
FR × FR	1	0.0108	0.01083	0.09	0.773
GFR × GFR	1	8.1332	8.13323	69.84	0.000
2-Way interaction	3	4.3222	1.44075	12.37	0.009
HI, kJ/mm × FR	1	0.8930	0.89302	7.67	0.039
HI, kJ/mm × GFR	1	0.1892	0.18923	1.62	0.258
FR × GFR	1	3.2400	3.24000	27.82	0.003
Error	5	0.5822	0.11645	–	–
Lack-of-fit	3	0.1556	0.05186	0.24	0.862
Pure error	2	0.4267	0.21333	–	–
Total	14	16.2679	–	–	–

ANOVA TABLE OF WBW WITH VARYING HI, FR, GFR

Table 7 shows the ANOVA table for WBW. Figure 5, *a–f* shows the hold value, surface plot, and contour plot for the GFR.

Initially, bead width changes somewhat when HI increases in the lower range of FR. Then it exhibits a diminishing tendency with increasing HI. However, with greater FR, bead width decreases with increased HI. On the other hand, at greater HI levels, bead width decreases significantly with increasing FR. Melt vol-

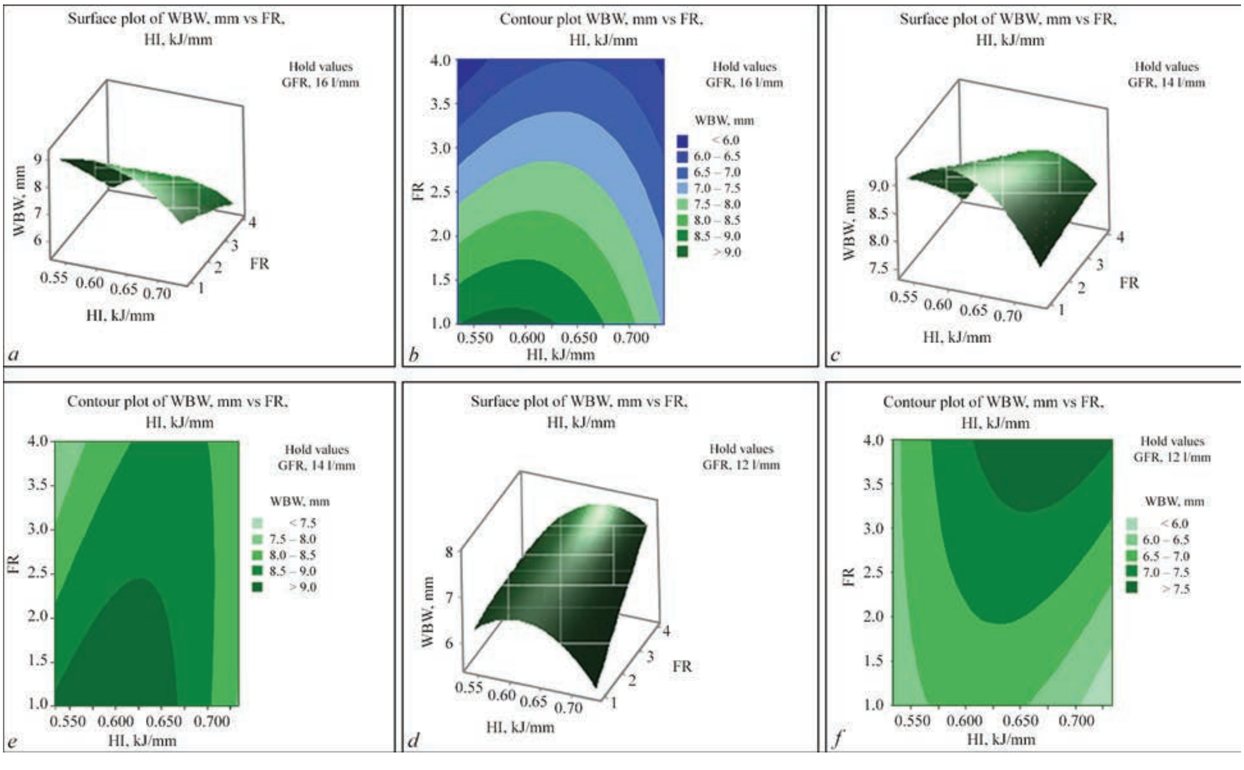

Figure 5. *a* — surface; *b* — contour plot of bead width (mm) for FR against HI with GFR held at 16 l/min; *c* — surface plot; *d* — contour plot of bead width (mm) for FR against HI with GFR held at 14 l/min; *e* — surface plot; *f* — contour plot of bead width (mm) for FR against HI with GFR held at 12 l/min

ume naturally increases as HI increases. If it directly increases DOP, it has little effect on bead width. When DOP is not adjusted, the bead width rises, resulting in less reinforcing.

Initially, bead width increases somewhat with increased HI in the lower FR range. Then it displays a diminishing trend as HI increases. However, with greater FR, bead width increases marginally as HI increases. On the other hand, bead width increases with increasing FR at greater HI levels.

Bead width first increases somewhat with an increase in HI across all FR ranges. It then exhibits a diminishing trend as the HI increases. However, with greater FR, bead width increases as HI increases. Bead width, on the other hand, increases dramatically as the FR increases across a wider range of HI.

Because the R^2 value of bead width is 96.42 % and static values of probability value (PV) are close to zero, as shown in ANOVA Table 7, the regression relation is acceptable. The surface plot and contour plot show that the greatest bead width occurs in the lower range of HI, while the FR is undecided. More thorough studies may be performed to investigate the presence of any specific trend, if any. Equation (2) presents the regression equation for bead width.

$$\begin{gathered}\mathrm{WBW} = -110.4 + 102.8\,\mathrm{HI} + 2.09\,\mathrm{FR} + 11.97\,\mathrm{GFR} - \\ - 76.0\,\mathrm{HI} \times \mathrm{HI} - 0.024\,\mathrm{FR} \times \mathrm{FR} - 0.370\,\mathrm{GFR} \times \\ \times \mathrm{GFR} + 3.15\,\mathrm{HI} \times \mathrm{FR} - 1.086\,\mathrm{HI} \times \\ \times \mathrm{GFR} - 0.3000\,\mathrm{FR} \times \mathrm{GFR},\end{gathered} \tag{2}$$

when, bead width is in mm, HI is in kJ/mm and GFR is in l/min.

OBSERVATION OF MICROSTRUCTURE

Figure 6 shows the microstructure of the best welded sample No. 8. Figure 6, *a* depicts the microstructure as seen using an optical microscope, whereas Figure 6, *b* shows it via a SEM. Both optical and scanning electron microscopy (SEM) observations reveal the formation of black granular formations known as ferrite structures and white granular structures known as pearlite. Ferrite is α iron, while cementite is an intermetallic complex (Fe_3C, iron carbide).

MODELLING USING ANN

An ANN is a nonlinear computer model comprising several neurones that communicate with one another in the same way as a biological nervous system does. In the present research, we use the Levenberg–Marquardt multilayer error back propagation training algorithm (EBPTA) to train feed forward ANN. This strategy uses the iterative gradient technique to compute connection weights that minimise the total means-square error between the algorithm's output and the intended outcome. Figure 7 depicts a wide framework for the present research on weld bead form. The current study was conducted using Matlab17 software and the neural network toolbox. The multilayered ANN model consists of three input layers (HI, FR, and GFR), three output levels (WBW, DOP, and reinforcement), and a hidden layer of ten nodes. Table 5 illustrates the experimental data utilised in the ANN investigation. The training, testing, and validation ratios are set as 70, 15, and 15 % for the 15 data sets, respectively. The maximum number of epochs allowed in ANN analysis is 1000. The iterative method's beginning and maximum convergence factors (μ) are 0.001 and $1.00e^{10}$. The minimal performance gradient (MSG) during training is $5.05e^{-9}$. The experimental DOP and WBW are the objectives here. The outcome is calculated by taking the ANN model's penetration depth and WBW into account.

Table 8. Summary of processes (training, validation and testing)

Process	Observation	MSG	R ???
Training	11	0.2394	0.9989
Validation	2	0.3451	0.9415
Test	2	0.3212	0.9809

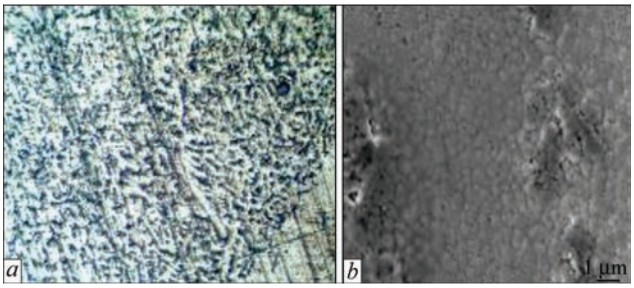

Figure 6. Microstructure observed of weld bead of sample 9 (*a*) by optical microscope with ×200 magnifications and (*b*) by SEM with ×1000 magnification

Throughout training, validation, and testing, the model's *R* (coefficient of correlation) values are vir-

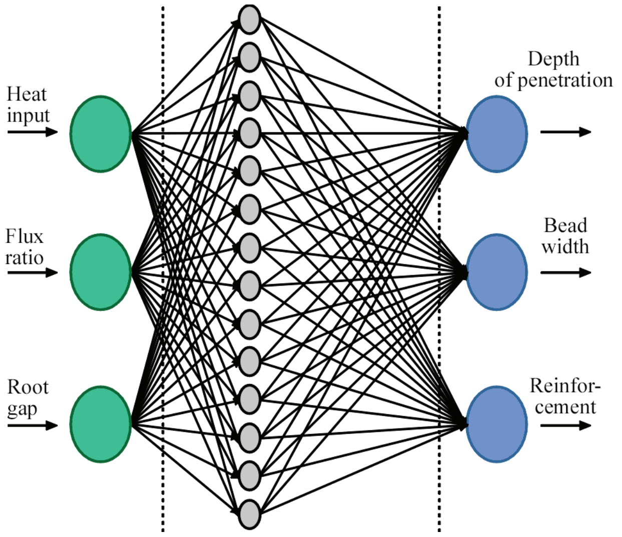

Figure 7. Neural network model schematic for forecasting bead width and penetration

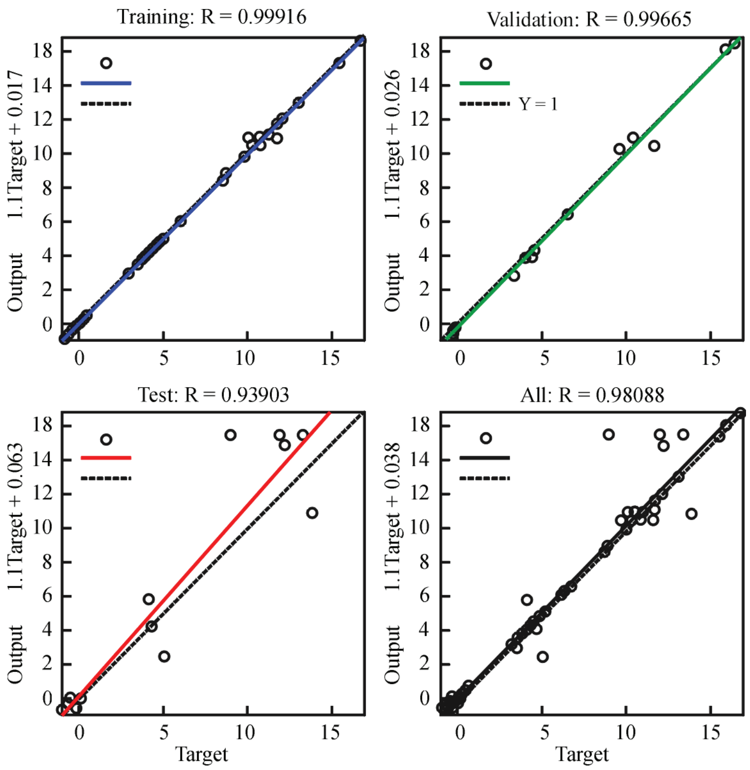

Figure 8. Regression plot analysis

tually same, but its MSG (mean square error) values are much lower. Thus, this ANN model is considered while making predictions. A value of *R*, as shown in Table 8, is appropriate for a number of tasks such as training, validation, and testing since it evaluates goodness-of-fit. Statistically significant changes in the independent factors balance out with changes in the dependent variables.

The experimental network's regression curve, shown in Figure 8, shows a significant relationship between the training, validation, and testing stages. The generated model is strong, as indicated by regression values approaching Black line is the main regression line. It shows the central trend of the data. Red line represents confidence interval boundary. Blue line represents fitted values or predictions. Green line represents smoothed fit.

RESULTS AND DISCUSSIONS

Table 9 and Figure 9, *a* compare the experimental and expected WBW values of the 15 experimental

Table 9. Bead width (predicted data and experimental data with percentage error)

No.	WBW (Experimental)	WBW (Predicted)	Percentage Error
1	7.64	7.65	0.13
2	8.35	8.43	0.94
3	7.81	7.77	0.51
4	7.97	7.95	0.25
5	8.77	8.74	0.34
6	8.8	8.79	0.11
7	8.89	8.85	0.45
8	8.58	8.54	0.46
9	8.77	8.81	0.45
10	9.29	9.33	0.42
11	8.82	8.86	0.45
12	9.09	9.12	0.32
13	7.68	7.72	0.51
14	8.69	8.73	0.45
15	9.09	9.18	0.98

Table 10. DOP (predicted and experimental with error)

No.	DOP (Experimental)	DOP (Predicted)	Percentage Error
1	2.58	2.6	0.77
2	3.42	3.44	0.58
3	3.61	3.6	0.27
4	3.32	3.31	0.3
5	4.597	4.609	0.26
6	2.4	2.41	0.41
7	3.45	3.46	0.28
8	4.25	4.24	0.23
9	4.15	4.17	0.47
10	2.7	2.71	0.36
11	3.08	3.082	0.06
12	2.91	2.9	0.34
13	4.14	4.11	0.72
14	5.7	5.75	0.86
15	2.44	2.42	0.82

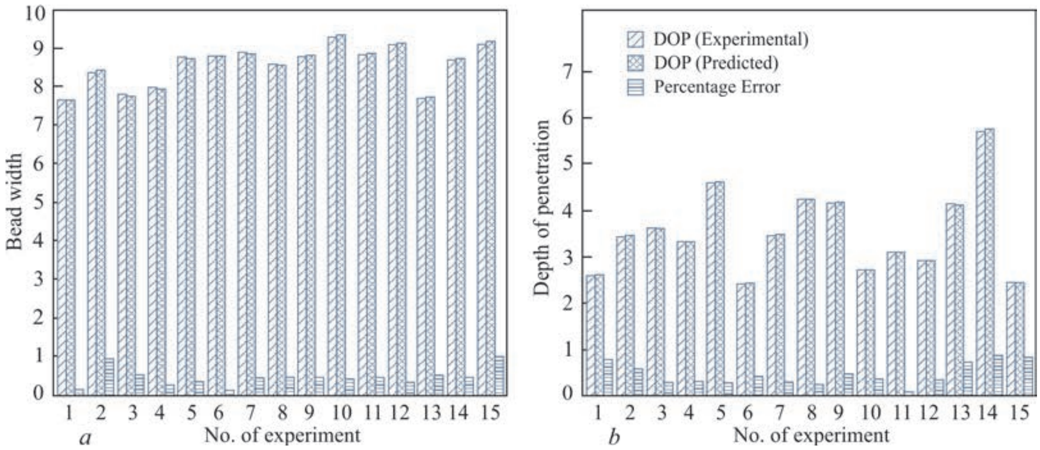

Figure 9. Bar graph showing difference between experimental and predicted WBW **or simply bead width** (*a*), bar graph showing difference between the experimental and predicted penetration (*b*)

Table 11. Input parameters (minimum, maximum, mean, standard deviation)

No	Input parameters	Min. value	Max. value	Mean value	Standard deviation
1	HI, kJ/mm	0.534	0.734	0.634	0.0731
2	FR	1	4	2.5	1.0954
3	GFR, l/min	12	16	14	1.4605

Table 12. Output parameters (minimum, maximum, mean, standard deviation)

No	Output parameters	Min. value	Max. value	Mean value	Standard deviation
1	WBW, mm	6.3	9.25	7.756	1.0414
2	DOP, mm	2.4	5.7	3.516	0.8884

runs, whereas Table 10 and Figure 9, *b* illustrate the experimental and anticipated DOP values. There are minor departures from the predicted values of bead geometry i.e. WBW and DOP in certain experimental runs, but overall there is satisfactory agreement. The authors predict the result while keeping stable input and output nodes by adjusting the amount of training data sets, hidden layers, and hidden nodes through trial and error. It is not uncommon to discover disparities between experimental and expected results using ANN.

Using the data allocated for validation, Figure 10 presents a graphical depiction of performance during the validation step. A maximum of 1000 epochs can be used with the ANN model. With the lowest prediction error, the fifth epoch of the eleven repetitions yielded the best validation performance. The starting value is zero and the ending value is eleven as the training progresses. It is assumed that the MSG values for training, validation, and testing are 0.2394, 0.3451, and 0.3212, respectively. The R values are nearly one, while the MSG values are almost zero. Thus, the ANN architecture that was used was successful.

Table 11 displays the minimum, maximum, mean, and standard deviation of the input parameters, while Table 12 displays the minimum, maximum, mean, and standard deviation of the replies, or output parameters.

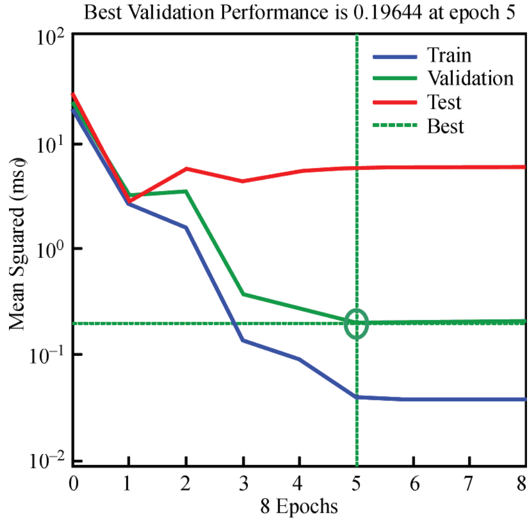

Figure 10. Graph of the best validation performance

CONCLUSIONS

Based on the experimental investigation on A-TIG welding of SS304 steel flats by utilizing a ternary flux combination (SiO_2:TiO_2:Cr_2O_3), data analysis with the help of ANOVA and applying ANN for prediction of bead geometry, the following conclusions may be drawn:

With a HI of 0.634 kJ/mm, root gap of 1 mm, GFR of 16 l/min and FR of 45:45:10, maximum DOP of 5.7 mm is achieved.

The DOP and width of the weld bead are more influenced by HI and FR.

We may conclude that the ANOVA regression analysis is satisfied in this situation because the PV values of the ANOVA table for the DOP and bead width are often less than 0.05 and the lack of fit is insignificant.

The bead width has an R^2 value of 96.42 % while the DOP has an R^2 value of 96.76 %. The results, therefore, are more than 90 % and pretty acceptable.

Based on measurements made with a Rockwell hardness testing machine, the maximum hardness value for the A-TIG weldment is 65 *HRC*. It is quite satisfactory.

The A-TIG welding bead width and penetration depth determined by ANN are found to be fairly close to the experimental value. Minor differences are also observed from time to time, and this is normal. The ANN model has been successfully applied in this case. Consequently, it can be said that the ANN is a helpful tool for estimation.

REFERENCES

1. Akhonin, S.V., Bilous, V.Yu., Selin, R.V., Petrychenko, I.K. (2020) Impact of TIG welding on the structure and mechanical properties of joints of pseudo-β-titanium alloy. *The Paton Welding J.,* **2**, 9–15. DOI: https://doi.org/10.37434/tpwj2020.02.02
2. Kovalenko, D.V., Pavlyak, D.A., Sudnik, V.A., Kovalenko, I.V. (2010*)* Adequacy of thermohydrodynamic model of through penetration in TIG and A-TIG welding of Nimonic-75 Nickel alloy. *The Paton Welding J.,* **10**, 2–6.
3. Dadfar, M., Fathi, M.H., Karimzadeh, F. et al. (2007) Effect of TIG welding on corrosion behavior of 316L stainless steel. *Materials Letters,* **61**, 2343–2346. DOI: https://doi:10.1016/j.matlet.2006.09.008
4. Mohan, P. (2014) Study of the effects of welding parameters on TIG welding of aluminium plate. *Masters Dissertation,* NIT Rourkella.
5. Kovalenko, D.V., Kovalenko, I.V., Zaderii, B.O., Zviagintseva, G.V. (2022) Application of A-TIG welding for improving the technology of manufacturing and repair of units of gas turbine engines and installations from titanium alloys. *The Paton Welding J.,* **10**, 3–11. DOI: https://doi.org/10.37434/tpwj2022.10.01
6. Yushchenko, K.A., Kovalenko, D.V., Kovalenko, I.V. (2001) Application of activators for TIG welding of steels and alloys. *The Paton Welding J.,* **7**, 37–43.
7. Kumar, S.A., Sathiya, P. (2015) Experimental investigation of the A-TIG welding process of Incoloy 800H. *Materials and Manufacturing Processes,* **30**, 1154–1159.
8. Babbar, A., Kumar, A., Jain, V., Gupta, D. (2019) Enhancement of Activated TIG welding using multi component TiO_2–SiO_2–Al_2O_3 hybrid flux, *Measurement,* **148**, 106912/1-16 DOI: https://doi.org/10.1016/j.measurement.2019.106912
9. Tathgir, S., Bhattacharya, A. (2015) Activated-TIG welding of different steels: Influence of various flux and shielding gas. *Materials and Manufacturing Processes,* **31**, 335–342. DOI: https://doi.org/10.1080/10426914.2015.1037914
10. Saha, S., Das, S. (2018) Investigation on the effect of activating flux on tungsten inert gas welding of austenitic stainless steel using AC polarity. *Indian Welding J.,* **51**, 84–92. DOI: https://doi.org/10.22486/iwj.v51i2.170313
11. Venkatesan, G., George, J., Sownyasri, M., Muthupandi, V. (2014) Effect of ternary fluxes on depth of penetration in A-TIG welding of AISI 409 ferritic stainless steel. *Procedia Materials Sci.,* **5**, 2402–2410. DOI: https://10.1016/j.mspro.2014.07.485
12. Ganesh, K.C., Balasubramanian, K.R., Vasudevan, M. et al. (2016) Effect of multipass TIG and activated TIG welding process on the thermo-mechanical behavior of 316LN stainless steel weld joints. *Metallurgical and Materials Transact. B*, **47**, 1347–1362. DOI: https://doi.org/10.1007/s11663-016-0600-6
13. Pamnani, R., Vasudevan, M., Vasantharaja, P., Jayakumar, T. (2015) Optimization of A-GTAW welding parameters for naval steel (DMR 249 A) by design of experiments approach. *J. of Materials Design and Applications,* **34**, 1–12. DOI: https://doi.org/10.1177/1464420715596455
14. Kumar, V.B., Lucas, D., Howse, G. et al. (2009) Investigation of the A-TIG mechanism and the productivity benefits in TIG welding. In: *Proc. of the Fifteenth Inter. Conf. on the Joining of Materials,* 15.
15. Vora, J.J., Badheka, V.J. (2017) Experimental investigation on microstructure and mechanical properties of activated TIG welded reduced activation ferritic/martensitic steel joints. *J. of Manufacturing Processes,* **25**, 85–93.
16. Kulkarni, A., Dwivedi, D.K., Vasudevan, M. (2019) Dissimilar metal welding of P91 steel-AISI 316L SS with Inconel 800 and Inconel 600 interlayers by using activated TIG welding process and its effect on the microstructure and mechanical properties. *J. of Materials Proc. Technol.,* **274**, 116–128. DOI: https://doi.org/10.1016/j.jmatprotec.2019.116280
17. Touileb, K., Hedhibi, A.C., Djoudjou, R. et al. (2022) Mechanical, microstructure, and corrosion characterization of dissimilar austenitic 316L and Duplex 2205 stainless-steel ATIG welded joints. *Materials,* **15**, 1–21. DOI: https://doi.org/10.3390/ma15072470
18. Howse, D.S., Lucas, W. (2000) Investigation into arc constriction by active fluxes for tungsten inert gas welding. *Sci. and Technol. of Welding and Joining,* **5**, 189–193. DOI: https://doi.org/10.1179/136217100101538191
19. Saha,, S., Paul, B.S., Das, S. (2021) Productivity improvement in butt joining of thick stainless steel plates through the usage of activated TIG welding. *SN Applied Sci.,* **3**, 416/1-10. DOI: https://doi.org/10.1007/s42452-021-04409-7
20. Acharya, S., Das, S. (2023) A review on the use of activating flux in gas tungsten arc welding towards obtaining high productivity. *Manufacturing Technology Today*, **22**, 12–28. DOI: https://doi.org/10.58368/MTT.22.7-8.2023.12-28
21. Vidyarthy, R.S., Dwivedi, D.K. (2016*)* Activating flux tungsten inert gas welding for enhanced weld penetration. *J. of Manufacturing Processes,* **22**, 211–228. DOI: https://doi.org/10.1016/j.jmapro.2016.03.012
22. Nanavati, P.K., Badheka, V.J., Idhariya, J., Solanki, D. (2021) Comparisons of different oxide fluxes in activated gas tungsten arc welding of duplex stainless steels for improved depth of penetration and pitting corrosion resistance. *Advances in Materials and Processing Technologies,* **8,** 2533–2550. DOI: https://doi.org/10.1080/2374068X.2021.1916283

23. Acharya, S., Gonda, D., Das, S. (2022*)*. Achieving favourable depth of penetration and productivity of ATIG welds utilising the AHP. *Indian Sci. Cruiser,* **36**, 24–30. DOI: https://doi.org/10.24906/isc/2022/v36/i5/218005
24. Acharya, S., Gonda, D., Das, S. et al. (2023) Augmentation of depth of penetration and productivity benefits of ATIG welds using the AHP. *Inter. J. of Analytical Hierarchy Process,* **15**, 1–20. DOI: https://doi.org/10.13033/ijahp.v15i3.1120
25. Berthier, A., Paillard, P., Carin, M. et al. (2012) TIG and A-TIG welding experimental investigations and comparison to simulation. *Sci. and Technol. of Welding and Joining,* **17**, 609–615. DOI: https://doi.org/10.1179/1362171812y.0000000024
26. Vora, J.J., Abhishek, K., Srinivasan, S. (2015) Attaining optimized ATIG welding parameters for carbon steels by advanced parameter-less optimization techniques: with experimental validation. *J. of the Brazilian Society of Mechanical Sci. and Eng.,* **41**, 260–280.
27. Gurevich, S.M., Zamkov, V.N., Kushnirenko, N.A. (1965) Improving the penetration of titanium alloys when they are welded by argon tungsten arc process. *Avtomaticheskaya Svarka,* **9**, 1–4.
28. Ates, H. (2007) Prediction of gas metal arc welding parameters based on artificial neural networks. *Materials & Design,* **28**, 2015–2023.
29. Pal, S., Pal, S.K., Samantaray, A.K. (2008) Artificial neural network modelling of weld joint strength prediction of a pulsed metal inert gas welding process using arc signals. *J. of Materials Proc. Technology,* **202**, 464–474.
30. Nagesh,D.S., Datta, G. L. (2010) Genetic algorithm for optimization of welding variables for height to width ratio and application of ANN for prediction in TIG welding process. *Applied Soft Computing,* **10**, 897–907. DOI: https://doi.org/10.1016/j.asoc.2009.10.007
31. Owunna, I., Ikpe, A.E. (2019) Modeling and prediction of the mechanical properties of TIG weld joint for AISI 4130 low carbon steel plates using artificial neural network (ANN) approach. *Nigerian J. of Technology,* **38**, 117–126. DOI: http://dx.doi.org/10.4314/njt.v38i1.16
32. Acharya, S., Gonda, D., Das, S. (2024) Artificial neural networks based prediction of penetration in activated tungsten inert gas welding. *Indian Welding J.*, **5**, 71–79. DOI: https://doi.org/10.22486/iwj.v57i1.223729
33. Acharya, S., Patra, S., Das, S. (2024). Predicting A-TIG weld bead geometry using artificial neural networks. **4**, 12. DOI: https://doi.org/10.21203/rs.3.rs-5277673/v1

ORCID

Samarendra Acharya: 0000-0002-8337-8839,
Soumyadip Patra: 0009-0007-7946-9678,
Santanu Das: 0000-0001-9085-3450

CONFLICT OF INTEREST

The Authors declare no conflict of interest

CORRESPONDING AUTHOR

Santanu Das
Department of Mechanical Engineering, Kalyani Government Engineering College, Kalyani, 741235, West Bengal, India.
E-mail: sdas.me@gmail.com

SUGGESTED CITATION

Samarendra Acharya, Soumyadip Patra, Santanu Das (2025) Employing artificial neural networks to estimate weld bead geometry in A-TIG welds. *The Paton Welding J*., **3**, 13–23.
DOI: https://doi.org/10.37434/tpwj2025.03.02

JOURNAL HOME PAGE

https://patonpublishinghouse.com/eng/journals/tpwj

Received: 19.11.2024
Received in revised form: 13.03.2025
Accepted: 26.04.2025

DOI: https://doi.org/10.37434/tpwj2025.03.03

INFLUENCE OF HEAT TREATMENT ON THE STRUCTURE, PROPERTIES AND DURABILITY OF FLAT TUNGSTEN CATHODES

L.A. Krushinska[1], **Ya.A. Stelmakh**[1], **R.A. Tkach**[2], **O.O. Yukalchuk**[2], **A.A. Dudnik**[3]

[1]E.O. Paton Electric Welding Institute of the NASU
11 Kazymyr Malevych Str., 03150, Kyiv, Ukraine

[2]State-run Company "International Center for Electron Beam Technologies
of the E.O. Paton Electric Welding Institute of the NASU"
68 Antonovich Str., 03150, Kyiv, Ukraine

[3]LLD "TANGSTEN"
19a Dniprovska Naberezhna, of. 33, 02081, Kyiv, Ukraine

ABSTRACT

The effect of heat treatment on the structure and properties of flat tungsten thermionic cathodes (W-cathodes) obtained by hot pressing (flattening) of blanks from 99.99 % pure tungsten wire was investigated. The effect of temperature (800–1200 °C) and vacuum annealing time (0.3–2.0 h) on the formation of a recrystallization structure in W-cathodes was studied; comprehensive comparative studies of the structure, mechanical and operational properties were carried out. It was found that to increase the service life of W-cathodes a mixed structure should be formed in them in the following quantitative ratio: 5–25 % — equiaxed recrystallized grains 1–8 μm in size; the remaining volume of the cathode material should retain the original oriented structure.

KEYWORDS: thermionic cathodes, tungsten, electron beam installations, recrystallization, microstructure

INTRODUCTION

Electron beam guns (EPG) are widely used to conduct the processes of meting, evaporation and condensation in vacuum. Their consumable elements are tungsten thermionic cathodes (W-cathodes), which are the source of electrons. This most important EBG component determines the electric, energy and service properties of vacuum electron beam installation (EBI). W-cathodes with a flat surface (in the form of plates) are widely applied now as electron sources for industrial processes. Electron emission occurs, when these cathodes are heated to high temperature [1–3].

The cathode service life is determined by the speed of its geometry change (elongation, distortion, etc.) during high-temperature service and repeated heating-cooling cycles, leading to deterioration of the beam shape and need for cathode replacement. According to patent information, the main attention is paid to development of variants of the flat cathode design, while preserving polycrystalline tungsten as the material [2–5]. In practice it turned out that not only the design determines the cathode service properties, but also the material from which it is made. However, in application of alloys of tungsten (for instance single-crystal W-4 % Ta alloy [6]) and tungsten doped with SiO_2, K_2O, Al_2O_3 additives [7], as well as tungsten with To, Ta, Re coating [8] as flat cathode materials, a significant limitation of their application sphere was found (REM coatings are used predominantly for indirectly heated cathodes). Therefore, tungsten remains a priority material for directly heated thermionic cathodes. Unfortunately, there are practically no data in publications as regards high-temperature studies of the structure-properties-performance complex of cathodes from pure W.

Two processes: deformation and recrystallization are widely used during cathode manufacture. In order to improve the required material characteristics, it is important to select the optimal modes of impact on it. Local W-cathodes are produced from wire under plant conditions during a multistage process, alternating pressing and heat treatment [3, 9]. However, the need to upgrade the technologies of manufacturing W-cathodes for EBG in terms of improvement by the cost/effectiveness criterion remains important and relevant to this day, and it became particularly urgent now under the conditions of import substitution and saving of costly metals.

The objective of this work was development of the modes of heat treatment (HT) for material of the already supplied W-cathodes, to improve the properties required to increase their service life.

MATERIALS AND METHODS OF INVESTIGATION

W-cathodes supplied for use in EBG, are plates 0.6 mm thick, 3 mm wide and 100–140 mm long. Their manufacturing method is multistage hot pressing of blanks from tungsten wire of 99.99 % purity described in literature [3, 9]. Total degree of deformation is estimated to be equal to 60–65 %.

Cathodes for investigations were selected randomly from three cathode batches of the total amount of 1000 pcs, produced by “TANGSTEN” Ltd. (Kharkiv) in 2023.

To determine the initial temperature of recrystallization and study the dynamics of its processes, vacuum annealing of the supplied W-cathodes was conducted, for 1 h at different temperatures in the range from 800 to 1200 °C, as well as isothermal annealing in vacuum at 1200 °C in the time interval of 20–120 min.

Structural changes were controlled using optical (Polyvar Met) and scanning electron microscopy (Cam Scan 4D). Computer analysis of the images and statistical data processing with “Media cybernetics image analysis program”’ Image-Pro Plus version 6.0 software was applied to study the structural changes in W-cathodes.

Mechanical properties were assessed on the base of measurements of Vickers microhardness (*HV*), using Micro Duromate 4000E attachment to optical microscope, and by automatic microindendation method (Berkovich indenter) with automatic recording of the load diagram (indenter driving into the material) in MicronGamma instrument [10].

Service properties were determined when testing under the actual conditions of cathode operation in EBG of PE-123 in EBI of UE-202 and UE-210 type [2]. The cathode was mounted in the EBG cathode head, having first controlled the tension of the spring, stretching the cathode. A tungsten tablet 70 mm in diameter was used as evaporation material, which was placed into the water-cooled crucible. In operation, in addition to constant mechanical loads, the cathode is also exposed to multiple cyclic temperature loads. The test cycle simulated the temperature profile of cathode operation, and it consisted of the following stages: cathode heating and entering the operating mode (beam current of about 1.3 A, 60 mm diameter of the electron beam) for 1 min, working in this mode for 30 min, cathode switching off and cooling — 10 min. Test cycles lasted up to violation of electron beam geometry (beam spot going beyond the crucible limits in the operating mode), which was followed by recoding the total time of cathode working in the operating mode.

RESULTS AND THEIR DISCUSSION

Cathode microstructure in as-delivered state is polycrystalline and fibrous (Figure 1, *a*). Note that in both the sections made in the transverse and longitudinal directions of the cathode, the structure is homogeneous, its morphology is the same, and consists of elongated grains with average width of 3–5 μm, their length is 40–100 μm, individual grains reaching the length of 200 μm. No anisotropy of mechanical properties was found, either. Obtained microhardness values of 5.4–5.6 GPa are characteristic for both the directions.

One of the important characteristics, determining metal behaviour during HT, is the start of recrystallization, which has a significant influence on the change of physical-mechanical properties of structural materials. As determined by A.A. Bochvar, the temperature of the start of recrystallization (*TR*) is related to absolute melting temperature by the following relationship: $TR\ 0.4T_m$ (T_m W = 3680 K). Known recrystallization diagrams [11] also allow assessing *TR* in advance, depending on the value of preliminary deformation. According to literature data, the temperature of the start of initial recrystallization for unalloyed tungsten is in the range of *TR* = 1373–1573 K (1100–1300 °C) [12, 13].

However, *TR* depends on many parameters, which determine its more accurate value [14]. Three factors: amount of preliminary deformation, heating temperature (*T*) and holding duration (τ) have the strongest influence on the recrystallization process and determine the final grain size and mechanical properties of the material. At fixed amount of deformation (unchanged manufacturing conditions) two more factors remains, which require précising *TR* for the studied W-cathodes — *T* and τ.

Conducted analysis of the dependence of W-cathode microhardness on vacuum annealing temperature (*T*) in the selected temperature range of 800–1200 °C at fixed holding (τ = 1 h) showed that microhardness values do not change right up to 1000 °C (Figure 2), and only after reaching the temperature of 1100 °C, the microhardness slightly decreases (by 3–4 %). No visible changes in the microstructure were found up to the temperature of 1100 °C with the selected investigation methods. Noticeable changes in the microstructure occur in the case of temperature rising up to 1200 °C. New equiaxed grains form against the background of the initial structure (Figure 1), which is accompanied by microhardness lowering by 10 % compared to the initial one (Figure 2). Obviously, in our case, increasing of annealing temperature of W-cathodes to 1200 °C, and holding for 1 h actively stimulate the start of the initial recrystallization process. Further detailed studies of the kinetics of this process were conducted at the temperature of 1200 °C.

It was found that after isothermal annealing operations a two-phase microstructure forms in the entire

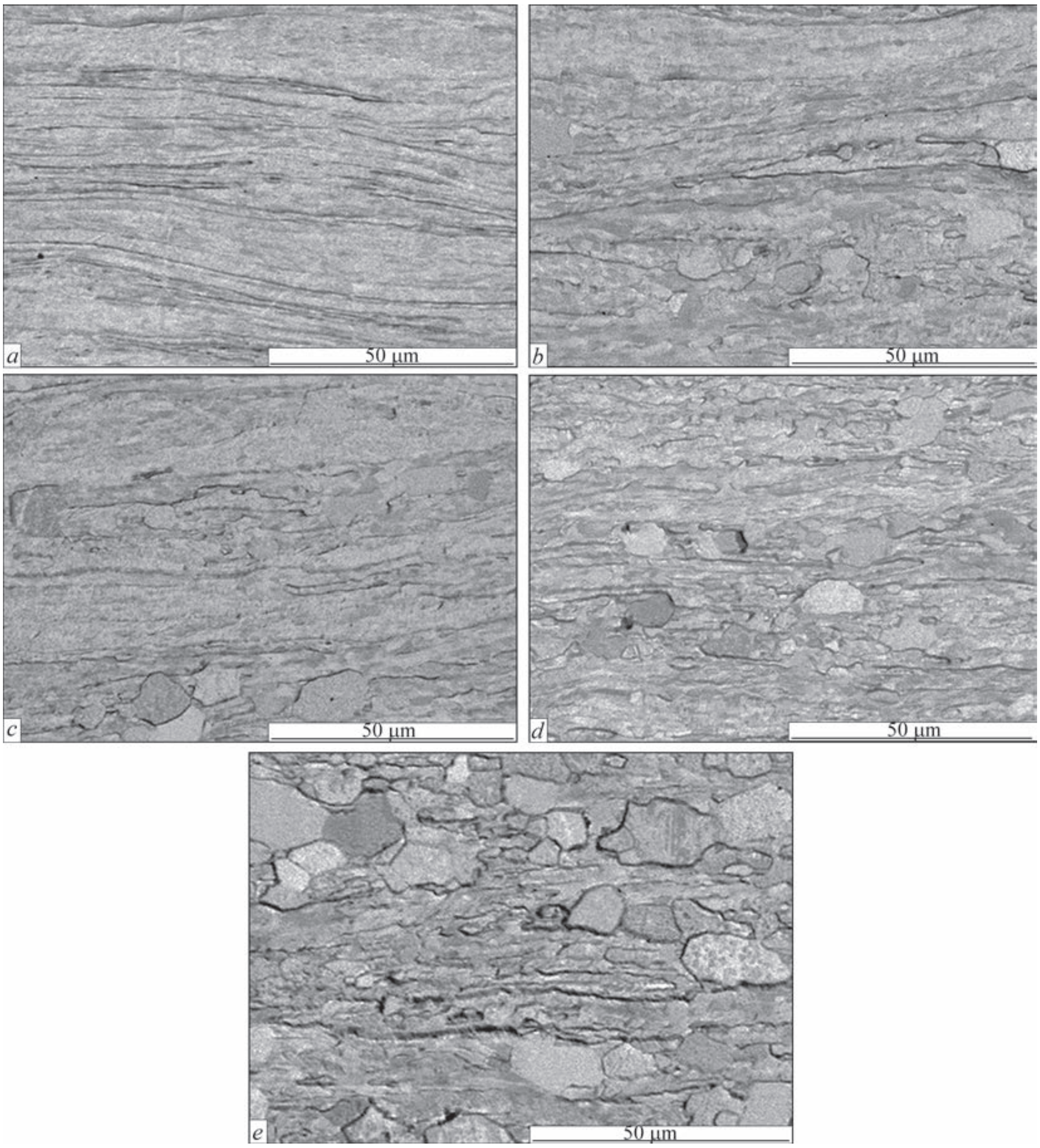

Figure 1. W-cathode structure: *a* — in as-delivered state; *b*–*e* — after vacuum annealing at the temperature of 1200 °C and annealing time of 30, 50, 80 and 120 min, respectively

studied time interval (τ = 20–120 min), which is a mixture of initial elongated and equiaxed recrystallized grains (Figure 1).

As recrystallized grains present in the structure have a wide range of sizes (for instance, from 2 to 21 μm at τ = 90 min), the value of the average grain size can distort the information about the occurring processes. As a result of the performed computer processing of microstructure images and statistical analysis, curves of frequency distribution of grains by size were plotted for W-cathodes, annealed during different τ at the temperature of 1200 °C. The distribution curves were used to determine the probable grain size *d* for each of the studied τ, and the results are given in Figure 3 (curve *1*). Change in the volume fraction of recrystallized *V* phase with greater holding time is shown in Figure 3 (curve *2*).

Given dependencies demonstrate that for W after deformation processing, as in our case, fine equiaxed grains of 1 μm size were detected already after 20 min of isothermal holding. The recrystallized phase volume was 5 %.

With increase of the duration of isothermal annealing (τ), grain size *d* and their volume fraction in the cathode material are increased simultaneously (Fig-

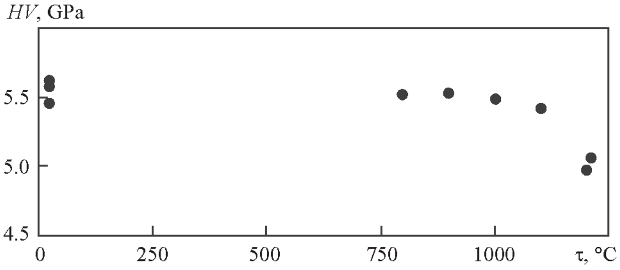

Figure 2. Dependence of tungsten cathode microhardness on vacuum annealing temperature (τ = 60 min)

ure 3, curves *1*, *2*). The processes run more actively in τ interval from 20 to 60 min, and their slowing down is observed at $\tau > 60$ min.

Note that with τ increase part of the grains are coarsened, but new ones also appear. Thus, the structures recorded by us in the entire interval of annealing time (Figure 1) form as a result of superposition of two parallel processes: the process of new fine grain formation proceeds together with growing of the already formed grains. Thus, even at maximum $\tau = 120$ min, initial recrystallization is incomplete, and the volume of the recrystallized phase in this case is not more than 60 %. Based on the generated data on the structure in the longitudinal and transverse directions we can assume that partial recrystallization runs homogeneously through the entire volume of cathode material.

Structural changes correlate with the change in mechanical properties of W-cathodes. With τ increase, a monotonic lowering of microhardness HV from 5.5 GPa in the initial state to 4.7–4.9 GPa takes place ($\tau = 120$ min) (Figure 4). This corresponds to the known fact that the processes of initial recrystallization are accompanied by lowering of internal stress and strength of material. However, taking into account the incomplete recrystallization and the volume taken up by it the resulting reduction of cathode material microhardness is not higher than 13 %.

The key factor ensuring the object strength, as well as a measure of elasticity of the material, from which it is made, is the Young's modulus (E). In the work E was calculated by the obtained load-hold-unload diagrams in the coordinates of load — depth of indenter penetration by the procedure described in a number of works [10, 15]. Resultant average E value for each of τ is taken from calculations of not less than ten measurements. Figure 4 shows changes in the modulus of elasticity of W-cathodes, depending on the time of annealing at unchanged temperature of 1200 °C.

Average value of the modulus of elasticity of W-cathodes in the initial state is equal to 213 GPa. The difference in E values obtained in the longitudinal and transverse sections of the cathodes is small, being within the instrument error.

With increase of holding time at annealing E changes nonmonotonically: after increasing to maximal value of 263–270 GPa in τ time interval from 20 to 50 min its noticeable lowering occurs, and after 90 min of holding the modulus of elasticity of annealed tungsten cathodes is below the initial one.

All the obtained E values are in the range of 180–270 GPa. This is less than the values of the modulus of elasticity $E0$ for a massive single-crystal tungsten sample, according to the reference data, $E0$ 400–411 GPa [13], and the experimentally derived value $E0 = 355$ GPa for polycrystalline W [16]. It is, however, higher than the value of the modulus of elasticity 100±30 GPa, which the authors of work [17] determined for nanostructured tungsten based on experimental data. A general trend is observed of decreasing of the modulus of elasticity with reduction in the grain size and respective increase in the intercrystalline boundaries. In this case, the correlation of the modulus of elasticity with the size and amount of the recrystallized phase was established experimentally, and a region of maximal E values was determined, which corresponds to the presence of 5–25 % of recrystallized grains of 1–8 μm size in the structure of W-cathodes.

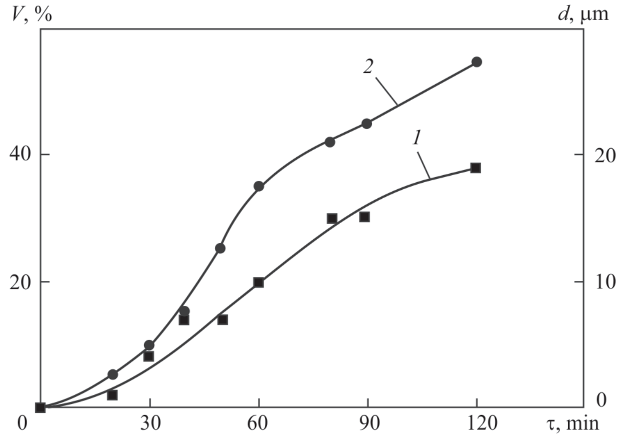

Figure 3. Influence of annealing time (τ) on recrystallized grain size d (*1*) and volume fraction V (*2*)

When solving the question of materials application, several parameters must be taken into account, as usual. During operation, the cathode is exposed not only to temperature loads, but also to mechanical loads, namely constant tension due to EBG design.

One of the causes for shortening of the service life of the supplied W-cathodes is their stretching during operation right up to sagging. Although creep resistance is the determining property of refractory materials, reduction of the creep rate is one of the tasks aimed at improvement of the cathode performance.

When conducting an additional experiment for comparison with the initial one, a cathode was select-

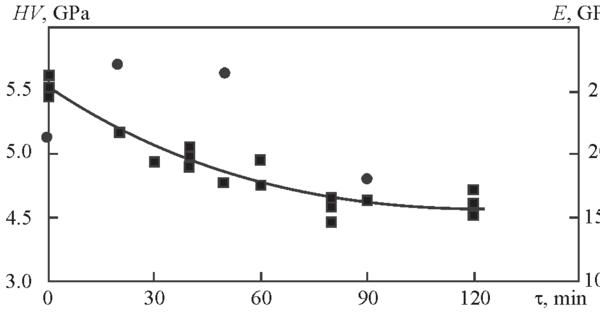

Figure 4. Influence of annealing time (τ) on mechanical properties of W-cathodes: line — microhardness; dots — modulus of elasticity

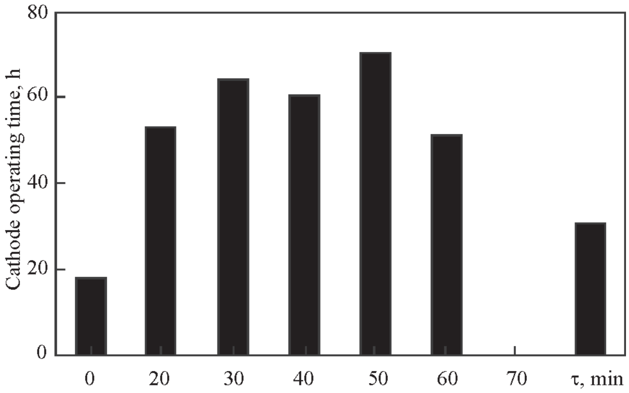

Figure 5. Service life of W-cathodes in the initial state and depending on vacuum annealing time

ed with maximal rigidity of the area with high E value, which has been subjected to HT by the following mode: $T = 1200$ °C, $\tau = 30$ min. Both the samples were tested under similar conditions: at a high temperature (operating temperature of directly heated cathode of 2200–2300 °C ($0.7T_m$) and under constant tensile stress of estimated value of 35.4 MPa, with 10 min time of operation in such a mode (it was noted that in case of a significant elongation of the cathode, it occurs in the first 10–20 min of operation). Measurement results showed that the magnitude of deformation $\Delta l/l$ of the initial and heat-treated cathodes was equal to 0.9 and 0.7 %, respectively. Thus, conducting cathode HT leads to lowering of creep rate.

Creep process in our case is associated with the impact of a whole number of different physical factors: tensile stresses; high temperature, cathode heating being characterized by a high rate and rather quickly entering the stationary operating mode; presence of an axial temperature gradient, resulting in a secondary recrystallization zone (*TSR* 2000–2100 °C) in the active central part of the cathode and possible development of compressive stresses, because of intensive metal expansion in this area is prevented by cold cathode ends. The question of creep mechanism is complicated, requiring additional studies and theoretical analysis, and it was not part of the objective of this work, but owing to great practical interest, investigations in this area will be carried on.

The physical creep mechanism probably is of a predominantly dislocation nature, based on the data of the map of creep deformation mechanisms of tungsten [18], and taking into account our values of the two main parameters, working temperature and stresses τ. It is known that the rate of this process is sensitive to structural characteristics, namely grain size and shape. It is obvious that presence of recrystallized grains of 4 μm size in the amount of 10 %, created additional boundaries in the direction normal to the load and this way slightly reduced the creep rate.

Experimental determination of the entire complex of processes taking place in the cathode assembly (including cathode material erosion as a result of ion bombardment) is quite complicated. Only indirect measurement of physical values determining the flow of processes inside the cathode is possible. Final response to the question of rationality of heat treatment application for W-cathodes is only given by checking their service properties under the actual conditions of EBG operation.

Results of evaluation of service life of as-delivered cathodes, as well as cathodes after HT in different modes, are shown in Figure 5. In as-delivered state the service life of the cathode varies from 10 to 18 h (8 cathodes have been tested), and after vacuum annealing ($T = 1200$ °C) during τ from 20 to 60 min it reaches the maximal 50–60 h. This coincides with the area of maximal E values (Figure 5) against the background of slight softening (Figure 4), due to internal stress lowering at the beginning stages of initial recrystallization process (Figure 3). Further increase of annealing time leads to lowering of operational characteristics, so it is not rational.

Thus, based on analysis of the results of the conducted complex studies, an optimal HT mode ($T = 1200$ °C, $\tau = 20$–50 min, protective environment is vacuum) was selected, in order to improve the service properties of W-cathodes. Such HT leads to the presence of a mixed two-phase structure of the recrystallized and unrecrystallized phases. Presence of a recrystallized phase of 1–8 mm size in the amount of 5–25 % ensures the level of mechanical properties, necessary for reliable operation of the cathodes: microhardness of 5.0±0.15 GPa, modulus of elasticity of 260–270 GPa.

CONCLUSIONS

1. It is found that to improve the quality of flat W-cathodes produced by pressing from tungsten wire, a mixed structure should be formed in them with the following quantitative ratio: up to 5–25 % of equiaxed recrystallized grains, with the rest of the cathode material volume preserving an unrecrystallized structure.

2. It is shown that such a condition of W-cathodes is reached after conducting the HT: vacuum annealing at 1200 °C for 20–50 min is recommended.

3. Service life of the cathodes heat-treated in such a mode reaches 50–60 h (3–5 times higher, compared to unheat-treated cathodes) and it corresponds to the level of endurance of foreign-made cathodes, the cost of which is several times higher.

REFERENCES

1. Zuev, I.V. (1998) *Processing of materials with concentrated energy flows*. Moscow, Izd-vo MEI [in Russian].

2. Movchan, B.A., Yakovchuk, K.Yu. (2004) Electron beam installations for evaporation and deposition of inorganic materials and coatings. *Sovrem. Elektrometall.*, **2**, 10–15 [in Russian].
3. Shapoval, A.A. (2011) Using highly processes in deformation trial tungsten ribbon. *Visnyk Kremenchuk National University,* Pt 1, 67(**2**), 65–67 [in Russian].
4. Yakovchuk, K.Yu., Barskov, V.O., Klimenko, I.G. et al. (2018) *Electron-beam projector with linear thermionic cathode*. Pat. 113607, Ukraine, Int. Cl. H01J37/06 H01J37/065 [in Ukrainian].
5. Movchan, B.O. (1994) *Linear thermionic cathode electron gun.* Pat. 21440, Ukraine, Int. Cl. H01J29/46 H01J29/48 [in Ukrainian].
6. Yaskolko, A.A. (2010) *Methods and results of studying materials of cathode of powerful X-ray tubes*. Syn. of Thesis for Ph. D. Dissertation. Moscow, A.A. Baykov Institute of Metallurgy and Materials Science [in Russian].
7. Taubin, M.L., Platonov, V.F., Yaskolko, A.A. (2009) Medical X-ray tube cathodes. *Med. Tekhnika*, 253(**1**), 44–47 [in Russian].
8. Shi Lei, L., Jun Yan, G., Yun Fei, Y. et al. (2020) A review on recent progress of thermionic cathode. *Tungsten,* **2**, 289–300. DOI: https://doi.org/10.1007/s42864-020-00059-1
9. Dragobetskyi V.V., Shapoval O.O., Shchepetov V.V. et al. (2017) *Controlled effects of plastic deformation of blanks for metallurgy and transport:* Monograph. Kharkiv, Madrid Printing House.
10. Ignatovich, S.R., Zakiev, I.M. (2011) Universal micro/nano-indentometer “MicronGamma”. *Zavodskaya Laboratoriya*, 77(**1**), 61–67 [in Russian].
11. Golovin, S.A, Krystal, M.A, Legner, M.N, Rabinovich, E.M. (1968) Recrystallization diagram of tungsten powder. *Physics and Chemistry of Metal Processing*, **5**, 168–172 [in Russian].
12. Savitsky, E.M., Povarova, K.B., Makarov, P.V. (1978) *Metallurgy of tungsten*. Moscow, Metallurgiya [in Russian].
13. Lassner, E., Schubert, W.D. (1999) *Tungsten: Properties, chemistry, technology of the element. alloys and chemical compounds*. Berlin, Springer-Verlag.
14. Humphreys, F.J., Hatherly, M. (2004) *Recrystallization and related annealing phenomena*. Elsevier.
15. Oliver, W.C., Pharr, G.M. (2004) Measurement of hardness and elastic modulus by instrumented indentation: Advances in understanding and refinements to methodology. *J. of Materials Research*., 19(**1**), 3–20.
16. Grigoriev, I.S., Meilikhov, E.Z. (1991) *Physical Quantities:* Handbook. Moscow, Energoatom.
17. Pugachevsky, M.A. (2010) Determination of the elastic modulus of tungsten nanowires. *Letters to the J. of Technical Physics*, 36(**14**), 7–12 [in Russian].
18. Frost, G.J., Ashby, M.F. (1989) *Maps of deformation mechanisms*. Moscow, Metallurgiya [in Russian].

ORCID

L.A. Krushinska: 0009-0000-6050-9130,
Ya.A. Stelmakh: 0000-0002-5238-2288

CONFLICT OF INTEREST

The Authors declare no conflict of interest

CORRESPONDING AUTHOR

L.A. Krushinska
E.O. Paton Electric Welding Institute of the NASU
11 Kazymyr Malevych Str., 03150, Kyiv, Ukraine.
E-mail: lkrushynska@gmail.com

SUGGESTED CITATION

L.A. Krushinska, Ya.A. Stelmakh, R.A. Tkach, O.O. Yukalchuk, A.A. Dudnik (2025) Influence of heat treatment on the structure, properties and durability of flat tungsten cathodes. *The Paton Welding J.*, **3**, 24–29.
DOI: https://doi.org/10.37434/tpwj2025.03.03

JOURNAL HOME PAGE

https://patonpublishinghouse.com/eng/journals/tpwj

Received: 15.01.2025
Received in revised form: 03.03.2025
Accepted: 09.04.2025

DOI: https://doi.org/10.37434/tpwj2025.03.04

STUDY OF THE TEMPERATURES OF PHASE TRANSFORMATION IN HEAT-RESISTANT TITANIUM ALLOY OF Ti–Al–Zr–Si–Mo–Nb–Sn ALLOYING SYSTEM

A.Yu. Severyn[1], **V.Yu. Bilous**[1], **L.M. Radchenko**[1], **V.A. Kostin**[1], **I.I. Alekseenko**[1], **L.T. Yeremeyeva**[1], **M.M. Kuzmenko**[2]

[1]E.O. Paton Electric Welding Institute of the NASU
11 Kazymyr Malevych Str., 03150, Kyiv, Ukraine
[2]Frantsevych Institute for Materials Science Problems of the NASU
3 Omelian Pritsak Str., 03142, Kyiv, Ukraine

ABSTRACT

Calculated continuous-cooling-transformation diagram (CCT-diagram) was derived for titanium alloy of Ti–Al–Zr–Si–Mo–Nb–Sn system to determine the phase transformation kinetics. The structures and microhardness of samples of heat-resistant titanium alloy of Ti–Al–Zr–Si–Mo–Nb–Sn alloying system, quenched from different temperatures, were studied. It was proved that application of computational methods of modeling the structure-phase transformations for heat-resistant titanium alloys allows obtaining results close to the experimental values.

KEYWORDS: heat-resistant titanium alloy, thermodynamic modeling, phase transformation, deformation processing, temperature, structure, phase, microhardness

INTRODUCTION

Thermodeformational treatment (TDT) is an effective method to improve the complex of physical and mechanical properties of semi-finished products and products from titanium alloys, together with alloying and heat treatment. It is known that titanium alloys deformed in the β-region, have a lamellar microstructure and demonstrate a higher resistance to high-temperature creep and impact toughness. This advantage, however, is achieved due to lower ductility and thermal stability, leading to β-brittleness and structural heredity. During (α+β) deformation the material is usually heated and processed at the temperature 30–50 °C lower than that of β-transition [1, 2]. That is why, during selection of the optimal thermomechanical deformation mode it is necessary to determine the average values of permissible degrees of one-time deformation of the cast billets at different temperatures for the main structural components of the material. The objective of determination of the optimal thermomechanical parameters of the deformation process consists in selection of the initial and final temperature and establishing the maximal permissible degree of deformation in the specified temperature range. It is extremely important, however, to know the temperature of polymorphous transformation of α↔β-titanium, which in multicomponent titanium alloys varies, depending on the composition and concentration of the alloying elements [3].

MATERIALS AND EXPERIMENTAL PROCEDURE

Electron beam melted (EBM) ingots 110 mm in diameter [4] were used in the experiments. Their composition is given in the Table 1.

Experimental cast alloy of Ti–Al–Zr–Si–Mo–Nb–Sn alloying system is a pseudo-α-alloy, the main structural components of which are a lamellar α-phase and a small amount of residual β-phase [4]. However, the final structure of titanium pseudo-α-alloys forms during hot deformation processing, and the structure type does not undergo any significant changes during subsequent heat treatment.

To obtain the values of physical characteristics of the new titanium alloy, it is possible to use computer models for calculation of thermal-physical and physical properties of multicomponent alloys at solidification and cooling. One of the main methods to produce

Table 1. Chemical composition of the alloy of Ti–Al–Zr–Si–Mo–Nb–Sn alloying system, wt.%

Al	Zr	Si	Mo	Nb	Sn	Ti
6.2–6.9	5.0–5.5	0.5–0.85	0.5–0.8	0.5–0.8	1.5–2.5	Base

such data is thermodynamic modeling by CALPHAD procedure, based on the theory of multicomponent alloys [55].

CALPHAD (Calculation of Phase Diagrams) is the procedure and approach in the field of materials science, used for modeling, prediction and understanding of the material phase diagrams. The main objective of CALPHAD consists in solving complex problems of phase equilibriums and phase transitions, which helps to solve the question of design and optimization of materials. The main CALPHAD aspects include [6]: thermodynamic models — CALPHAD uses thermodynamic models to describe the energy of various phases and phase transitions in materials. These models are based on experimental data and theoretical calculations; phase diagrams — CALPHAD allows plotting phase diagrams of materials, representing the phases, present with different combinations of temperature, pressure and composition; data bases — CALPHAD uses thermodynamic data bases, containing information on standard thermodynamic values of different phases and phase transitions; prediction of material properties — CALPHAD allows predicting such material properties as hardness, heat conductivity, magnetic properties, etc. based on phase diagrams and thermodynamic models; application in metallurgy — CALPHAD is widely used in metallurgy for development of new alloys and optimization of the alloying processes; application in materials science — CALPHAD is used for investigation and development of new materials with certain properties; systems with many components — CALPHAD allows developing phase diagrams for multicomponent systems, which is particularly important for complex materials; further investigations — CALPHAD is continuously developing and new methods and data bases are added constantly to improve the prediction of phase diagrams and properties of materials.

SG model was used with application of CALPHAD method for nonequilibrium processes, which yields good results for multicomponent alloys forming during solidification, and which allows deriving the dependence of many parameters on their composition and temperature.

Properties of individual phases in multicomponent systems, such as molar volume, heat conductivity, and density, are expressed by functions, similar to those used for modeling the thermodynamic functions in excess multicomponent alloys. Having determined the properties of individual phases, the property of the final alloy is calculated using well-established mixture models [7]. Such models were first developed for two-phase systems, which were extended to multicomponent structures. Large data bases of the respective parameters are now available for the majority of the main steels and alloys, aluminium and titanium alloys [8].

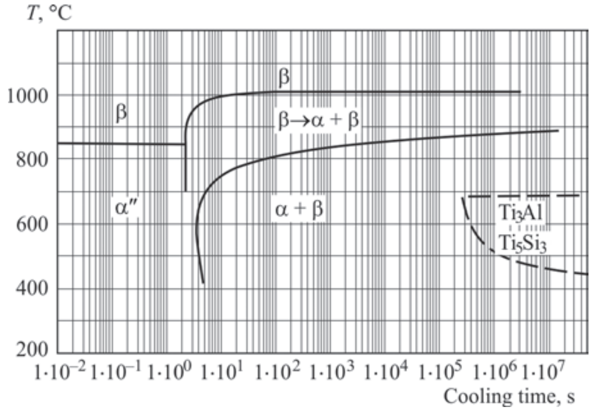

Figure 1. Calculated CCT-diagram of heat-resistant titanium alloy of Ti–Al–Zr–Si–Mo–Nb–Sn alloying system

During work performance, computer simulation of phase transformations of the heat-resistant titanium alloy of Ti–Al–Zr–Si–Mo–Nb–Sn alloying system was carried out [9]. To assess the change in the probable phase composition of the metal, computational CCT-diagram was plotted for this alloy (Figure 1).

The temperatures of the start of β→α transformation (~1015 °C) for cooling rates of 100–10 °C/s and end of β→α transformation (820–750 °C) for the same rates are marked in the diagram (Figure 1).

To confirm the calculated temperature of polymorphous transformation of a heat-resistant titanium alloy of Ti–Al–Zr–Si–Mo–Nb–Sn alloying system, a study of solid-phase transformations was performed with application of differential scanning calorimeter DSC 404 F3 Pegasus, operating in DTA mode (Figure 3). Samples were heated and cooled at the rate of 20 K/min up to the temperature of 1200 °C. To further refine the transformation temperatures, sample quenching was also performed with their further metallographic analysis. A series of samples were heated up to the temperatures from 800 to 1075 °C with 25 °C step,

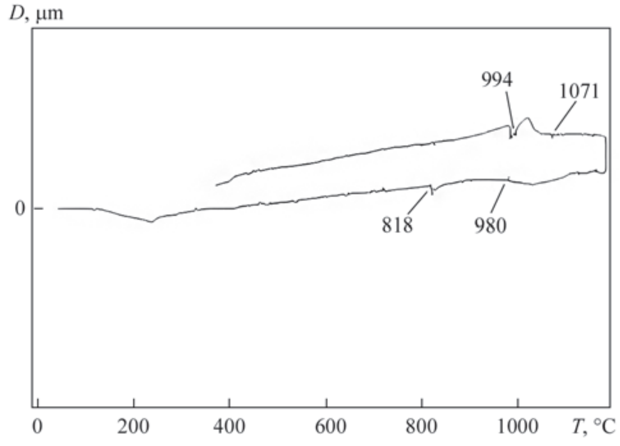

Figure 2. Dilatogram of an alloy of Ti–Al–Zr–Si–Mo–Nb–Sn alloying system

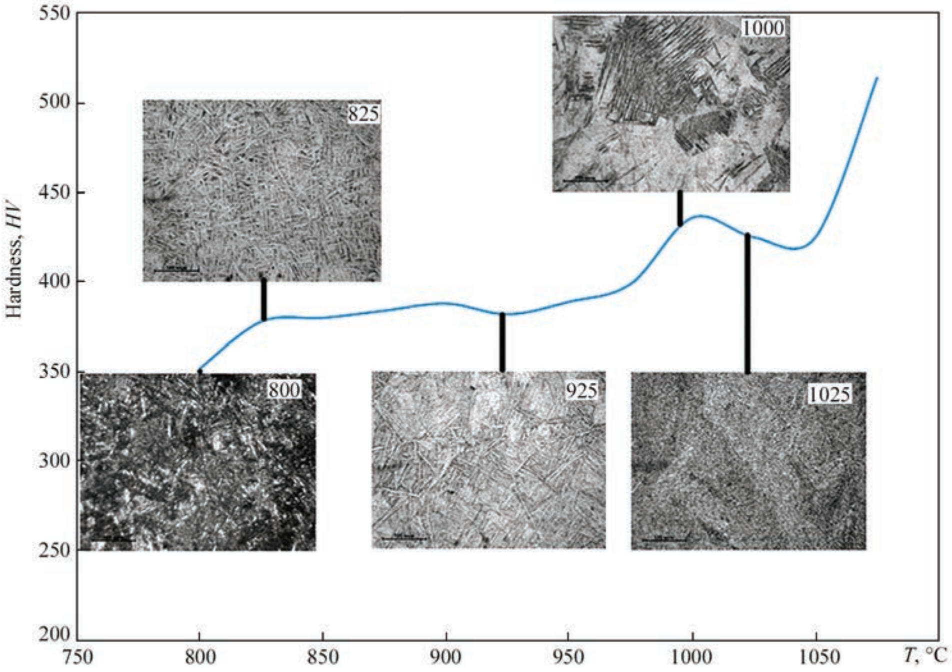

Figure 3. Microhardness of the samples and produced structures after quenching from different temperatures for an alloy of Ti–Al–Zr–Si–Mo–Nb–Sn alloying system

held in the furnace up to completion of the diffusion processes and quenched in water to record the phase composition. Change in the structure morphology and phase composition of the sample (Figure 2), allowed establishing the approximate temperature of polymorphous transformation of the material. Microhardness measurement was additionally performed on the quenched samples in LECO-M-400 instrument with 0.1 kg load. Change in material hardness also indirectly proves the change in its structure and phase composition (Figure 3).

The microstructure formed during quenching from the temperatures of the two-phase (α+β)-region consists of primary α-phase with lamellar morphology and α′-martensite. It is possible that presence of dispersion hardening due to dispersed α′-martensite results in a certain increase in material hardness in the temperature range of 825–1000 °C. Quenching from the single-phase region, leads to formation of α′-martensite and a small amount of the residual β-phase. Increase in hardness after the temperature of 1000 °C, is attributable to dissolution of the intermetallic α-phase and its further precipitation during quenching. A significant increase in material hardness in samples quenched from the temperature higher than 1050 °C, is explained by dissolution of silicides in the β-phase at these temperatures (Figure 4, *a*) [10], and during rapid cooling — by silicide precipitation in the entire sample volume (Figure 4, *b*).

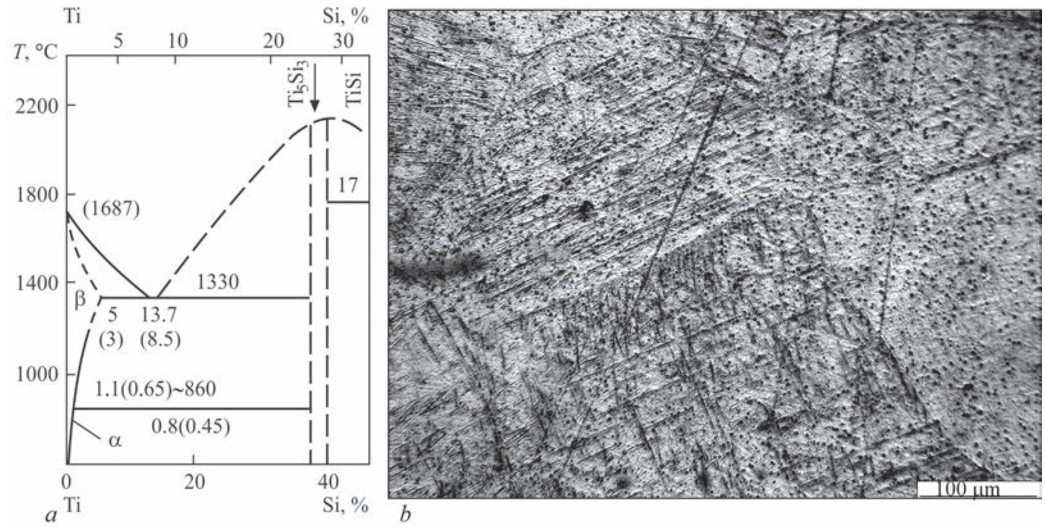

Figure 4. State diagram of Ti–Si system and structure, produced after quenching of an alloy of Ti–Al–Zr–Si–Mo–Nb–Sn alloying system from the temperature of 1050 °C

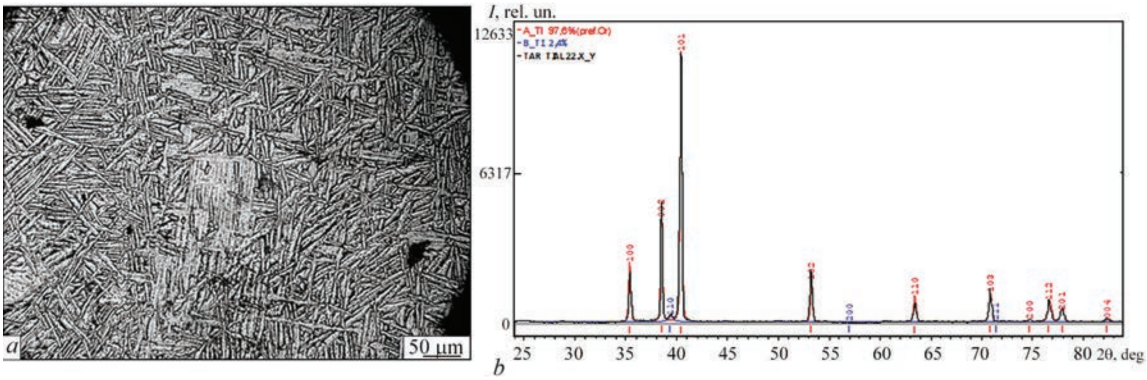

Figure 5. Microstructure (*a*) and roentgenogram (*b*) of initial metal of heat-resistant pseudo-β-titanium alloy of Ti–Al–Zr–Si–Mo–Nb–Sn alloying system

Comparison of computational diagram (Figure 1) and conducted experiments showed quite a slight discrepancy in the transformation temperatures. According to the diagram, in the range of the cooling rates of 10–100 °C/s, the calculated start of transformation begins at the temperatures of 780–850 °C, and ends at the temperature of 1015 °C, which is close to the experimental data. Dylatometric analysis demonstrates the temperature of transition from α- into (α+β)-region at about 818 °C, which is confirmed by the change in the structure in the quenched samples in the temperature range of 800–825 °C. The (α+β)→β transformation occurs in the temperature range of 994–1025 °C, which is also confirmed by the change in the structure morphology in the range of 1000–1025 °C. Thus, application of the computational methods of modeling the structural-phase transformation for heat-resistant titanium alloys yields results close enough to the experimental ones, which allows eliminating the operations of DTA and trial quenching and optimizing their structural-phase composition and improving their mechanical properties.

In keeping with the data obtained from the computational CCT-diagram of heat-resistant titanium alloy of Ti–Al–Zr–Si–Mo–Nb-Sn alloying system, and proved experimentally, hot deformation processing of EBM ingot with 50 % degree of deformation was performed from the temperature of β-phase region (~1050 °C) [11]. Deformed semi-finished products were produced in the form of rods 55 mm in diameter, the microstructure and phase composition of which are shown in Figure 5.

The microstructure of a sample from a deformed rod resembles the type of basket weave from α-plate packets (Figure 5, *a*). Silicide interlayers in the form of intermittent bands are located between the α-plates. Average grain size is equal to 50–70 µm. Investigations conducted by X-ray structural analysis confirmed that the pseudo-α-heat-resistant titanium alloy is a two-phase alloy and it consists of titanium β-phase (β-Ti) in the amount of 2.4 % (lattice parameters: $a = 2.9400$, $c = 4.670$), titanium α-phase (α-Ti) in the amount of 97.6 % (lattice parameters: $a = 3.2225$) (Figure 5, *b*).

CONCLUSIONS

1. A computational CCT-diagram was constructed for heat-resistant titanium alloy of Ti–Al–Zr–Si–Mo–Nb–Sn alloying system, which allowed determination of the temperature of α↔β-phase transformation in order to conduct further deformation processing.

2. Experimental quenching from different temperatures of a series of samples of heat-resistant titanium alloy of Ti–Al–Zr–Si–Mo–Nb–Sn alloying system was performed, which proves that application of computational methods of modeling the structure-phase transformations for heat-resistant titanium alloys yields results close to the experimental ones.

3. A dependence of metal microhardness on sample quenching temperature was established. Microhardness of metal of samples quenched from the (α+β)-region is higher than microhardness of samples quenched from the α-region, due to increase in the amount of the dispersed α′-phase, having a high strength and low ductility. Microhardness of metal of samples quenched from the β-region is ~10 % higher due to dissolution of silicides and their further precipitation at quenching.

4. Hot deformation processing of EBM ingot 110 mm in diameter from the temperature of β-phase region was performed, and deformed semi-finished products in the form of rods 55 mm in diameter were produced. Its microstructure and phase composition were studied. The deformed rod microstructure resembles the basket weave type from α-plate packets, and the silicide interlayers are located between the α-plates. Residual β-phase in the amount of 2.4 % is present in the structure.

REFERENCES

1. Hsueh-Chuan Hsu, Shih-Ching Wu, Shih-Kuang Hsu et al. (2014) Structure and mechanical properties of as-cast

Ti–Si alloys. *Intermetallics*, 47(**4**), 11–16. DOI: https://doi.org/10.1016/j.intermet. 2013.12.004

2. Shevchenko, O.M., Kulak, L.D., Kuzmenko, M.M. et al. (2023) The influence of the deformation and heat treatment on the structure and heat-resistance of Ti–Al–Zr–Si alloys. *Mater. Sci.*, 59(**1**), 40–48. DOI: https://doi.org/10.1007/s11003-023-00741-y
3. Solonina, O.R., Glazunov, S.P. (1976) *Heat-resistant titanium alloys.* Moscow, Metallurgiya [in Russian].
4. Akhonin, S.V., Berezos, V.O., Pikulin, O.M. et al. (2022) Producing high-temperature titanium alloys of Ti–Al–Zr–Si–Mo–Nb–Sn system by electron beam melting. *Suchasna Elektrometalurhiya*, **2**, 3–9 [in Ukrainian]. DOI: https://doi.org/10.37434/sem2022.02.01
5. Fan, Z., Tsakiropoulos, P., Miodownik, A.P. (1994) A generalized law of mixtures. *J. of Mater. Sci.*, **29**, 141–150. DOI: https:// doi.org/10.1007/BF00356585
6. Lukas, H.L., Fries, S.G., Sundman, B. (2007) *Computational thermodynamics: The CALPHAD method*. U.K., Cambridge University Press.
7. Khina, B., Goranskiy, G.G. (2017) Thermodynamics of multicomponent amorphous alloys: Theories and experiment comparison. *Adv. Materials and Technologies*, **1**, 036–043. DOI: https://doi.org/10.17277/amt.2017.01
8. Dinsdale, A.T. (1991) SGTE data for pure elements. *Calphad*, 15(**4**), 317–425. DOI: https://doi.org/10.1016/0364-5916(91)90030-N
9. Akhonin, S.V., Belous, V.Yu., Selin, R.V., Kostin, V.A. (2021) Influence of TIG welding thermal cycle on temperature distribution and phase transformation in low-cost titanium alloy. In: *Proc. of IOP Conf. Series: Earth and Environmental Sci.*, **688**, 1–9. DOI: http://dx.doi.org/10.1088/1755-1315/688/1/012012
10. Lyakisheva, N.P. (2000) *State diagram of binary metallic systems:* Refer. Book. Vol. 2, Book 2. Moscow, Mashinostroenie [in Russian].
11. Akhonin, S.V., Severyn, A.Yu., Berezos, V.O. et al. (2024) Influence of deformation processing modes on the structure and mechanical properties of a high-temperature titanium alloy of the Ti–Al–Zr–Si–Mo–Nb–Sn system. *Metallophysics and Advanced Technologies*, 46(**7**), 705–715. DOI: https://doi.org/10.15407/mfint.46.07.0705

ORCID

A.Yu. Severyn: 0000-0003-4768-2363,
V.Yu. Bilous,: 0000-0002-0082-8030,
L.M. Radchenko: 0000-0002-4235-2413,
V.A. Kostin: 0000-0002-2677-4667,
I.I. Alekseenko: 0000-0002-2595-1684,
M.M. Kuzmenko0000-0001-8108-7088

CONFLICT OF INTEREST

The Authors declare no conflict of interest

CORRESPONDING AUTHOR

A.Yu. Severyn
E.O. Paton Electric Welding Institute of the NASU
11 Kazymyr Malevych Str., 03150, Kyiv, Ukraine.
E-mail: tim.severin72@gmail.com

SUGGESTED CITATION

A.Yu. Severyn, V.Yu. Bilous, L.M. Radchenko, V.A. Kostin, I.I. Alekseenko, L.T. Yeremeyeva, M.M. Kuzmenko (2025) Study of the temperatures of phase transformation in heat-resistant titanium alloy of Ti–Al–Zr–Si–Mo–Nb–Sn alloying system. *The Paton Welding J.*, **3**, 30–34.
DOI: https://doi.org/10.37434/tpwj2025.03.04

JOURNAL HOME PAGE

https://patonpublishinghouse.com/eng/journals/tpwj

Received: 20.01.2025
Received in revised form: 21.02.2025
Accepted: 09.04.2025

REMOTE MONITORING OF LARGE-SIZED STRUCTURES BASED ON PHOTOGRAMMETRY METHOD AND ARTIFICIAL INTELLIGENCE

Paton Welding Institute offer a new method for defect detection in large structures using UAVs, photogrammetry, and artificial intelligence (AI). This approach involves UAV surveys that generate a comprehensive database of high-resolution images. These images are used to create accurate 3D models using 3DF Zephyr software, and artificial intelligence is used to effectively detect defects.

Detection results: AI-identified defects and bolts

- ◈ Verticality Assessment
- ◈ Defect Detection using AI
- ◈ Defect Localization
- ◈ Measurement of Defect Sizes and Structural Elements

DOI: https://doi.org/10.37434/tpwj2025.03.05

STUDY OF THE EFFECT OF ELECTRICAL DISCHARGE CUTTING ON FORMATION OF A DAMAGED LAYER DURING PROCESSING OF TUNGSTEN SINGLE CRYSTALS

Yu.O. Nikitenko, V.O. Shapovalov, V.V. Yakusha, O.M. Gnizdylo, D.M. Zhirov

E.O. Paton Electric Welding Institute of the NASU
11 Kazymyr Malevych Str., 03150, Kyiv, Ukraine

ABSTRACT

The new type of electrical discharge machining without immersion of the processed workpiece is characterized by higher cost-effectiveness, simplified maintenance, and safety. In addition, a molybdenum wire with multiple reversible feed is used as a cutting tool, instead of a consumable brass wire. This study presents the results of experiments on processing tungsten single crystals by varying the technological modes of electrical discharge cutting. The dependences of the effect of the duration of electrical discharge pulses and the pause between them on surface morphology, depth of interplane crack formation, and cutting speed were determined. Molybdenum wire with a diameter of 0.18 mm and a tungsten single crystal with a thickness of 15 mm were used as tools and working material in the experiments.

KEYWORDS: tungsten single crystal, electrical discharge cutting, damaged layer, interplane cracks

INTRODUCTION

Unique properties of single crystals which are due to structural perfection and anisotropy of the crystal lattice have an essential role in ensuring the required parameters and durability of products made from them. Therefore, the question of processing single-crystal products is relevant, both for semiconductor, and for metal materials, as the unremoved damaged surface layer completely levels out the unique properties inherent in the single-crystal structure [1]. High thermomechanical loads, which are in place during machining, result in formation of a defective layer, with a high concentration of dislocations. The surface layer with a damaged structure is one of the most common types of defects in manufacturing products from single crystals, as production of solid-state elements is related to a certain set of necessary operations of surface processing, such as cutting, grinding, polishing, and subsequent finer finishing to ensure the specified product characteristics. This question is particularly relevant for general investigation of the single crystal properties in the sense of studying the damaged layer depth, its influence on subsequent processing stages to avoid its development and investigation of the internal (actual, undistorted) crystalline structure [2].

Determination of the thickness of damaged surface layer of single crystals, i.e. after cutting, grinding and physical-chemical polishing, allows optimizing the modes of crystal machining.

As tungsten single crystal is a rather hard material, its machining by a cutting tool is quite problematic, both for the tool and for the crystal proper. Characteristic parameters of the damaged surface layer largely determine the degree of structural perfection of the single crystal proper. The value of this quantity may depend not only on the single crystal processing method, but also on the directions of force impact on the processed crystal, having the specified crystallographic orientation.

That is why, electrical discharge (electrical spark) machining is often used for primary processing of refractory metal single crystals (to eliminate hard machining). Electrical discharge machining is a controlled destruction of current-conducting material under the impact of electrical discharges between the electrode and the part. Discharges occur in the pulse mode so that the interelectrode space has enough time to restore its electrical resistance.

After electrical discharge machining, particularly of tungsten single crystals, a polycrystalline layer with an axial texture is formed on the metal surface. The fine structure of this layer, as well as its formation mechanism, is closely related to the anisotropy of metal properties in a single-crystal state.

The most widely accepted method of Wire Electrical Discharge Machining (WEDM) is the method of cutting samples, which are completely immersed into the working fluid (kerosene or water). Brass wire is used as the cutting tool, and many studies have been conducted in this field [3–5]. Development of the technologies of electrical discharge cutting allowed creation of new variants of this process. Instead of a consumable brass wire, 0.18 mm molybdenum wire with reversible feed is used, that is the wire of the specified length takes part in cutting many times, owing to winding on and unwinding from the drum. Cutting proceeds without immersion, but with feeding of the water-based

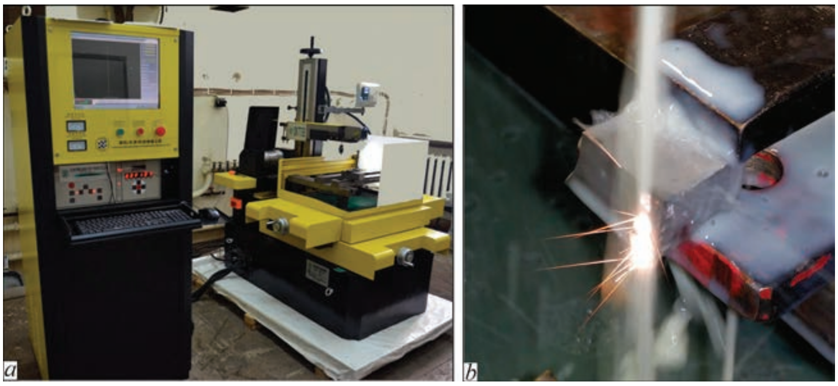

Figure 1. Appearance of the electrical discharge cutting machine DK7732 (*a*) and photo of the process of cutting a sample of tungsten single crystal (*b*)

Table 1. Characteristics for calculation of cutting parameters

Characteristic	*K*	0	1	2	3	4	5	6	7
Pulse duration	μs	1	2	4	6	9	12	16	20
Characteristic	*K*	8	9	A	B	C	D	E	F
Pulse duration value	μs	24	28	32	40	48	56	64	72

lubricating and cooling agent (LCA) from the sample top and bottom. The wire, making a reversible motion, captures a certain amount of LCA with its surface and transports it to the location of spark gap.

That is why, the performed study of the influence of technological parameters of WEDM-process of electrical discharge cutting on the properties of the damaged layer of tungsten single crystals is an important scientific-practical task, having current practical importance for their wider application in engineering.

TECHNOLOGICAL EQUIPMENT, EXPERIMENTAL PROCEDURE AND MATERIALS

Wire-cut electrical discharge machine DK7732 (TOSUN) with CNC is designed for processing any current-conducting materials, including metal-ceramic alloys, non-ferrous metals and other difficult-to-process materials, which allows producing complex shaped external and internal surfaces from them (Figure 1, *a*). DK77 series machines are jet type machine tools, where processing is conducted not in a bath with fluid, but on the working table, where LCA is supplied directly into the processing zone from the bottom and the top (Figure 1, *b*).

The main technical characteristics of electrical discharge equipment are given below.

Specification of DK7732 machine

Cooling liquid type	Water with addition of JR3 emulsion (A, B, C, D, H, G)
Electrode type	Reusable molybdenum wire
Overall dimensions of the working table, mm	Not less than 620×450
Working table travel (*X*, *Y*)	Not less than 450×350
Maximal weight of the part placed on the working table, kg	Up to 600
Maximal processed height of the part, mm	Up to 300
Usable wire diameter, mm	0.04–0.22
Part processing accuracy, mm	Not more than 0.010
Accuracy of repeatable positioning of *X*, *Y* axes, μm	Not more than ±1
Installed power, kW	Not more than 3

In keeping with the user manual, the machine has four main groups of changeable processing parameters, which influence the cutting process characteristics: pulse duration (values of 0, 1, 2, 3, 4, 5, 6, 7, 8, 9, A, B, C, D , E, F); pulse interval (values of 0, 1, 2, 3, 4, 5, 6, 7, 8, 9, A, B, C, D, E, F); tracking the critical interelectrode spacing (values of 0, 1, 2, 3, 4, 5, 6, 7, 8, 9, A, B, C, D, E, F); pulse amplifier level (values of 0, 1, 2, 3, 4, 5, 6, 7, 8, 9, A)

To conduct a pure experiment, only such current characteristics as pulse duration and interval between them were studied. Tracking and amplification parameters were unchanged in all the experiments and their values were 1 and 6, respectively.

Table 1 gives the values of pulse duration (in microseconds), depending on the *K* setting parameter. Value of the interval between the pulses is calculated as $4 + 0.25K$ (where K is the pulse duration, in keeping with the value from Table 1).

EXPERIMENTAL RESULTS AND THEIR ANALYSIS

The problem of single crystal machining is highly relevant both in product manufacturing and in seed crystal production. Formation of deep gaps between the planes may lead to formation of parasitic grains of different orientation.

For instance, in order to produce a crystal in the form of a body of revolution, machining is used to cut off a seed crystal from a large flat crystal, which was grown with lateral face orientation in the plane (100) (Figure 2, *a*). The seed crystal is given a circular shape and

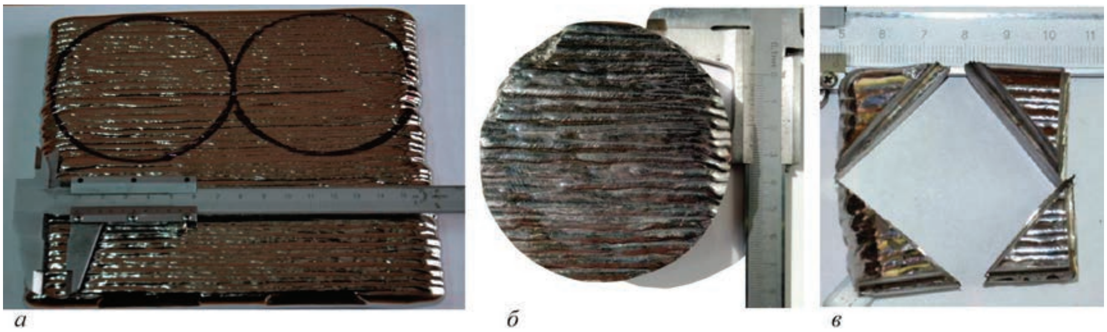

Figure 2. Stages of producing seed single crystal for growing a tungsten ingot in the form of the body of revolution: large flat single crystal of 170×160×25 mm size (*a*), round seed crystal 85 mm in diameter (*b*) and corner segments remaining after treatment (*c*)

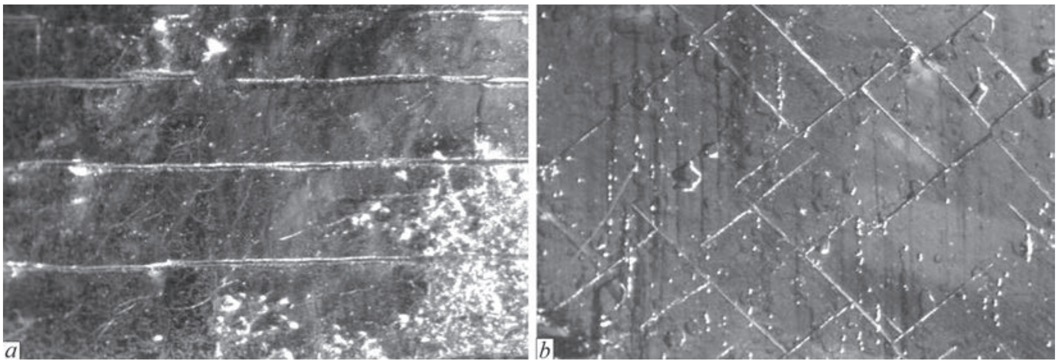

Figure 3. Crack network on the side (*a*) and bottom surface (*b*) of the seed crystal after abrasive treatment

all unnecessary elements are separated (Figure 2, *b*, *c*). Harsh processing conditions may result in formation of a network of cracks which corresponds to the crystal orientation of the ingot. Figure 3 gives an example of crack formation on the side and bottom surfaces. Presence of parallel and rectangular cracks corresponds to interplanar formations for orientations (100, 010, 001).

With application of electrical discharge cutting, the process of cutting out the seed crystal becomes much easier, and the need for additional treatment of the side surface is eliminated. The seed crystal has the set ideal cylindrical shape 85 mm in diameter (Figure 4). Even though the side surface has a damaged defective layer, it is much smaller, and during the technological process of plasma-induction growing the surface melting at a minimal speed of sample rotation ensures restoration of the single-crystal structure.

During examination, the cut surface is rough with a not more than 0.2–0.3 mm defective layer, which is related to the features of electrical discharge cutting (Figure 5). During cutting electrical discharges are sent in-depth of the base metal, forming a defective layer. Defects are manifested as chipping of material from the surface in the form of geometric shapes pointing in the same direction. During chemical etching, a set of parallel cracks is revealed (Figure 6). The same direction of the rectangle defect edges is indicative of preservation of the general orientation of the single-crystal structure. Stresses accumulated during treatment may lead not only to formation of a crack network, but also to fragment spallation from the surface. A solution of hydrofluoric (HF) and nitric (HNO_3) acids in a ratio of 1:1 was used as the chem-

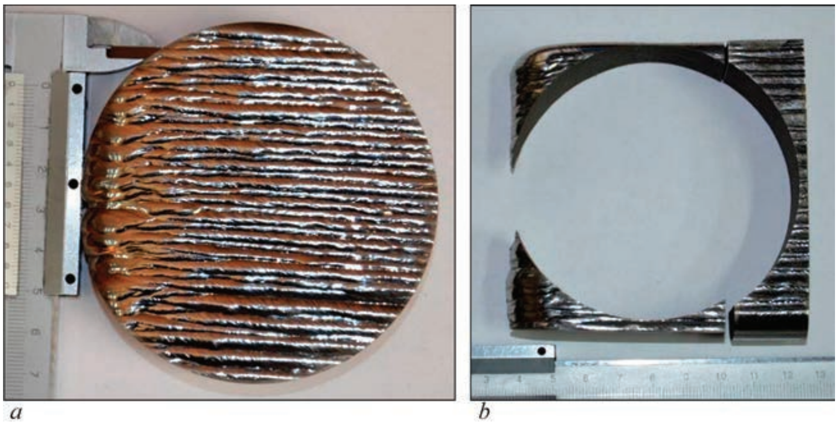

Figure 4. General view of the seed crystal (*a*) and remains after electrical discharge cutting (*b*)

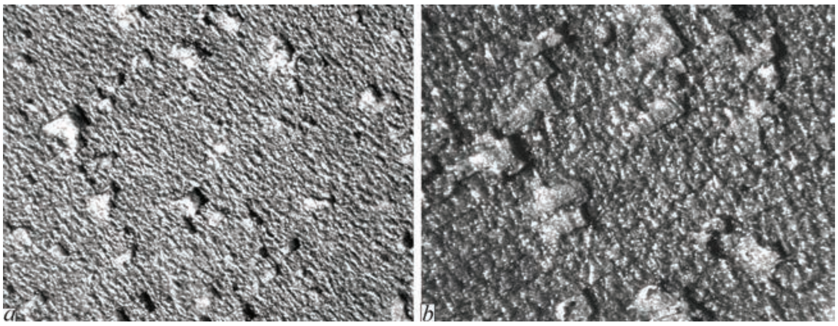

Figure 5. Appearance of the vertical plane of sample cut after electrical discharge cutting at the following magnification: *a* — ×50; *b* — ×88

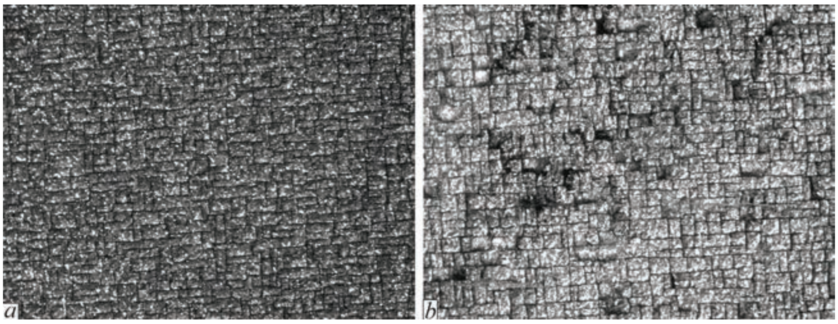

Figure 6. Formation of a crack network on the sample surface after electrical discharge cutting, which is manifested after etching by chemical reagents: *a* — horizontal; *b* — vertical plane

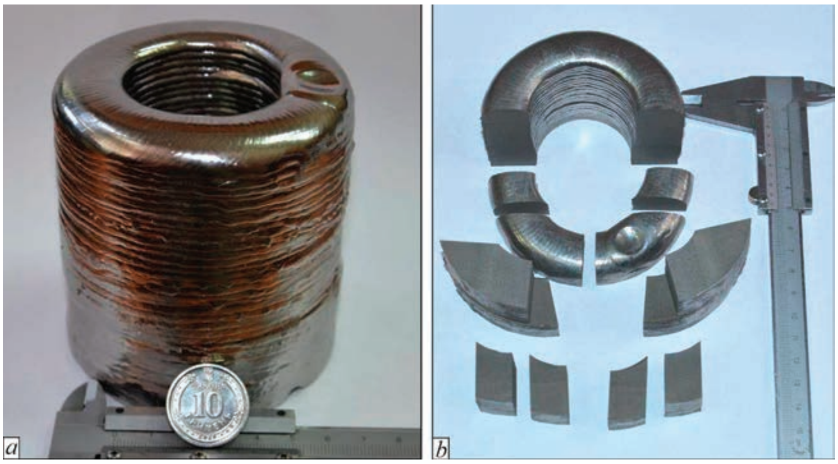

Figure 7. Tungsten single crystal grown in the form of a hollow cylindrical body 85 and 68 mm in diameter (*a*), and its separated upper part cut up into small samples (*b*)

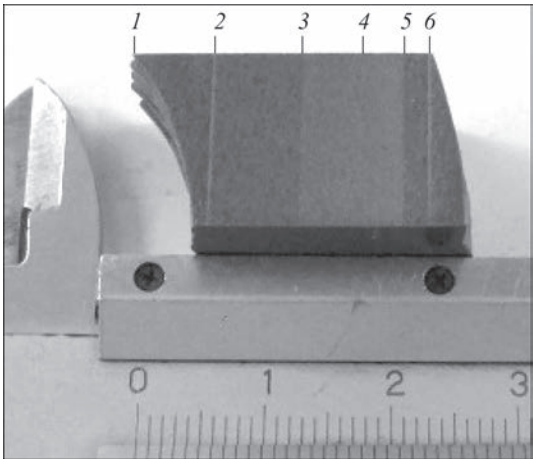

Figure 8. Appearance of an experimental tungsten sample with marked zones of different cutting modes

ical reagent for etching and identification of structure defects, etching time being 5 min.

A rather stringent treatment mode was used (AA18) to prepare a seed crystal, which ensured maximal cutting productivity.

However, further research, particularly during preparation of samples for metallographic examination, raises the question about the actual depth of the damaged layer, which should be removed in order to conduct further studies of the actual undamaged structure.

Samples, separated from the crystal in the form of a cylindrical hollow body 85 mm in diameter, were selected as material for investigations (Figure 7) [7]. Experiments were conducted with cutting of one of the samples in different modes in the horizontal plane of the ingot (Figure 8), cut height being 15 mm. Fig-

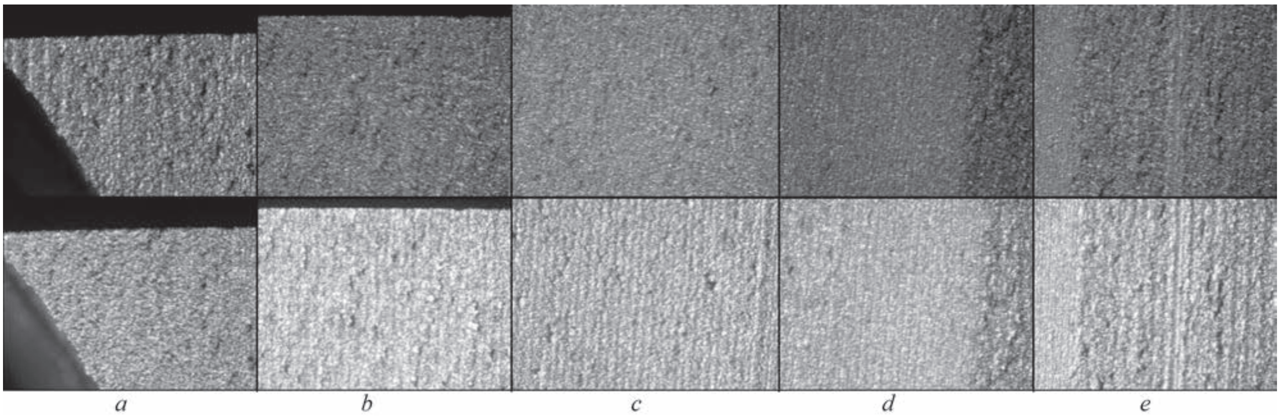

Figure 9. Enlarged view of the zones at different lighting angles (×200): *a* — 1; *b* — 2; *c* — 3; *d* — 4; *e* — 5; *f* — 6, designations, corresponding to Figure 8

Table 2. Cutting modes relative to Figure 9

Mode	1	2	3	4	5	6
Designation	9B16	7D16	5F16	3416	9616	9816
Pulse, μm	28	20	12	6	28	28
Pause, μm	14	18	22	6,25	8	10
Cutting speed, μm/s	< 15	< 13	< 11	< 9	< 16	< 14

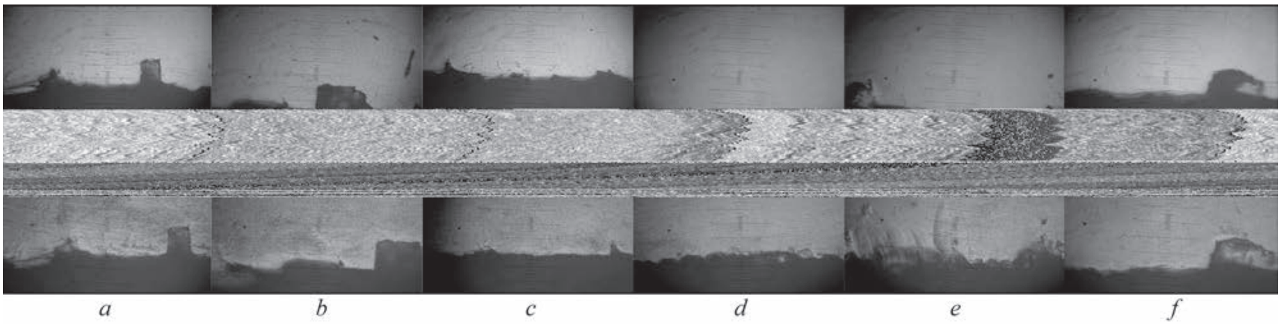

Figure 10. Depth of penetration of gaps and damage from electrical discharge cutting (×200); upper row — polishing, lower row – after etching; *a* — 1; *b* — 2; *c* — 3; *d* — 4; *e* — 5; *f* — 6; distance between two large divisions of the scale is equal to 50 μm

ure 9 gives enlarged photos of the obtained surface relief, formed in different cutting modes (Table 2). For a more voluminous and visual perception of the relief, the photos were taken at different lighting angles.

To determine the damaged layer depth, surface grinding was performed in the plane normal to the cutting area. The depth of the formed cracks propagating deep into the metal was studied directly after grinding and after chemical etching (Figure 10).

Results of the conducted studies are given in Table 3. Having analyzed the influence of pulse and pause duration, we can draw the following conclusions: during treatment in the modes with unchanged pulse time (modes 1, 5, 6) the parameter of the dura-

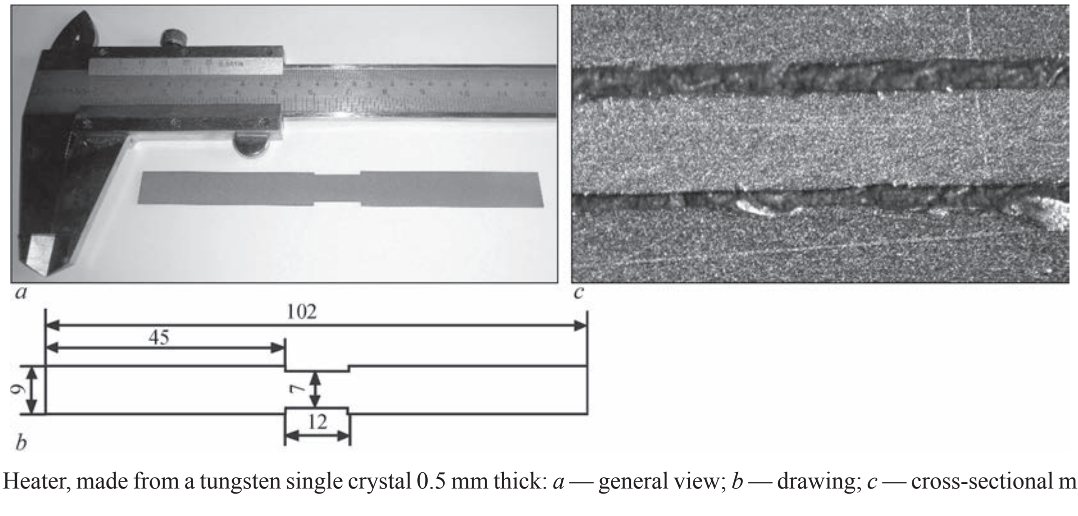

Figure 11. Heater, made from a tungsten single crystal 0.5 mm thick: *a* — general view; *b* — drawing; *c* — cross-sectional microsection

Table 3. Depth of crack propagation into the tungsten single crystal body, depending on the cutting mode

Mode	4	3	1, 2, 5, 6
Crack depth	< 50 μm	≈ 100 μm	< 200 μm

tion of pauses between the pulses practically did not influence the defective layer characteristics; reduction of pulse duration (modes 1, 2, 3, 4) lowers the influence of the treatment factor on defective layer formation, which is manifested in reduction of its depth. In mode 4 the depth did not exceed 50 μm.

Based on the conducted studies, the cutting modes were selected for manufacturing critical parts from tungsten single crystals. A defect-free thin-walled heating element 0.5 mm thick was produced (Figure 11).

CONCLUSIONS

Technological modes of tungsten single crystal treatment by electrical discharge cutting have been studied. The influence of the modes on the damaged layer depth and crack propagation in-depth of the single-crystal structure was established. It is shown that in the hard modes, ensuring the maximum cutting speed, the depth of the damaged layer may reach 200 μm. It was determined that by reducing the pulse duration it is possible to achieve formation of the treated surface almost without the damaged layer, but it will result in lower cutting speeds.

The work was carried out with the assistance of the Ministry of Education and Science of Ukraine, Order No. 134 of 02.0.22021 "On financing in 2021 scientific and technical work within the framework of the implementation of the state order for scientific and technical (experimental) developments and scientific and technical products", in keeping with Agreement No. DZ/103-2021 of 09.03.021: "Development of innovative 3D technology of growing single-crystal tungsten crucibles".

REFERENCES

1. Shpak, A.P., Molodkin, V.B., Nizkova, G.I. et al. (2004). Influence of the broken surface layer on dynamic scattering in crystals with defects. *Usp. Fiz. Met.*, **5**, 285–312. DOI: https://doi.org/10.15407/ufm.05.03.285
2. Tosun, N., Cogun, C., Tosun, G. (2004) A study on kerf and material removal rate in wire electrical discharge machining based on Taguchi method. *J. Materials Proc. Technology,* **152**, 316–322. Doi: DOI: https://doi.org/10.1016/j.jmatprotec.2004.04.373
3. Kneubühler, F., Wiessner, M., Wegener, K. (2020) Analysis of WEDM process with respect to wire wear and wire consumption. *Procedia CIRP,* **95**, 313–318. DOI: https://doi.org/10.1016/j.procir.2020.03.151
4. Tosun, N. (2003) The effect of the cutting parameters on performance of WEDM. *KSME Inter. J.*, 17(**6**), 816–824. DOI: https://doi.org/10.1007/BF02983395
5. Mouralova, K., Prokes, T., Benes, L., Bednar, J. (2019) The infuence of WEDM parameters setup on the occurrence of defects when machining Hardox 400 steel. *Materials*, **12**, 3758. DOI: https://doi.org/10.3390/ma12223758.
6. Nikitenko, Yu.O., Shapovalov, V.O., Yakusha, V.V. et al. (2023) 3D technology of growing single-crystal ingots in the form of hollow tungsten cylinders. *Suchasna Elektrometal.*, **2**, 34–40 [in Ukrainian]. DOI: https://doi.org/10.37434/sem2023.02.05
7. Nikitenko, Y., Shapovalov, V., Yakusha, V. et al. (2024) Features of the structural formation of tungsten single crystals in the shape of hollow rotational bodies. *Mat. Sci. Forum*, 1113. DOI: https://doi.org/10.4028/p-SDyx6A 2024

ORCID

Yu.O. Nikitenko: 0000-0002-3603-2333,
V.O. Shapovalov: 0000-0003-1339-3089,
V.V. Yakusha: 0000-0001-5962-9194,
O.M. Gnizdylo: 0000-0001-7537-6481,
D.M. Zhirov: 0000-0002-9435-8075

CONFLICT OF INTEREST

The Authors declare no conflict of interest

CORRESPONDING AUTHOR

Yu.O. Nikitenko
E.O. Paton Electric Welding Institute of the NASU
11 Kazymyr Malevych Str., 03150, Kyiv, Ukraine.
E-mail: nikyu80@gmail.com

SUGGESTED CITATION

Yu.O. Nikitenko, V.O. Shapovalov, V.V. Yakusha, O.M. Gnizdylo, D.M. Zhirov (2025) Study of the effect of electrical discharge cutting on formation of a damaged layer during processing of tungsten single crystals. *The Paton Welding J.*, **3**, 35–40.
DOI: https://doi.org/10.37434/tpwj2025.03.05

JOURNAL HOME PAGE

https://patonpublishinghouse.com/eng/journals/tpwj

Received: 05.06.2024
Received in revised form: 14.02.2025
Accepted: 27.04.2025

DOI: https://doi.org/10.37434/tpwj2025.03.06

STUDY OF INTERGRANULAR CORROSION CRACKING IN WELDED JOINTS OF CHORNOBYL NPP PIPELINES. MATERIALS SCIENCE ASPECT

V.M. Torop[1], **V.B. Hutsaylyuk**[2], **M.D. Rabkina**[1], **E.O. Davydov**[1]

[1]E.O. Paton Electric Welding Institute of the NASU
11 Kazymyr Malevych Str., 03150, Kyiv, Ukraine
[2]Military University of Technology
gen. Sylwestra Kaliskiego Str. 2, 00-908, Warsaw, Poland

ABSTRACT

Stress corrosion cracking, similar to intergranular corrosion in austenitic steel welds, primarily affects grain boundaries in the heat-affected zone when exposed to a corrosive environment, leading to sensitization, i.e. reduction in structural integrity, which causes cracking and grain loss. The object of studies were specimens cut out of rings from the pipelines of Power Unit 3 of the Chernobyl NPP in the areas of damaged welded joints. Based on radiographic and ultrasonic testing of pipeline welds, as well as determination of the content of alloying elements in the tested specimens, mechanical properties, metallographic, fractographic and micro-X-ray spectral studies, including investigation of fracture surfaces of specimens that were cyclically loaded taking into account fatigue grooves, and with regard to solution of the problem of corrosion cracking of austenitic steels in boiling water reactors, a set of measures was developed, including long-term measures: replacement of steels with others, that are not prone to corrosion cracking; short-term measures: deposition of external weld coating, repair of defective areas, relieving residual stresses; temporary measures: justification of the admissibility of the defective weld for operation.

KEYWORDS: radiographic and ultrasonic testing of welded joints, intergranular corrosion, stress corrosion cracking, corrosion-resistant steel, pipelines, alloying elements, chromium carbides, fatigue grooves

INTRODUCTION

Stress corrosion cracking in welded joints (WJ), similar to intergranular corrosion (IGC), can occur almost without visual evidence of corrosion damage [1]. Metallographic and fractographic studies of fractures performed on damaged circumferential welds cut out from the pipelines of Unit 3 (pipelines of the 1st circuit with an outer diameter of 325 mm and a wall thickness of 16 mm) revealed an intergranular (at crack propagation in the heat-affected zone (HAZ)) and intragranular (at crack propagation along the weld metal) fracture pattern. The crack surfaces are oxidised. Significant corrosion damage with typical crack branching was observed in both cases [2, 3]. IGC is known to be a type of local corrosion of steels and alloys when a potential difference between the grain boundaries and the body of the grains occurs during the contact with the corrosive environment. This type of corrosion usually takes place when a phase precipitation from the solid solution occurs in the alloy. In most cases, the precipitation occurs more rapidly at the grain boundaries, the so-called sensitization, which results in the depletion of the material near the grain boundaries by the alloying element. Unlike other forms of corrosion (pitting, crevice and fretting corrosion), signs of intergranular corrosion in stainless steel are not always visible on the metal surface. Intergranular corrosion occurs at the microscopic level, affecting the metal structure itself, and requires certain conditions that can be avoided in some cases. The precipitation of chromium carbides at grain boundaries in austenitic stainless steels typically occurs at heating from 540 to 845 °C, which leads to a depletion of chromium at the grain boundaries and, consequently, increased corrosion sensitivity. The most frequently sensitization is caused by welding. In addition, the mentioned temperatures are most common during heat treatment or operation in a high-temperature environment.

Thus, intergranular corrosion in a stainless steel weld mainly affects the grain boundaries in the HAZ, which leads to a decrease in structural integrity, causing cracking and grain loss. At the same time, in welded structures made of ferritic steels, fracture occurs both in the area immediately adjacent to the weld place and in the weld itself. Ignoring the risks of intergranular corrosion can lead to catastrophic failure or partial failure of critical welded structures and various components of stainless steel structures, including NPP equipment, pipelines used in oil and gas transportation, etc.

INFLUENCE OF ALLOYING ELEMENTS ON THE IGC MECHANISM IN STAINLESS STEELS

Three classes of stainless steels are traditionally used: ferritic, martensitic and austenitic, and rarely two-

Table 1. Influence of alloying elements in steel based on anodic polarization curves of pure metals [3]

Value of potential E, V	Characteristic of the environment	Rate of metal solution in the series
–0.5	Strongly reducing	Ni < Mo< W < Fe < Cr < Mn
–0.05	Non-oxidizing	Mo < Cr < W < Ni < Fe < Mn
+0.2	Slightly oxidizing	Mo < Cr < W < Ni < Fe < Mn
+0.6	Medium oxidizing	Cr < Ni < Fe < W < Mo < Mn
+1.1	Oxidizing	Cr < Ni < Fe < W < Mo < Mn
+1.3	Highly oxidizing	Fe < Ni < W < Cr < Mo

phase. The largest group of all stainless steels includes austenitic corrosion-resistant steels, which account for 60–70 % of global consumption [4]. They usually contain 16–25 % Cr, 6–14 % Ni, sometimes 2–6 % Mo and a small amount of other elements. The most common example is 08Kh18N10T steel. It should be noted that 08Kh18N10T steel used for pipe manufacturing is an analogue of AISI321 stainless austenitic steel stabilized with titanium.

Chromium is the main alloying element in corrosion-resistant steels that ensures the passivation ability of steel over a wide range of potentials. The instability of chromium is manifested only in the potential range of –0.58 V in highly reducing environments and 1.3 V in highly oxidizing environments (Table 1).

The effect of chromium on IGC is closely related to carbide formation. At a constant quenching temperature, the minimum time τ_{min}, required for carbide formation depends on the diffusion rate of carbon and chromium. In the low temperature region, the appearance of IGC tendency is controlled by chromium diffusion, and at higher temperatures — by carbon diffusion. Since the ability of carbon to form carbides is determined by its thermodynamic activity, which is significantly influenced by the chemical composition of steel, the admissible carbon content depends on the content of such alloying elements in steel as nickel, molybdenum, etc.

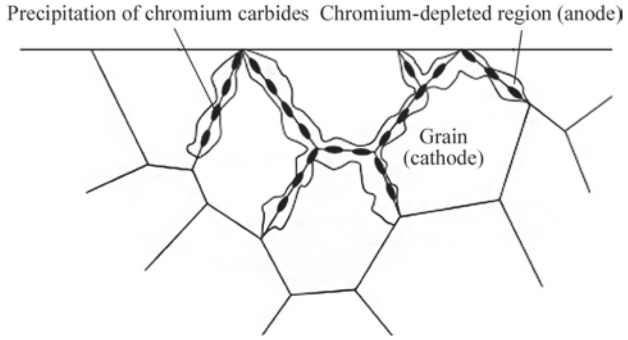

Figure 1. Schematic representation of carbide precipitation at grain boundaries in austenite [4]

Nickel, silicon and cobalt increase the activity of carbon, i.e. facilitate the formation of carbides; molybdenum, tungsten, vanadium, niobium and manganese decrease the activity of carbon, i.e. inhibit the formation of carbides. Nickel is introduced into corrosion-resistant steels to ensure the stability of the austenitic structure and to improve the corrosion resistance of steel mainly in reducing environments, although it has satisfactory corrosion resistance in a wide range of potentials. Molybdenum enhances the self-passivation ability of chromium-nickel steels and significantly increases their resistance in non-oxidizing and slightly oxidizing environments. In oxidizing and strongly oxidizing environments, the corrosion rate of molybdenum and molybdenum-rich phases is high (Table 1).

One of the most common ways to prevent IGC is to alloy corrosion-resistant steels with carbide-forming elements. The most stable carbides form titanium, niobium and tantalum, but stabilization with titanium and niobium is more commonly used [5]. According to the stoichiometric formula of titanium and niobium carbides, it is recommended to add titanium in 5-fold and niobium in 8–11-fold amount to bind carbon. The special TiC and NbC carbides are not completely insoluble. Their solubility depends on the degree of stabilization, but their dissolution temperature is significantly higher than that of chromium carbides. Compared to low-carbon steels, stabilized steels are prone to IGC in approximately the same temperature range, but in stabilized steels, the tendency to IGC disappears at long-term holding times. The latter is explained by the fact that in stabilized steels, depending on the degree of stabilization, a certain amount of $M_{23}C_6$ is formed initially, rather than a special TiC or NbC carbide due to the slow diffusion of titanium and niobium. As the holding time grows, TiC or NbC carbides are formed — chromium carbide dissolves and chromium depletion disappears.

Since the precipitation of carbides from the solid solution occurs faster at the grain boundaries (Figure 1), the material near the grain boundaries is depleted by the alloying element, creating a potential difference that promotes better dissolution of the alloy boundary zones. IGC is observed in Cr- and Cr–Ni steels and leads to a sharp decrease in alloy strength and ductility, which can cause a premature structural failure. IGC can be caused by slow cooling of the alloy through the dangerous temperature region and even long-term welding works. This does not occur during rapid cooling.

Thus, IGC of steels and alloys occurs when a potential difference between the grain boundaries and the grain body arises in contact with the corrosive environment, the electrolyte. In general, three main mechanisms of intergranular corrosion can be distinguished in corrosion-resistant Cr- and Cr–Ni steels:

- depletion of grain boundary areas with elements that determine the material's stability in this environment;
- low chemical stability of phases precipitated at the boundaries;
- segregation of surface-active elements at the grain boundaries that reduce the stability of the base in this environment.

The mentioned IGC mechanisms can operate simultaneously in different steels, but one of them has a decisive influence on the corrosion rate. Usually, a phase precipitation from the solid solution occurs.

INTERGRANULAR STRESS CORROSION CRACKING (ISCC)

The problem of corrosion cracking of welds of austenitic steels in boiling water reactors (BWR) and light water reactors (LWR) first arose in the 70s of the twentieth century [6]. Western countries and Japan faced the problem of cracking of welded joints of pipelines made of austenitic stainless steels at NPPs with LWR reactors in the early 70s of the twentieth century. In the United States, cracks were first detected at the Unit 2 of the Dresden NPP in September 1974. Later, the problem of corrosion cracking at US NPPs became a large-scale one. On average, 25 % of welded joints had cracks, with some units having a defect rate of 50 %.

In this regard, a special programme of technological, calculation and experimental works was developed [6] to solve the following issues:

- need in repair of detected cracks;
- flaw detection of all welds;
- assessment of the fatigue life of defective or repaired sections;

long-term solutions that include replacement of pipeline systems.

Large capital investments were aimed at searching for improvement measures. The following were suggested as the most affordable and reasonable:

- induction heating to relieve residual stresses;
- deposition of external welding coating;
- mechanical crimping of the outer pipe surface near the defective WJ.

As a long-term goal and as the main focus of combating the ISCC phenomenon, KWU Siemens began developing new types of steels that are not prone to sensitization and corrosion [7].

In Japan, the ISCC study was carried out as part of the national programme to ensure the reliability of pipeline systems, the main goal of which was:

- demonstration of the integrity of pipeline system during operation, taking into account both fatigue and, especially, ISCC with sufficient safety factors;
- verification of the concept of 'leak before failure' in pipeline systems;
- demonstration of effective protective devices in case of guillotine failure.

Thus, based on the inspection, the following set of measures was developed to solve the problem of corrosion cracking of austenitic steels in boiling reactors:

- long-term measures: replacement of steels with other steels not prone to corrosion cracking;
- short-term measures: deposition of external welded coating, repair of defective areas, removal of residual stresses;
- temporary measures: justification of the admissibility of the defective weld operation.

MATERIALS SCIENCE ASPECTS OF THE CONDITION OF Du300 PIPELINES OF ChNPP UNIT No. 3

Unit No. 3 of the Chernobyl Nuclear Power Plant (ChNPP) belongs to the second generation of 1000 MW reactors (RBMK-1000) and represents a heterogeneous channel-type thermal neutron reactor with a graphite moderator and boiling light water coolant. The RBMK-1000 has a thermal design typical of single-circuit boiling water reactors, consisting of channel pipes and pipelines of various diameters, which together form a repeated forced circulation circuit (RFCC), as well as a steam pipeline supplying steam to the turbines. Most of the pipelines of the Du300 RFCC (downflow pipelines (DP), pressure pipelines (PP), automatic reactor coolant system (ARCS), etc.) have an outer diameter of 325 mm, rated wall thickness of 16 mm and are made of austenitic steel stabilized with 08Kh18N10T titanium, which is an analogue of AISI 321 stainless austenitic steel.

During the shutdown of ChNPP Unit 3 for routine repair in 1997, a 100 % radiographic inspection of welds of the DP, PP and ARCS pipelines (Table 2) was performed. By then, the equipment of ChNPP unit No. 3 had reached the end of 99230.33 operating hours. In accordance with the Instruction [8] and on the basis of the "Work Programme for Cutting Out Sections of Unit 3 Pipelines to Investigate the Condition of Base Metal and Welded Joints after 100 Thous H of Operation", the pipeline sections were cut out. The cut out pipeline sections were in operation since December 1981.

Table 2. Results of radiographic inspection of welds of ChNPP Unit 3 safety system pipelines obtained in 1997

Type of pipelines	No. of premises	Number of welds tested	Number of defects detected	
			Cracks	Welded defects
Downflow pipelines	804/1 БС 21	120	9	4
	BS 22	96	9	6
	804/2 BS 11	96	21	10
	BS 12	120	17	4
	403/1 BS 21	84	7	–
	BS 22	84	6	3
	403/2 BS 11	84	9	6
	BS 12	84	11	6
	Total	768	89	39
Pressure pipelines	404/1	88	23	–
	404/2	88	17	3
	403/1	160	23	4
	403/2	160	17	3
	Total	496	80	10
Pipelines of the reactor emergency cooling system	404/1	15	4	2
	404/2	12	6	1
	405	51	14	6
	216	14	5	3
	02	95	1	2
	Total	187	30	14
Total		1451	199	63

The Programme included determination of mechanical properties (σ_t, σ_y, δ, ψ) and impact toughness at room temperature (20 °C) and 350 °C; hardness (*HB*) of the pipe cross-section; determination of the chemical composition of the base metal and welded joints; microstructure examination; determination of the cyclic crack resistance characteristics of the base metal and welded joint. During the radiation inspection of 1451 welded joints of DP, PP and ARCS of the Du300 pipelines, 199 defects in the form of cracks and 63 welding defects were detected. All detected defects were repaired in 1997. Since there was no confidence that all weld defects were detected by radiographic inspection, the ChNPP management decided to perform 100 % ultrasonic testing (UT) of the welds available for UT. UT results obtained during 1997–1998 are shown in Table 3.

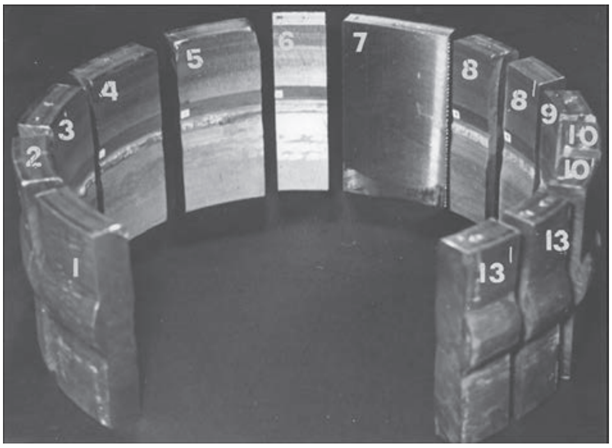

Figure 2. General appearance of a ring with a weld, cut into templates

Table 3. Results of ultrasonic testing of welds of pipelines of the safety system of ChNPP Unit 3 obtained in 1997–1998

Type of pipelines	No. of premises	Number of welds tested	Number of defects detected
Downflow pipelines	804/1 BS 21	107	9
	BS 22	81	7
	804/2 BS 11	65	6
	BS 12	99	19
	403/1 BS 21	77	12
	BS 22	75	11
	403/2 BS 11	69	9
	BS 12	67	9
	Total	640	82
Pressure pipelines	404/1	65	18
	404/2	68	17
	403/1	111	26
	403/2	118	32
	Total	368	93
Pipelines of the emergency reactor cooling system	404/1	9	–
	404/2	5	3
	405	31	2
	216	6	2
	02	92	1
	Total	143	8
Total		1145	183

Due to the fact that it was not possible to repair all the newly detected defects at ChNPP, it was decided to assess the ability of further operation of the ChNPP safety system pipelines with detected defects for another year (until the next routine repair).

In the process of testing damaged welded joints of pipelines, the following was studied:

- metal quality of welded pipes;
- areas of predominant cracks initiation and nature of their propagation;
- mechanism of open cracks propagation (fractography).

The object of studies was specimens cut out from rings (Figure 2) from ChNPP Unit 3 pipelines in the areas of damaged welded joints, including: 53 units of downflow pipelines, 32 units of pressure pipelines, and 4 units of ARCS.

Figure 2 shows a ring cut into templates containing a weld (in this case, weld No. 8 of the pressure pipeline). The templates are arranged in the same order as in the uncut ring, and the numbers indicated on the templates allow localizing subsequent investigations by referring to the corresponding template number.

The content of alloying elements in the studied specimens was determined using a Camascan scanning electron microscope with an X-ray spectrometer System 860 CP2-50 from Link System. To obtain

Table 4. Chemical composition (wt.%) of pipe metal made of 08Kh18N10T steel

Welded joint area	C	Mn	Si	Cr	Ni	S	P	Ti	Cu
Base metal on the left	0.08	1.41	0.55	19	10.17	–	0.035	0.4	0.07
Base metal on the right	0.08	0.99	0.23	19.28	10.21	0.018	–	0.428	0.3
Requirements in accordance with TU 14-3-197–73 for delivery in accordance with GOST 5632–72	≤ 0.08	≤ 1.5	≤ 0.8	17÷19	10÷11	≤ 0.02	≤ 0.035	5C÷0.06	≤ 0.3

Table 5. Mechanical properties of pipe specimens from the investigated 08Kh18N10T steel

Pipe specimens	T, °C	$\sigma_{0.2}$, MPa	σ_t, MPa	δ, %	ψ, %	KCV, kgs·m/cm^2
Diameter 325×16	+20	434 473 361	641 656 665	49.1 41.8 42.5	58.8 64.8 66.3	19.0 22.9 19.1

reliable results, measurements were made at several points. An example of the results is shown in Table 4.

THE MECHANICAL PROPERTIES

Were determined on plane or fivefold cylindrical specimens (type IV of GOST 1497–84) with a diameter of 4 mm in the temperature range of –196–+350 °C. Standardized tests for determining mechanical properties in the temperature range of 77–293 °C were carried out in a specialized Ala-Too unit and an Instron-1251 universal inspection machine, which were equipped with special cryo- and thermal chambers to create and maintain the appropriate test temperatures. A scheme of cutting specimens and their main dimensions are shown in Figure 3. The impact toughness was determined by the results of tests of Charpy specimens with a V-notch on a certified MK-30A pendulum tester in accordance with GOST 9454–78. In addition to impact tests of Charpy specimens, the ductile-brittle transition temperature (DBTT) was determined by the

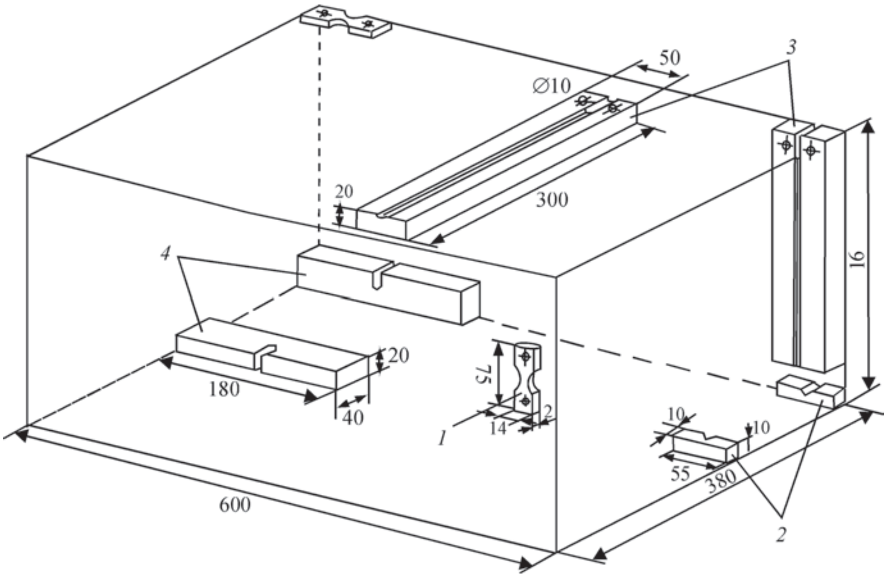

Figure 3. Scheme of cutting specimens and their basic dimensions

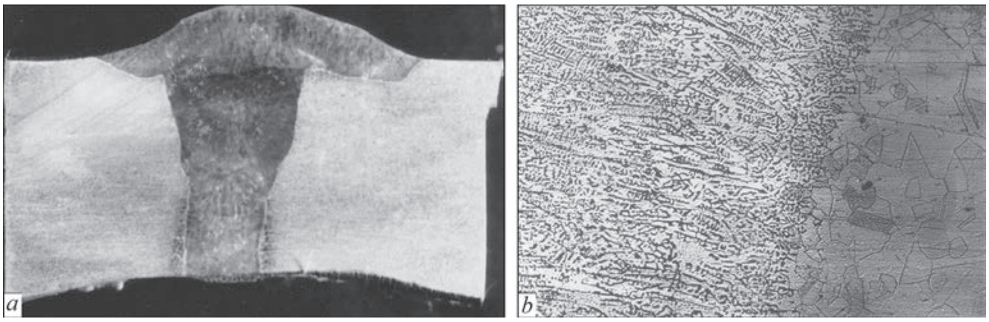

Figure 4. Structure of the pipeline material (325×16, 08Kh18N10T steel) at Unit 3 of the ChNPP after 100 thou h of operation: *a* — macrostructure, ×3; *b* — microstructure, ×100

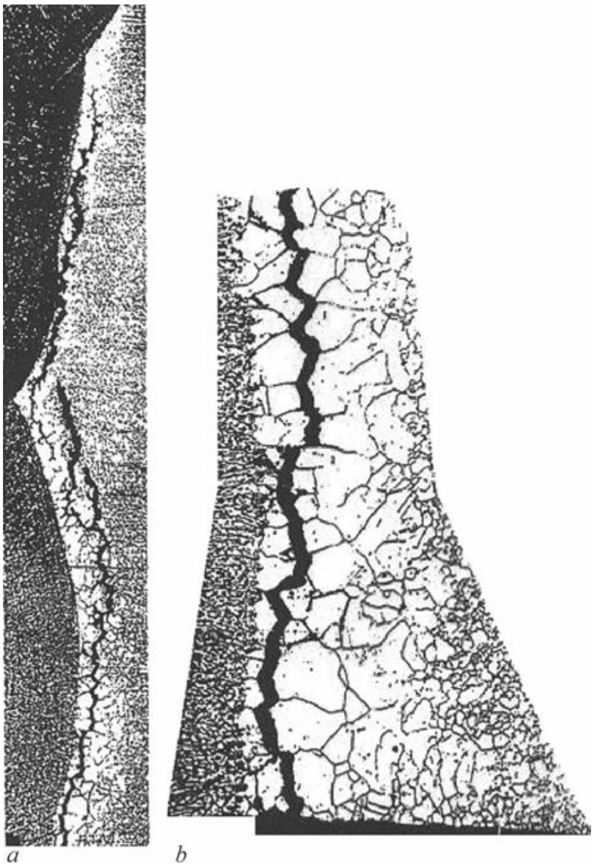

Figure 5. Appearance of a crack in the near-weld zone of welded joint: *a* — ×30; *b* — ×80

temperature dependence of the reduction in area and by X-ray analysis.

Some test results for pipe specimens made of 08Kh18N10T steel are shown in Table 5.

METALLOGRAPHIC EXAMINATIONS

Macrosections were made on the cutting surfaces (see Figure 2), followed by etching in 1 part HNO_3 +2 parts HCl reagent, which allowed revealing the contours and structure of the weld (Figure 4), as well as cracks, if any were present (Figure 5).

It should be noted that the susceptibility of steels to intergranular corrosion, which was determined by the standard procedure [9], was not detected even in defective welded joints. However, thorough metallographic examinations on templates cut out from the rings of downflow and pressure pipelines of the reactor's emergency cooling system revealed a narrow (up to 1 mm) zone of metal sensitization located along the fusion line (the zone of coarser austenitic grain). In this zone, the formation of a network of $Cr_{23}C_6$ carbides along the boundaries of austenitic grains was observed. To confirm this fact, micro-X-ray spectral analysis revealed an increased (up to 38 %) chromium content in a narrow zone at the boundaries of austenitic grains, while the chromium content in the grain body was 11–13 %.

Metallographic examinations made it possible to reveal cracks of circumferential orientation on the inner surface of the pipe (both in the weld and in the near-weld zone). The cracks observed in the near-weld zone were in the form of cracks with branches (Figure 5).

Branching cracks usually propagate deep into the base metal of the pipe intergranularly, along a narrow zone of the fusion line of austenitic grains that had grown during welding.

Crack initiation on the inner surface of the pipe had a multi-embryonic nature, and the propagation of main circumferential cracks occurred by merging of multilevel embryonic cracks. Cases of cracks location were observed on both sides of the weld.

FRACTOGRAPHIC STUDIES

Were carried out using a Camscan scanning electron microscope. These studies confirmed the intergranular (at crack growth in the HAZ) and intragranular (at crack growth along the weld metal) nature of crack propagation with numerous traces of corrosion impact on the grain boundary facets (Figure 6). Secondary cracks extending deep into the metal were observed on the fracture surface. Analysis of corrosion products on the fracture surface showed the presence of chlorine in the amount of 0.15 wt.%.

Fractographic and metallographic examinations of the crack surface cleaned of corrosion deposits showed that the main mechanism was intergranular fracture with crack branching typical of corrosion. On

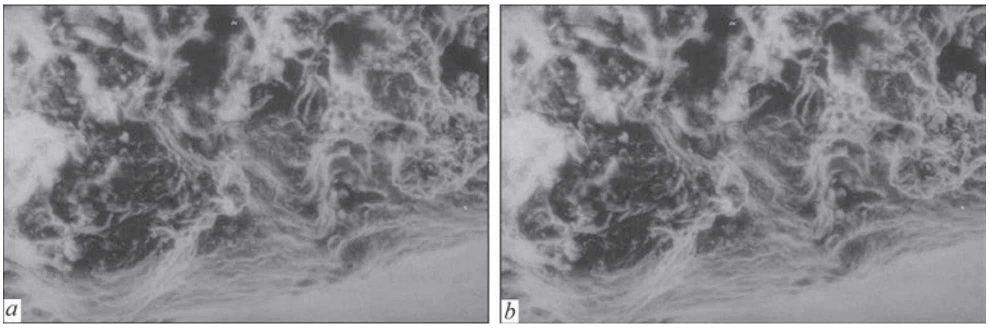

Figure 6. Microfractograms of a corrosion crack surface: *a* — before cleaning; *b* — after cleaning (average fatigue groove pitch $\Delta \approx 1.0$ μm)

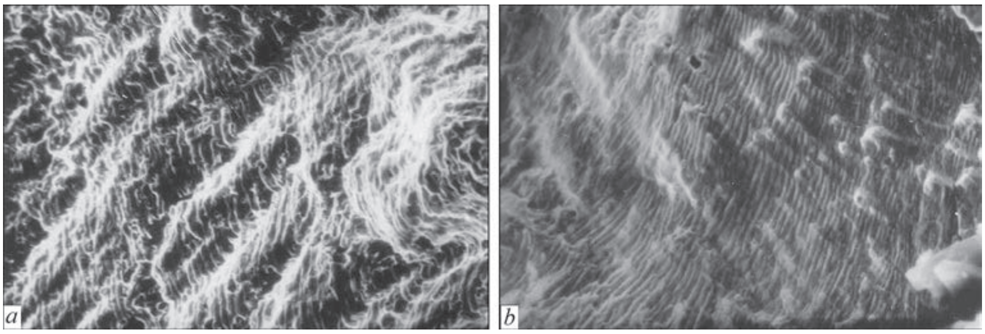

Figure 7. Fracture surface of the 08Kh18N10T steel specimen tested for cyclic crack resistance: *a* — at 20 °C, average fatigue groove pitch $\Delta \approx 1.5$ μm; *b* — at 50 °C, average fatigue groove pitch $\Delta \approx 2.0$ μm

the surface of the fracture, free of corrosion products, signs of fatigue fracture in the form of grooves were found, which can be detected even directly near the source of crack initiation (Figure 6, *b*). Distinct fatigue grooves are observed, which are an imprint of the crack front on each loading cycle, with a pitch of 0.4 μm. As a crack progressed, the pitch of the grooves increased to 1.0 μm.

Fractographic studies of the fracture surfaces of the cyclically loaded specimens revealed fatigue grooves that were clearly observed with a constant pitch corresponding to each degree of cyclic loading (Figure 7). This constant nature of the groove pitch was predetermined by the test conditions — the constant load amplitude at each loading stage. The measured groove pitch was related to the middle section of the fatigue fracture kinetic diagram, and in the entire load range, where fatigue grooves were observed, their pitch corresponded to the average crack rate measured directly on the specimen during the experiment.

Such a correspondence between the microscopic crack rate measured by the groove pitch and the macroscopic crack rate was observed at crack rates exceeding 10^{-7} m/cycle, and the measured groove pitch was in the range of 0.3–2.0 μm. This is in good agreement with many studies (e.g. [10]), where it was shown that the groove pitch correlated well with the macroscopic crack rate at crack rates higher than 10^{-7} m/cycle.

The less regular fatigue grooves observed on the surface of the intergranular corrosion cracks in the welds of the pipes showed a measured groove pitch of 0.4 to 1.0 μm (see Figure 7, *b*), which falls within the above-mentioned groove pitch interval measured on the specimens. This correspondence can be seen as evidence that the cyclic stress component in the pipe affects the growth of a corrosion crack, i.e., the superposition of stress corrosion cracking and fatigue crack growth processes. In other words, we observe the propagation of cracks by the corrosion fatigue mechanism.

FEATURES OF INTERGRANULAR CORROSION CRACKS PROPAGATION

According to the studies carried out on damaged circumferential welds cut out from the pipelines of Unit No. 3 (pipelines of the 1st circuit with an outer diameter of 325 mm and a wall thickness of 16 mm), intergranular corrosion cracks initiate near the root weld on the inner wall of the pipe and propagate, as a rule, in the HAZ along the weld fusion line. In some places, crack initiation are local stress concentrators caused either by metal shrinkage during root weld cooling or by rough machining marks on the pipe's inner surface during welding. A large number of such concentrators on the inner part of the weld and in the near-weld zone leads to the initiation of several cracks. These cracks, which have several nuclei located in different parallel sections of the pipe, often merge into a single crack during propagation. As the moments of initiation of these cracks do not coincide in time, some cracks are ahead of other, which, when merging into a common main crack, leads to its twisting front. The appearance of the surface of one of such cracks is shown in Figure 8, where seven adjacent final fractured templates cut out from a damaged weld are shown.

Each opposite half of the template contains the response surface of the same corrosion crack (of dark colour, facing outward in the image) and the surface of the final crack (of light colour, facing inward), resulting from the mechanical fracture of the templates during their bending.

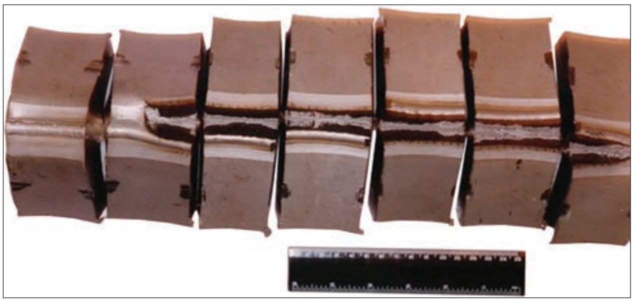

Figure 8. Appearance of a surface crack on the fractured templates

The surfaces of corrosion cracks are covered with a thick layer of corrosion deposits that are dark brown in colour and have significant radioactivity. When studying the growth characteristics of corrosion cracks, it was observed that the choice of the growth trajectory by a crack is largely determined by the place of its initiation, which, in turn, depends on the efficiency (i.e., the sharpness) of the local stress concentrator. Therefore, at the damaged welded joints cut out from pipes, both cracks propagating along the HAZ near the fusion line and (less frequently) cracks growing along the weld metal were observed. To take these features into account, it is necessary, firstly, to determine the strength of the weld metal, and secondly, to determine the limit fracture load of the weld section that remained unaffected by a crack.

CONCLUSIONS

1. Metallographic and fractographic studies of the welded joints of the pipelines of Power Unit No. 3 of the Chernobyl NPP revealed intergranular (with crack growth in the HAZ) and intragranular (with crack growth along the weld metal) fracture. Significant corrosion damage with typical crack branching was observed in both cases.

2. Additional fractographic studies of the surfaces of corrosion fracture of welds confirmed the presence of signs of cyclic loads (fatigue grooves) on a significant fracture area.

3. As a result of comprehensive metallographic, fractographic and micro-X-ray spectral studies, a set of measures was developed to solve the problem of stress corrosion cracking in austenitic steels.

4. In the event of a probable IGC propagation, monitoring the formation and propagation of cracks becomes particularly important for the reliable operation of power equipment. It is especially important to be able to measure the geometric characteristics of cracks, which significantly expands the capabilities of temporary and short-term measures to maintain operational reliability. Therefore, the development and optimization of non-destructive testing methods for welded joints prone to IGC is an urgent task.

REFERENCES

1. *IAEA. Report of a regional workshop on environmentally assisted cracking of NPP austenitic piping. Slavutych, Ukraine, 22–26 June 1998*. Introduction, 7–38.
2. Krasovsky, A.Ya., Makovetskaya, I.A., Torop, V.M., Chugunov, V.A. (2000) Examination of causes of stress corrosion cracking in 1st pipeline circuit of NPP. In: *Proc. of Conf. on Assessment and Substantiation of Extension of the Service Life of Structural Elements, Kyiv, 6–9 June, 2000*, IPS, Vol. 1, 27–34 [in Russian].
3. Yasniy, P.V., Hlado, V.B., Hutsaylyuk, V.B., Vuherer, T. (2005) Microcrack initiation and growth in heat-resistant 15Kh2MFA steel under cyclic deformation. *Fatigue & Fracture of Engineering Materials & Structures*, 28(**4**), 391–397.
4. Lai, J.K., Shek, C.H., Lo, K.H. (2015) *Stainless steels: An introduction and their recent development*. Hong Kong, Bentham Books.
5. Lawrynowicz, Z. (2018) Diagnostics of the effect of prior cold deformation and aging time on intergranular corrosion resistance in case of austenitic stainless steel. In*: Proc. of .* 17th *Inter. Conf. on Diagnostics of Machines and Vehicles.* MATEC Web of Conf., **182**, 2018. 01011.
6. (1975) *US NRC pipe crack study group. Investigation and evaluation of cracking in austenitic strainless steel piping of BVR plants*. NUREG–75/061.
7. (1986) Pressure vessel and piping codes. Evaluation of flaws in austenitic steel piping. Transact. of ASME. *J. of Pressure Vessels Technology*, **3**, 357.
8. (1988) *Instruction on investigation of state of metal of NPP pipelines using cut-out samples after 100 thou h of operation (AI*-35-17–86). Moscow, VNIIAES. Introd. 30.04.88 [in Russian].
9. (1990) GOST 6032–89: *Corrosion-resistant steels and alloys*. Moscow, Izd-vo Standartov [in Russian].
10. (2002) *IAEA-EBP-IGSCC Mitigation of intergranular stress corrosion cracking in RBMK reactors.* Final Report of the Programme’s Steering Committee. IAEA-EBP-IGSCC. A publication of the extrabudgetary programme on mitigation of intergranular stress corrosion cracking in RBMK reactor.

ORCID

V.M. Torop: 0000-0002-8807-9811,
V.B. Hutsaylyuk: 0000-0003-4812-5737,
M.D. Rabkina: 0000-0003-3498-0716,
E.O. Davydov: 0000-0003-3470-2329

CONFLICT OF INTEREST

The Authors declare no conflict of interest

CORRESPONDING AUTHOR

V.M. Torop
E.O. Paton Electric Welding Institute of the NASU
11 Kazymyr Malevych Str., 03150, Kyiv, Ukraine.
E-mail: v.torop@gmail.com

SUGGESTED CITATION

V.M. Torop, V.B. Hutsaylyuk, M.D. Rabkina, E.O. Davydov (2025) Study of intergranular corrosion cracking in welded joints of Chornobyl NPP pipelines. Materials science aspect. *The Paton Welding J*., **3**, 41–48.
DOI: https://doi.org/10.37434/tpwj2025.03.06

JOURNAL HOME PAGE

https://patonpublishinghouse.com/eng/journals/tpwj

Received: 17.10.2024
Received in revised form: 27.11.2024
Accepted: 17.04.2025

TO THE 155th ANNIVERSARY OF THE BIRTH OF EVGENY PATON

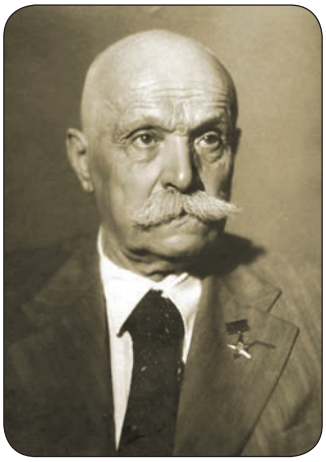

Evgeny Paton was born on March 4, 1870, into the family of a Russian Empire consul in Nice, France. He received his higher education in 1894 at the Royal Saxon Technical University in Dresden, Germany. He was offered a teaching position at the Department of Structural and Bridge Statics, and he had already begun working at the design office for the construction of the new Dresden railway station, but he declined the offer.

After graduating in 1896 from the St.-Petersburg Institute of Railway Engineers, Paton began teaching at the Institute while simultaneously working in the technical department of the state railways, where the designed bridges and floors. Since the spring of 1889, he worked at the Moscow Engineering School of Railway Communications, and in 1901 he defended his dissertation and was appointed professor of the Department of Bridges.

In 1905, Paton began working at the Kyiv Polytechnic Institute, where he headed the Department of Bridges and was elected dean of the Civil Engineering Faculty. He improved educational programs, established laboratories, created an engineering museum, continued scientific work, and published manuals and textbooks. In 1914, Paton organized the Bridge Section of the Military-Industrial Committee of the Southwestern.

Front, where he designed and supervised the production of bridges, pivot-lift trestles, icebreakers, and other structures. For crossings over the Dnipro River, he developed the designs for seven large strategic demountable bridges.

For about 35 years of scientific, engineering, and teaching activity, Paton dedicated himself to bridge construction. He published over 160 scientific papers and created designs for 35 bridges, floors, and crossings. From 1920 onward, Paton, together with his students, actively participated in the restoration of destroyed bridges. Simultaneously, from 1921 to 1931, he served as head of the Kyiv Bridge Testing Station.

In 1929, Paton was elected an academician of the All-Ukrainian Academy of Sciences (now the National Academy of Sciences of Ukraine). Within the Academy, he organized the Electric Welding Laboratory and the Electric Welding Committee — public organizations that facilitated cooperation between scientists and engineering-technical workers interested in the development of welding production. Paton was elected chair of the Committee.

From 1929 to 1933, Paton and a small team conducted studies of the performance characteristics of welded structures and carried out comparative testing of a series of full-scale riveted and welded products. The results were presented in 1933 in the first domestic manual on the design of welded structures, which was later reprinted in foreign editions.

In 1932, Paton was the first in the world to develop and propose a comprehensive program for the development of welding, which was supported by the government. In 1934, the government of the Ukrainian SSR issued a decree on the establishment of the Electric Welding Institute (EWI). Evgeny Paton was appointed director. In line with the Institute's main areas and the comprehensive nature of its work, he organized several departments: scientific-research, design, welding equipment, welded structures, and an experimental-production

Arch bridge over the Alley of Magdeburg Rights in Kyiv today (built in 1910)

Demountable bridge of the Evgeny Paton system, 1914 base (workshops for manufacturing instruments and devices). EWI became a model scientific institution capable of creating innovative technologies — from conceptual and fundamental research to wide-scale industrial implementation.

At Paton's initiative, who paid great attention to personnel training, a department for training welding engineers was established in 1935 at the Kyiv Industrial Institute (National Technical University of Ukraine "Igor Sikorsky Kyiv Polytechnic Institute"), which later became the Welding Faculty and Department. He headed them until 1939.

The results of research on processes in the welding pool and other works laid the foundation for a new scientific direction — the metallurgy of welding processes. A remarkable achievement was the development of automatic submerged arc welding. By early 1939, under Paton's leadership, equipment, materials, and technology for high-speed automatic welding had been developed, which ensured high-quality welds when working with structural steels.

On December 20, 1940, the USSR leadership adopted a decree on the implementation of high-speed automatic submerged arc welding in industry. Paton was appointed a member of the Council on Mechanical Engineering under the Council of People's Commissars of the USSR and was entrusted with supervision over the implementation of this decree. Simultaneously, he was assigned to head the Welding Department at the Central Scientific Research Institute of Machine Building Technology (Moscow) while maintaining his position as director of EWI. Within six months, EWI staff managed to implement the innovative technology at 20 large enterprises, significantly increasing production efficiency. In 1940, Paton authored the monograph *"High-Speed Automatic Submerged Arc Welding"*.

In August 1941, EWI was evacuated to Nizhny Tagil. In 1942, under Paton's leadership, automatic welding of complex-alloyed armor steels was developed for the first time in the world. This accelerated the production of tank hulls tenfold. In the shortest possible period, under his direction, mass production of all types of tanks, aerial bombs, rocket shells, and many other types of weapons and ammunition was organized.

In 1943, Evgeny Paton became the first Ukrainian scientist to be awarded the title Hero of Socialist Labor.

In 1944, the EWI returned to Kyiv, and Evgeny Paton became involved in addressing the issues of restoring and developing the national economy. The conversion of the highly efficient "military" technology — automatic submerged arc welding — for civilian use became the institute's primary task. By the end of 1944, automatic submerged arc welding had been implemented at 12 major enterprises in Ukraine. In 1947, Evgeny Paton was entrusted with the scientific and organizational support of all welding operations in the USSR. During 1947–1948, 670 welding automatic machines were introduced at 111 plants across the country; EWI organized worker training, developed manuals, and created a special railcar equipped with training and demonstration equipment.

Evgeny Paton initiated fundamental research that became the theoretical foundation of the science of welding, improved the principles of designing new welding equipment, welding process control systems, and equipment for manufacturing metal structures, as well as addressing other engineering challenges.

One of Paton's ideas was to divide structures into units and weld them using specialized machines at separate positions along conveyor lines, which was a fundamentally new approach to the design and production of machines, tanks, pipe, and industrial structures. The Institute addressed tasks related to improving the manufacturability of welded products, reducing their weight, and decreasing the number of connecting parts.

Under his leadership, innovative industrial methods were developed for the production of pipes, welding of main pipelines, oversized tanks, blast furnace complexes, wagons, ships, atc. — primarily at the plants of the Dnipro and Donbas regions. From 1946 to 1948, a railway tank production line was launched at the Illich Iron and Steel Works in Mariupol.

With Evgeny Paton's active involvement, the following were developed for the first time in the world: a method of semi-automatic submerged arc welding with mechanized feeding of the electrode wire through a flexible hose to a manually operated holder with a nozzle and a flux hopper; a welding gun for ceiling structures; specialized installations for welding boiler equipment and industrial building steel structures.

For the first time in the world, it was proven that the shape of welded structures could be changed, and a fundamentally new method of constructing large sheet structures was developed — by rolling up fully welded sheets. Since 1948, this method has been used for building tanks.

Also for the first time in the world, EWI developed technologies for combined assembly and welding, relevant machine tools and conveyor lines, and rational welded designs of mining, power, and metallurgical equipment, as well as furnaces and bridges. Several welding machines, mechanisms, and devices — such as the roll-welding machine for mining carts, electroslag welding equipment, and a continuous system for automatic welding of large-diameter pipes — had no foreign equivalents.

For construction and installation works, technologies and equipment for automatic welding of vertical and overhead seams under flux were developed for the first time. The first all-welded blast furnace in Europe, with a volume of 1033 m^3, was erected in 1948 in Zaporizhzhia using this technology.

To increase welding speed, new technologies were developed for automatic submerged arc welding with an electrode tilted “forward along the weld axis”, split electrodes, atc. In 1946–1947, EWI created a welding technology with a speed of 160–200 m/h using two separately burning arcs, along with the necessary welding apparatus.

In 1949, the first domestic continuous pipe electric welding machine, welding equipment, and power sources were put into operation at the Khartsyzk Pipe Plant. For the first time, assembly and welding were performed in a single unit with a stationary welding head and a moving workpiece.

From 1949 to 1953, the processes and nature of current flow through the slag bath, electrode metal melting, and heat exchange between slag and the welded product were studied. The electroslag welding method, which allows single-pass welding of thick-walled metal structures, was invented for the first time in the world.

In 1949–1950, the regularities of electric and metallurgical processes during arc welding of steel in active gases were studied. It was established that the metal quality could be improved by introducing additional deoxidizers, and the technology of welding in carbon dioxide was created for the first time in the world. In 1952, studies were conducted on the interaction of chlorine and fluorine with components of the arc plasma and molten metal during welding of aluminum and its alloys. For the first time, chemical compositions of haloid fluxes and arc welding technology were developed.

By the mid-1950s, Ukraine had restored its mining-metallurgical and fuel-energy industries. A mechanized method for welding circumferential seams of main pipelines was developed and applied in constructing the Dashava–Kyiv–Bryansk–Moscow pipeline.

In 1952, research was conducted for the first time in the world, establishing the fundamental possibility of using welding heat sources to produce extra hight-purity metal in the electroslag process. The first electroslag remelted ingot was produced, and a special remelting unit was created.

Under Evgeny Paton’s leadership, comprehensive publications on various aspects of welding science and technology were issued. In 1948, he founded and became the chief editor of the Automatic Welding Journal.

Fundamental research laid the groundwork for the development of new scientific fields and breakthrough innovative technologies in numerous industries. Electroslag welding was invented for the first time globally, establishing the basis for a new branch of special electrometallurgy of high-quality metals.

From 1947 to 1952, the principles of weld metal alloying via flux-cored wire were established. Compositions of wires were developed, and arc surfacing techniques for wear-resistant surfaces of components operating under high temperatures and impact loads were introduced.

Between 1946 and 1951, under Paton’s guidance, a special low-carbon steel grade MSt3 was created for welded bridges. It was less sensitive to the thermal deformation cycle of welding. A new bridge design was developed, welding equipment was improved for both automatic and mechanized welding of structures, and technologies for plant-based and on-site welding were devised.

An outstanding example of the universal application of automatic submerged arc welding is the construction of the all-welded highway bridge across the Dnipro River in Kyiv, with a total length of over 1.5 kilometers. The bridge was completed in 1953 and recognized by the American Welding Society as an exceptional welded structure. The largest all-welded highway bridge in Europe was opened in Kyiv in November 1953. Evgeny Paton did not live to see its inaugu-

Welding of a bridge deck beam, Dnipropetrovsk, 1952 ration — he passed away on August 12, 1953, less than three months before the opening.

The American Welding Society in 1995 awarded the Evgeny Paton Bridge as a significant welded structure of the twentieth century.

AWS

American Welding Society
Historical Welded Structure
Award

МІСТ імені
ЄВГЕНА ПАТОНА
1953

Перший суцільнозварюваний довжиною в 1540 м. міст було споруджено в 1953 р. Його було виготовлено в майстернях використовуючи 30 відсотків механічного скріплення та застосовуючи вперше новий метод з'єднання при допомозі зварювання, який пізніше дістав назву «Електрозварка».

Здобув визнання Асоціацією Зварювання США
6 квітня 1995 р.

EVGENY PATON
BRIDGE
1953

First all-welded 1540 m long bridge erected in 1953. It was shop fabricated using 30% mechanized welding and erected making the first use of a new vertical butt welding process, *later to become known as "Electrogas" and "Electroslag" welding.*

Recognized by the American Welding Society
April 6, 1995.

American Welding Society commemorative plaque

In 2000, the International Institute of Welding established the international Evgeny Paton prize for professionals, who has made a significant contribution to science and technology through his lifetime dedication to applied research and development in the field of advanced technologies, materials and equipment for welding and allied processes.

Evgeny Paton Prize Medal

WINNERS OF EVGENY PATON PRIZE:

- 2000 Dr. Stephen Maddox (United Kingdom);
- 2002 Eur. Ing. Wayne Thomas (United Kingdom);
- 2003 Prof. William Lucas (United Kingdom);
- 2004 Dr. Nobutaka Yurioka (Japan);
- 2005 Prof. John Norrish (Australia);
- 2006 Dr. Alan Sanderson (United Kingdom);
- 2007 Dr. Pingsha Dong (USA);
- 2009 Prof. Shang Yang Lin (China);
- 2010 Dr. Carl D. Lundin (USA);
- 2011 Prof. Wolfgang Fricke (Germany);
- 2012 Dr. Michael Szczesny (USA);
- 2013 Dr. Adolf F. Hobbacher (Germany);
- 2017 Prof. Yoshinori Hirata (Japan);
- 2018 Univ.-Prof. Dr.-Ing. Uwe Reisgen (Germany);
- 2019 Prof. David Olson (USA);
- 2021 Prof. Michael Ghede (Germany);
- 2023 Dr. Murali Tumuluru (USA);
- 2024 Prof. Suck-Joo Na (Korea Repyblic).

Evgeny Paton established the globally renowned Paton scientific and engineering school, which became a symbol of the effective implementation of fundamental scientific developments and will continue to make significant contributions to the advancement of science and technology in Ukraine.

Dr. of Historical Sci. Oleksandr Kornienko

Evgeny Paton bridge today